

Titre: Synthesis and Characterization of Bismuth Telluride-Based
Title: Nanostructured Thermoelectric Composite Materials

Auteur: Mohsen Keshavarz Khorasgani
Author:

Date: 2014

Type: Mémoire ou thèse / Dissertation or Thesis

Référence: Keshavarz Khorasgani, M. (2014). Synthesis and Characterization of Bismuth
Citation: Telluride-Based Nanostructured Thermoelectric Composite Materials [Thèse de
doctorat, École Polytechnique de Montréal]. PolyPublie.
<https://publications.polymtl.ca/1372/>

 **Document en libre accès dans PolyPublie**
Open Access document in PolyPublie

URL de PolyPublie: <https://publications.polymtl.ca/1372/>
PolyPublie URL:

**Directeurs de
recherche:** Sylvain Turenne, & Rémo A. Masut
Advisors:

Programme: Génie métallurgique
Program:

UNIVERSITÉ DE MONTRÉAL

SYNTHESIS AND CHARACTERIZATION OF BISMUTH TELLURIDE-
BASED NANOSTRUCTURED THERMOELECTRIC COMPOSITE
MATERIALS

MOHSEN KESHAVARZ KHORASGANI
DÉPARTEMENT DE GÉNIE MÉCANIQUE
ÉCOLE POLYTECHNIQUE DE MONTRÉAL

THÈSE PRÉSENTÉE EN VUE DE L'OBTENTION
DU DIPLÔME DE PHILOSOPHIÆ DOCTOR
(GÉNIE MÉTALLURGIQUE)

MARS 2014

UNIVERSITÉ DE MONTRÉAL

ÉCOLE POLYTECHNIQUE DE MONTRÉAL

SYNTHESIS AND CHARACTERIZATION OF BISMUTH TELLURIDE-BASED
NANOSTRUCTURED THERMOELECTRIC COMPOSITE MATERIALS

présenté par : KESHAVARZ KHORASGANI Mohsen

en vue de l'obtention du diplôme de : Philosophiæ Doctor

a été dûment accepté par le jury d'examen constitué de :

M. TERRIAULT Daniel, Ph.D., président

M. TURENNE Sylvain, Ph.D., membre et directeur de recherche

M. MASUT Remo A., Ph.D., membre et codirecteur de recherche

M. YELON Arthur, Ph.D., membre

M. BROCHU Mathieu, Ph.D., membre

DEDICATION

I dedicate this work to

my supportive parents,

my lovely wife

&

my beautiful son.

“The true human ornaments are: knowledge, love, and freedom.”

Ferdowsi Tusi

ACKNOWLEDGMENTS

First, the financial support of the Natural Science and Engineering Research Council of Canada (NSERC), and the Fonds Québécois de la Recherche sur la Nature et les Technologies (FQRNT) is gratefully acknowledged.

I feel truly blessed to find the position as Ph.D. student in the thermoelectric research group of École Polytechnique de Montréal. It is genuinely a privilege to be working with and under the instruction of such group of prestigious scholars; Prof. Sylvain Turenne, Prof. Remo Masut, and Dr. Dimitri Vasilevskiy. Thanks and gratitude is given to my research director, Prof. Sylvain Turenne, for his open-ended support, insightful opinions, and extremely valuable advices in many occasions. Special thanks to my research co-director, Prof. Remo Masut, who has given very generously of his time to discuss various aspects of this project. In addition to his help in working on the project, writing the articles, and my dissertation, he has always been available to encourage, and lend perspective along the way. I would like to express my deep gratitude to my mentor, Dr. Dimitri Vasilevskiy, for his strong encouragement, support, guidance, and advices through my Ph.D. study. I am extremely indebted to him for his fatherly generosity, detailed instructions, high-standard education, also for sharing lots of time doing experiments, doing discussions, and helping me to develop my understanding specially in physics fundamentals. I just can say that without him, I would not have accomplished my Ph.D.

I would be remiss not to thank my friends, my colleagues and other members of thermoelectric research group of École Polytechnique de Montréal who helped and supported me a lot during my study. I would also like to recognize and thank the following individuals for their assistance in various aspects of this work: Mr. Siamak Kashi, Dr. Javier Arreguin Zavala, Mr. Melik Bouhadra, Mr. Frédéric Tremblay Verville, Mr. Jean-Philippe Masse, and Mrs. Carole Massicotte, besides all the staff of École Polytechnique de Montréal specially the secretaries and technicians of departments of mechanical engineering and engineering physics.

Most of all, I would like to gratefully thank my wife, and my parents in Iran for their love, support, and inspiration. My wife, Hoory, has been always a good listener for my toughest moments of life. She has always been there to help unconditionally, support unlimitedly, and inspire me amorously, and I owe her a special debt of gratitude.

Mohsen Keshavarz

ABSTRACT

Thermoelectric (TE) materials and devices are attractive in solid-state energy conversion applications such as waste heat recovery, air-conditioning, and refrigeration. Since the 1950's lots of unremitting efforts have been made to enhance the efficiency of energy conversion in TE materials (i. e. improving the figure of merit (ZT)), however, most of commercial bulk TE materials still suffer from low efficiency with ZT s around unity. To enhance the performance of bismuth telluride based TE alloys, we have developed composite TE materials, based on the idea that introducing more engineered interfaces in the bulk TE materials may lead to thermal conductivity reduction due to increased phonon scattering by these interfaces. In this approach it is expected that the electronic transport properties of the material are not effectively affected. Consequently, ZT enhancement can be achieved.

In this dissertation we will discuss synthesis and characterization of two types of bismuth telluride based bulk composite TE materials. The first type is engineered to contain the presence of coherent interfaces between phases in the material resulting from different mixtures of totally miscible compounds with similar composition. The second type includes the nanocomposites with embedded foreign nano-particles in which the matrix and the particles are delimited by incoherent interfaces. The synthesis procedure, micro- and nano-structures as well as thermoelectric properties of these composites will be presented.

In our study on the composites with coherent interfaces, we produced a series of different composites of p -type bismuth antimony telluride alloys and studied their microstructure and thermoelectric properties. Each composite consists of two phases that were obtained in powder form by mechanical alloying. Mixed powders in various proportions of the two different phases were consolidated by hot extrusion to obtain each bulk composite. The minimum grain size of bulk composites as revealed by scanning electron microscopy shows a 50% reduction compared to the conventional $(\text{Bi}_{0.2}\text{Sb}_{0.8})_2\text{Te}_3$. XRD analysis indicates a systematic decrease of crystallite size in the composite materials. Scattering mechanisms of charge carriers were evaluated by Hall effect measurements. There is no evidence of carriers scattering linked to the composite nature in these materials. The composites show no significant degradation of the power factor and high peak ZT values ranging from 0.86 to 1.04. It was found, contrary to expectations that the thermal conductivity of the composites slightly increases compared to the conventional alloy. This

behavior has been attributed to two factors: (1) the grains of the composites are not sufficiently small to increase phonon scattering, and (2) the lattice thermal conductivity of single phase $(\text{Bi}_{0.2}\text{Sb}_{0.8})_2\text{Te}_3$ alloy has the smaller value in comparison with the lattice thermal conductivity of each of the components of the composites.

Importantly, we have already demonstrated the feasibility of this approach to conserve the electronic transport properties while more interfaces are introduced in the material. We believe that continued investigation following this approach can guide us to achieve an enhanced figure of merit.

We have also studied bulk nanocomposites of *p*-type $(\text{Bi}_{0.2}\text{Sb}_{0.8})_2\text{Te}_3$ and *n*-type $(\text{Bi}_{0.95}\text{Sb}_{0.05})_2(\text{Te}_{0.95}\text{Se}_{0.05})_3$ with embedded MoS_2 nano-inclusions, which were obtained by mechanical alloying and hot extrusion. This series of TE nanocomposites contain incoherent interfaces between nano-particles and the matrix. We have found that addition of molybdenum disulfide (MoS_2) nano-particles to the matrix improves the extrusion process and limits the grain growth in bismuth telluride based alloys. Transmission electron microscopy revealed that grain boundaries of the matrix are decorated by nano-inclusions, leading to a significant reduction of average grain size and crystallite size compared to those of the conventional single phase alloy. Scanning electron microscope images show that the average grain size of *p*-type $(\text{Bi}_{0.2}\text{Sb}_{0.8})_2\text{Te}_3$ composites containing 0.2, 0.4 and 0.8 wt% MoS_2 nano-particles, under otherwise identical extrusion conditions, is reduced by a factor around four. Scherer's formula applied to x-ray diffraction data indicates that after the hot extrusion process, the average crystallite size in composites increases only by 10% (~ 18 nm) compared to about 400% growth (~ 80 nm) observed in the single phase bismuth telluride based alloy. Smaller crystallites, as expected, lead to a reduction of the thermal conductivity in these nanocomposites (~ 1.4 W/m·K at 450 K for 0.4 wt.% MoS_2) when compared to the conventional alloy (~ 1.8 W/m·K). The structural changes in the nanocomposites characterized by mechanical spectroscopy in the temperature range 293-540 K show an increase of the internal friction accompanied by a systematic reduction of its activation energy with increase in MoS_2 content, which is an indication of higher density of crystal defects in the nanocomposites that largely contribute to the internal friction background. Investigation of TE properties shows a reduction of the room temperature figure of merit (*ZT* values) from 0.9 to 0.7 due to a lower power factor. However, once above 370 K, the figure of merit of alloys containing MoS_2 nano-particles surpasses that of single phase $(\text{Bi}_{0.2}\text{Sb}_{0.8})_2\text{Te}_3$, due

to a more pronounced reduction in the thermal conductivity at temperatures above the cross point of the ZT values.

Remarkably, we have demonstrated that adding nano-particles of MoS_2 to bismuth telluride based alloys is an approach to significantly reduce the grain size of the matrix resulting in an important thermal conductivity decrease. The enhanced ZT values above 370 K in nanocomposites show the preeminent achievement of this approach, although further study is required to obtain optimum transport properties, and boost up the ZT more effectively.

RÉSUMÉ

Les matériaux et dispositifs thermoélectriques (TE) sont intéressants pour les applications en conversion d'énergie tels la récupération de chaleur, la climatisation et la réfrigération. Depuis les années 50, plusieurs efforts ont été déployés pour améliorer l'efficacité des matériaux TE pour la conversion d'énergie (amélioration de la figure de mérite ZT). Malgré ces efforts, la plupart des matériaux TE atteignent au mieux une valeur de ZT de l'ordre de 1. Pour améliorer la performance des alliages TE à base de tellure de bismuth, nous avons développé des matériaux TE composites à partir de l'hypothèse que par addition d'interfaces dans la structure du matériau TE, il soit possible de réduire la conductibilité thermique par la diffusion des phonons sur ces interfaces. En suivant cette approche, on suppose que les propriétés de transport électronique ne seront pas grandement affectées, menant ainsi à une augmentation de ZT .

Dans cette thèse, nous discuterons des procédés d'élaboration et de la caractérisation de deux types de composites TE basés sur le tellure de bismuth. Le premier type de composite est obtenu en créant des interfaces cohérentes entre différentes phases miscibles de compositions chimiques similaires. Le second type de nanocomposite est fabriqué par l'addition de nanoparticules d'une espèce différente menant à la présence d'interfaces incohérentes entre les particules et la matrice. Les étapes des procédés, la caractérisation micro- et nanostructurale ainsi que les propriétés thermoélectriques seront présentées dans cette thèse.

Dans l'étude des composites avec interfaces cohérentes, nous avons produit différents mélanges d'alliages de type p de tellure de bismuth et d'antimoine pour évaluer leurs propriétés TE et leur microstructure. Chaque composite est constitué de deux phases qui sont élaborées à partir de poudres par mécanosynthèse. Le composite est obtenu en extrudant à chaud différentes proportions des deux phases de compositions différentes. La taille de grains minimale pour les composites, évaluée par microscopie électronique à balayage, montre une réduction de 50% par rapport à la taille de grains de l'alliage $(\text{Bi}_{0.2}\text{Sb}_{0.8})_2\text{Te}_3$ élaboré par la méthode conventionnelle. L'analyse par diffraction des rayons x (XRD) indique une décroissance systématique de la taille des cristallites dans le composite. Les mécanismes de diffusion des porteurs de charges ont été caractérisés à partir de mesures de l'effet Hall. Nous n'avons pas observé d'évidence de diffusion des porteurs dans ces composites. Aucune décroissance significative du facteur de puissance n'a été observée et de hautes valeurs de la figure de mérite ZT ont été obtenues, entre 0.86 et 1.04.

Contrairement à ce qui avait été anticipé, nous avons observé une légère augmentation de la conductibilité thermique des composites comparée à celle caractérisant l'alliage conventionnel. Ce comportement peut être expliqué par deux facteurs : (1) les grains du composites ne sont pas suffisamment petits pour augmenter la diffusion des phonons et (2) la composante du réseau de la conductibilité thermique de la phase $(\text{Bi}_{0.2}\text{Sb}_{0.8})_2\text{Te}_3$ est plus faible que celle de chacun des constituants des composites.

Il est important de mentionner que cette approche de fabrication de composites permet de conserver les propriétés de transport électronique tout en augmentant la présence d'interfaces. Nous croyons qu'il sera aussi possible en poursuivant nos travaux d'améliorer la figure de mérite.

Pour l'étude des nanocomposites du second type, nous avons élaborés les composites par addition de nano-inclusions de disulfure de molybdène (MoS_2) dans des matrices de type *p* $(\text{Bi}_{0.2}\text{Sb}_{0.8})_2\text{Te}_3$ et de type *n* $(\text{Bi}_{0.95}\text{Sb}_{0.05})_2(\text{Te}_{0.95}\text{Se}_{0.05})_3$ par mécanosynthèse et extrusion à chaud. Ces nanocomposites contiennent des interfaces incohérentes entre les nano-particules et la matrice. Nous avons observé que l'addition de nano-particules de MoS_2 facilite le processus d'extrusion et limite la croissance des grains des alliages de tellure de bismuth. La microscopie électronique à transmission révèle que les nano-particules se situent au niveau des joints de grains, limitant ainsi significativement la croissance des grains et des cristallites, comparé au cas de l'alliage conventionnel monophasé. La microscopie électronique à balayage montre que la taille de grains moyenne pour les composites basés sur l'alliage de type *p* $(\text{Bi}_{0.2}\text{Sb}_{0.8})_2\text{Te}_3$ contenant 0.2, 0.4 et 0.8% poids de nano-particules de MoS_2 , extrudés dans les mêmes conditions, subit une réduction par un facteur 4 par rapport à l'alliage conventionnel. La formule de Scherer appliquée sur les données de XRD indique qu'après le procédé d'extrusion à chaud, la taille moyenne des cristallites n'augmente que de seulement 10% (~18 nm) dans les composites comparé à environ 400% (~80 nm) dans les alliages monophasés de tellure de bismuth. Comme prévu, la réduction de taille des cristallites mène à une diminution de la conductibilité thermique des composites (~1.4 W/m·K à 450 K pour 0.4% poids MoS_2) comparé à celle des alliages conventionnels (~1.8 W/m·K). Le changement structural dans les nanocomposites caractérisé par spectroscopie mécanique dans la gamme de température 293-540 K montre une augmentation du frottement interne accompagné d'une réduction systématique de l'énergie d'activation par ce mécanisme avec une augmentation du contenu en MoS_2 . Ceci est une indication que l'augmentation de défauts cristallins dans les composites contribue à l'augmentation du niveau de frottement

interne. La mesure des propriétés TE à la température ambiante montre une diminution de la figure de mérite ZT de 0.9 à 0.7 due à un facteur de puissance plus faible. Cependant, au dessus de 370 K, la figure de mérite des nanocomposites contenant du MoS_2 dépasse celle de l'alliage monophasé $(\text{Bi}_{0.2}\text{Sb}_{0.8})_2\text{Te}_3$ due à la plus grande réduction de la conductibilité thermique à une température située au dessus du point de croisement des valeurs de ZT .

Pour les composites du deuxième type, nous avons montré que l'addition de nano-particules de MoS_2 à des alliages de tellure de bismuth permet de réduire significativement la taille de grains de la matrice pour ainsi obtenir une réduction de la conductibilité thermique. L'amélioration de la figure de mérite ZT au dessus de 370 K montre le bénéfice de cette approche, malgré qu'il reste à approfondir les études pour optimiser les propriétés de transport électronique pour améliorer encore plus la figure de mérite.

TABLE OF CONTENTS

DEDICATION	III
ACKNOWLEDGMENTS	IV
ABSTRACT	V
RÉSUMÉ	VIII
TABLE OF CONTENTS.....	XI
LIST OF TABLES	XIV
LIST OF FIGURES.....	XV
LIST OF ABBREVIATIONS AND SYMBOLS.....	XXI
LIST OF APPENDICES.....	XXIV
INTRODUCTION.....	1
CHAPTER 1 STATE OF KNOWLEDGE AND CRITICAL REVIEW OF THE LITERATURE... ..	4
1.1 Introduction to thermoelectricity	4
1.1.1 History and developments	4
1.1.2 Thermoelectric properties.....	5
1.1.3 The figure of merit	7
1.2 Current issues in thermoelectrics	8
1.2.1 Particular thermoelectric nanocomposites.....	10
1.2.2 Random nanocomposites vs. ordered nanocomposites	21
1.3 Bismuth telluride- based alloys.....	23
1.4 The molybdenum disulfide system	29
CHAPTER 2 EXPERIMENTAL METHODS.....	33
2.1 Starting Materials	33

2.2	Synthesis	34
2.3	Characterization techniques and sample preparations	36
2.3.1	Microstructure analyses	36
2.3.2	Atomic structure analyses	36
2.3.3	Phases, elemental, and crystallite size analyses	36
2.3.4	Thermoelectric properties	38
2.3.5	Transport properties	40
2.3.6	Mechanical spectroscopy	41
CHAPTER 3	43
ARTICLE 1: <i>P</i> -TYPE BISMUTH TELLURIDE BASED COMPOSITE THERMOELECTRIC MATERIALS PRODUCED BY MECHANICAL ALLOYING AND HOT EXTRUSION.....		
3.1	Abstract.....	44
3.2	Introduction.....	44
3.3	Experimental procedures	46
3.4	Results and discussion.....	47
3.4.1	Microstructure and grain size.....	47
3.4.2	Carrier transport analysis.....	52
3.4.3	Thermoelectric properties	55
3.5	Conclusion.....	59
3.6	Further discussion	60
CHAPTER 4	61
ARTICLE 2: SYNTHESIS AND CHARACTERIZATION OF BISMUTH TELLURIDE-BASED THERMOELECTRIC NANOCOMPOSITES CONTAINING MoS ₂ NANOCOMPOSITES		
4.1	Abstract.....	62

4.2	Introduction.....	62
4.3	Experimental procedure	63
4.4	Results and discussion.....	64
4.5	Conclusion.....	70
4.6	Further discussion	71
CHAPTER 5.....		72
ARTICLE 3: EFFECT OF SUPPRESSION OF GRAIN GROWTH OF HOT EXTRUDED (Bi _{0.2} Sb _{0.8}) ₂ Te ₃ THERMOELECTRIC ALLOYS BY MoS ₂ NANOPARTICLES		72
5.1	Abstract.....	73
5.2	Introduction.....	73
5.3	Experimental procedure	75
5.4	Results	76
5.4.1	Microstructure and mechanical properties analyses.....	76
5.4.2	XRD analysis	78
5.4.3	TEM observations	80
5.4.4	Thermoelectric properties.....	81
5.5	Discussion.....	85
5.6	Conclusion.....	86
5.7	Characterization of <i>n</i> -type nanocomposite	87
5.7.1	Microstructure.....	87
5.7.2	Thermoelectric properties.....	87
CHAPTER 6 SUMMARY AND GENERAL DISCUSSION		92
CONCLUSIONS AND FUTURE DIRECTIONS		101
BIBLIOGRAPHY		103
APPENDIX.....		125

LIST OF TABLES

Table 2.1 : Powder contamination during mechanical alloying.....	35
Table 3.1: Composition and weight percentage of different phases mixed in powder form to produce composite TE alloys by hot extrusion.	47
Table 3.2 : Lattice parameters of alloys based on Bi, Sb, and Te (adapted from database of X'pert Highscore analyzer software).....	60
Table 6.1 : Comparison between literature and our work on bismuth telluride based nanocomposites with embedded nano-particles. The values are adopted from measurements at 370 K.	100

LIST OF FIGURES

Figure 1.1: Schematic of illustration of Seebeck effect between the junctions of two dissimilar conductors when a temperature gradient is present.	6
Figure 1.2 : The skutterudite crystal structure, metal atoms are the white circles and pnictogen atoms are the black ones [58].	11
Figure 1.3 : Typical crystal structure of half-Heusler alloys [72].	14
Figure 1.4 : Thermoelectric properties of ZrNiSn-ZrO ₂ nanocomposites: (a) electrical resistivity, (b) the Seebeck coefficient, (c) thermal conductivity, and (d) figure of merit [80].	15
Figure 1.5 : Lattice thermal conductivity in PbTe-based nanocomposites with different type of nano-inclusions [29].	16
Figure 1.6 : The microstructure of solidified alloys with the composition of Te-36at.%Sb-5at.%Pb (a) cooled in air, (b) quenched in water [100].	17
Figure 1.7 : Microstructure of transformed Pb ₂ Sb ₆ Te ₁₁ to PbTe and Sb ₂ Te ₃ lamellae by annealing. The darker regions are Sb ₂ Te ₃ , the lighter regions PbTe. (a) annealed at 500 °C for 5 days, (b) annealed at 400 °C for 5 days, (c) annealed at 300 °C for 5 days [98].	18
Figure 1.8 : TEM images of (a) Bi _{0.3} Sb _{1.7} Te ₃ matrix (b) magnified area of panel a, (c) SiC nano-particle in the matrix, (d) HRTEM image of the interface between SiC nano-particle and the matrix [111].	20
Figure 1.9 : Microstructure of water-quenched Bi ₂ Te ₃ -PbTe alloys with chemical composition of: (a) Pb ₂ Bi ₂ Te ₅ and, (b) PbBi ₆ Te ₁₀ [112].	21
Figure 1.10 : Schematic of random nanocomposites (a-e), and ordered nanocomposites (f-j) [29].	22
Figure 1.11 : Hexagonal representation of bismuth telluride crystal structure. Bi atoms in blue spheres and Te atoms in purple [118].	24
Figure 1.12 : Plot of the ratio of electrical conductivities of single crystal bismuth telluride at 300 K in the a-direction (σ_a) and c-direction (σ_c) vs. σ_a [1].	25

Figure 1.13: Seebeck coefficient of bismuth telluride as a function of Te at.%. Dash line indicate at around 62 at.% the conduction mode of bismuth telluride changes [123].	26
Figure 1.14: Plot of lattice thermal conductivity against molar percentage of Sb_2Te_3 in solid solutions of $(\text{Bi-Sb})_2\text{Te}_3$ (based on data of Birkholz, Goldsmid, and Rosi et al. [24]).	27
Figure 1.15: Plot of lattice thermal conductivity at 300 K against molar percentage of Bi_2Se_3 in solid solutions of $(\text{Bi-Sb})_2\text{Te}_3$ [1].	28
Figure 1.16: The thermoelectric figure of merit plotted against electrical conductivity for <i>n</i> -type and <i>p</i> -type solid solutions and pure compound of bismuth telluride [1].	28
Figure 1.17: Crystal structure of molybdenum disulfide and distances between its atomic layers [140].	30
Figure 1.18 : Size-dependent electronic band structure of MoS_2 . The bottom of the conduction band (in red) and top of the valance band (in blue) are highlighted. The Fermi level is set at 0 eV and the arrow shows the smallest value of the indirect or direct band gap [146].	31
Figure 1.19 : Schematic of different edge configurations in (a) MoS_2 monolayer, (b) side view of monolayer, (c) top view of MoS_2 monolayer. The horizontal orientation shows the armchair configuration and the vertical orientation shows the zigzag configuration [148].	32
Figure 2.1 : Elemental pellets of starting materials used to synthesize bismuth telluride based alloys.	33
Figure 2.2 : Morphology of MoS_2 nano-particles as provided by supplier.	34
Figure 2.3 : Schematic of attrition system used for mechanical alloying.	35
Figure 2.4 : An example of samples prepared for XRD analyses. The upper surface is ground with SiC grinding paper (1200 grit), then polished using slurry of Alumina (particles < 0.05 microns).	38
Figure 2.5: Samples prepared for TE properties measurement.	39
Figure 2.6: Schematic of voltage vs. time graph for a TE material once the current is switched off.	40
Figure 2.7: Samples prepared for Hall Effect measurements.	41

Figure 2.8 : Schematic of MS setup as sample installed in the furnace.	42
Figure 3.1: Microstructure of homogenous part of the extruded rods in conventional alloy (a) and composite #6 (b) obtained by using Secondary electron images. The porosity is typical for hot extruded alloys.	49
Figure 3.2: Backscattered electron images showing the microstructure at the beginning of the extruded rods in conventional alloy (a), and in composite #5 (b). Observe the grains size reduction and the lamellae within grains (stacking faults or twins). They are much smaller in the composites.	50
Figure 3.3 : Evolution of peak broadening in the composites for the (110) and (113) diffracting planes. There is no conclusive evidence of separate peaks in these curves.	51
Figure 3.4: Calculated crystal sizes from XRD data of extruded composites and conventional alloy from the homogenous part of the rods (blue diamonds) and from the beginning of the extruded rods (red triangles). Inserted XRD patterns for conventional alloy and composite #6 illustrate peak broadening (patterns taken from the homogeneous part).	52
Figure 3.5: (a) Hole Hall Mobility vs. temperature obtained from Hall measurements in the range 15-360K, (b) Conductivity vs. temperature from Harman measurements in the range 290-380K.	54
Figure 3.6: Inverse Hall mobility vs. carrier concentration at T=15K acquired from Hall measurements.	55
Figure 3.7: Peak ZT values of all composites and conventional alloy for both beginning (red squares) and homogenous part (blue diamonds) of the extruded rods. The solid line is included to highlight the decrease in peak ZT values in composites.	56
Figure 3.8: Maximum power factor of the conventional alloy and of the composites as was measured by our Harman setup. The solid line is included as a guide showing the overall tendency of the power factor.	57
Figure 3.9: Thermal conductivities of the composites and the conventional alloy as were obtained by Harman measurements. The solid line is included to highlight the upward trend.	58

- Figure 3.10: The composition (from Table 3.1) of the constituents of the composite materials (# on right axis) showing the molar percentage of Sb_2Te_3 in each phase (phase 1: green diamonds and phase 2: red squares). The graph also shows the values of the thermal conductivity (left axis) taken from the literature [24]..... 58
- Figure 4.1: HRTEM images of (a) decorated grains of $(\text{Bi}_{0.2}\text{Sb}_{0.8})_2\text{Te}_3$ with nano-flakes of MoS_2 in extruded nanocomposite containing 0.8 wt.% MoS_2 , (b) MoS_2 nano-flake with few atomic layers decorating a grain in a extruded nanocomposite with 0.2 wt.% MoS_2 , (c) several MoS_2 nano-particles (indicated by arrows) dispersed in the matrix of an extruded nanocomposite with 0.4 wt.% MoS_2 and (d) EDX spectrum of indicated area in panel (b). 65
- Figure 4.2: Backscattered electrons SEM images revealing: (a) the microstructure of a conventional single phase $(\text{Bi}_{0.2}\text{Sb}_{0.8})_2\text{Te}_3$ alloy (0 wt.% MoS_2), (b) the sub-micron matrix grains in $(\text{Bi}_{0.2}\text{Sb}_{0.8})_2\text{Te}_3:\text{MoS}_2$ nanocomposite containing 0.4 wt.% MoS_2 66
- Figure 4.3: Peak broadening in nanocomposites (a) selected peaks corresponding to (110) plane, (b) crystallite sizes of the powders and extruded samples of conventional alloy and nanocomposites, as determined by Scherrer's formula. 67
- Figure 4.4: (a) Measurements of the internal friction of nanocomposites with different amount of MoS_2 nano-particles compared with conventional alloys, as a function of absolute temperature; (b) Arrhenius plot of p-type nanocomposites, and (c) illustration of the internal friction activation energy trend as a function of MoS_2 content..... 68
- Figure 5.1: SEM images of the fracture surfaces perpendicular to the extrusion axis of a) conventional $(\text{Bi}_{0.2}\text{Sb}_{0.8})_2\text{Te}_3$ alloy (0 wt.% MoS_2), and nanocomposites with b) 0.2 c) 0.4 d) 0.8 wt.% MoS_2 77
- Figure 5.2: Young's modulus measured by mechanical spectroscopy as a function of temperature and MoS_2 content..... 78
- Figure 5.3: (a) X-ray diffraction patterns of extruded samples with different amount of MoS_2 nanoparticles, (b) Peaks' broadening in nanocomposites compared to the alloy without MoS_2 79
- Figure 5.4: Crystallite sizes of the powders and extruded samples of conventional alloy and nanocomposites calculated from XRD peak broadening using Scherrer's formula. 80

- Figure 5.5: TEM images of (a) dispersed nano-flakes which decorate the matrix grains in extruded nanocomposite with 0.4 wt.% of MoS_2 , (b) extruded nanocomposite with 0.4 wt.% MoS_2 and (c) EDX spectra of positions labeled 1-3 in panel (b). 81
- Figure 5.6: (a) Electrical conductivity (log-log scale) and (b) thermal conductivity of *p*-doped samples as a function of temperature. Both conductivities are measured on a plane containing the extrusion axes (except for the case of one sample, measured perpendicular to the extrusion axis, represented by solid triangles guided by a dashed line). 83
- Figure 5.7: (a) Comparison of *ZT* values as a function of temperature of the conventional $(\text{Bi}_{0.2}\text{Sb}_{0.8})_2\text{Te}_3$ compound with samples containing 0.4 wt.% MoS_2 obtained with different processing parameters, (b) comparison of the Seebeck coefficient of samples in panel (a). As in the previous figure, one of the samples is measured in a direction along the extrusion axis (solid triangles guided by a dashed line). 84
- Figure 5.8: SEM images of the fracture surfaces perpendicular to the extrusion axis of a) *n*-type $(\text{Bi}_{0.95}\text{Sb}_{0.05})_2(\text{Te}_{0.95}\text{Se}_{0.05})_3$ alloy (0 wt.% MoS_2), and (b) *n*-type nanocomposite with 0.3 wt.% MoS_2 87
- Figure 5.9: Electrical conductivity of *n*-type conventional and nanocomposite materials with 0.3 wt.% of MoS_2 as function of absolute temperature (log-log scale). The measured values in the direction parallel to the extrusion direction are presented for both conventional (red triangles) and nanocomposite (blue circles), as well as values measured on a plane perpendicular to the extrusion axis for the nanocomposite sample (blank squares). 88
- Figure 5.10: Thermal conductivity of *n*-type conventional and nanocomposite samples (with 0.3 wt.% MoS_2). The blank squares show the measured value for the nanocomposite sample along a direction perpendicular to the extrusion axis. 89
- Figure 5.11: *ZT* values of *n*-type conventional and nanocomposite samples as a function of temperature. As in the previous figure, one of the samples is measured in a direction perpendicular to the extrusion axis. 90
- Figure 5.12: Seebeck coefficients of *n*-type conventional and nanocomposite (0.3 wt% MoS_2) samples as a function of temperature. Values of nanocomposite sample shown by blank squares were measured in the direction perpendicular to the extrusion axis. 91

Figure 6.1: Mean crystallite size of powders after milling (circles) and sintered samples (squares) of bismuth telluride based nanocomposites as a function of fullerene concentration [180]. .95

LIST OF ABBREVIATIONS AND SYMBOLS

Abbreviation	Meaning
CNTs	Carbon Nanotubes
EDS	Energy dispersive spectroscopy
FEG-SEM	Field emission gun – scanning electron microscope
HH	Half-Heusler
HRTEM	High resolution transmission electron microscope
IET	Impulse excitation technique
MS	Mechanical spectroscopy
PF	Power factor
TE	Thermoelectric
XRD	X-ray powder diffraction
IF	Internal friction

Symbol	Meaning (Unit)
ZT	Dimensionless figure of merit
α	Seebeck coefficient ($\mu\text{V}/\text{K}$)
V	Electric potential (Volts)
T	Absolute temperature (K)
ΔT	Temperature difference (K)
α_{AB}	Differential Seebeck coefficient of conductors A and B ($\mu\text{V}/\text{K}$)
Π	Peltier coefficient (Volts)
q	Heating rate (W)

I	Electric current (A)
τ	Thomson coefficient (V/K)
Z	Figure of merit (1/K)
λ	Thermal conductivity (W/mK)
σ	Electrical conductivity (S/m)
λ_e	Electronic thermal conductivity (W/mK)
λ_{ph}	Lattice thermal conductivity (W/mK)
n, p	Charge carriers density (cm^{-3})
e	Electron charge (Coulombs)
μ	Charge carrier mobility ($\text{cm}^2/(\text{V}\cdot\text{s})$)
ρ	Electrical resistivity (Ωcm)
L	Lorenz number ($\text{W}\Omega\text{K}^{-2}$)
K_B	Boltzmann constant ($1.3806488 \times 10^{-23} \text{ m}^2 \text{ kg s}^{-2} \text{ K}^{-1}$)
E_f	Fermi energy (eV)
λ	X-ray radiation wavelength (Angstrom)
D	Average crystallite size (nm)
B	Full width at half maximum (Degree)
θ	Diffraction angle (Degree)
ΔX	Difference in electronegativities (eV)
E	Young's modulus (GPa)
E_C	Young's modulus of composite material (GPa)
E_m	Young's modulus of matrix phase of composite (GPa)
E_{np}	Young's modulus of nano-particles in the composite (GPa)
V_m	Volume fraction of matrix of composite (vol.%)

V_{np}	Volume fraction of nano-particles in the composite (vol.%)
IF_{bg}	Internal friction background

LIST OF APPENDICES

APPENDIX A – LIST OF AUTHOR’S CONTRIBUTIONS DURING THIS PROJECT...125

INTRODUCTION

When fossil fuel resources are becoming exhausted, followed by the environmental issues, the emerging global need for alternative energy sources, conservation, and management has increased interest in more effective, clean, and sustainable resources of power generation. Thermoelectric devices can be used as power generators or cooling devices. Despite high cost and relatively low efficiency of thermoelectric materials, which are used in these devices, there are some features under development that make them a promising alternative in energy conversion. Thermoelectric materials can play an important role in energy conservation (i.e. waste heat harvesting) if efficient, stable, and inexpensive novel materials can be developed. Thermoelectric generators are solid-state generators with no moving parts and minimum maintenance needed. These devices are environmentally friendly, silent, and reliable. The most clearly defined application of thermoelectricity is in energy recovery from waste heat. Currently, due to relatively high cost and low efficiency, thermoelectric materials are employed in limited applications. However, there are still key applications of thermoelectric devices where their restrictive parameters are not prohibitive. Nonetheless, more efficient materials need to be identified in order to extend their use in power generation and cooling applications.

Bismuth telluride based alloys are the most promising thermoelectric materials for near room temperature applications due to their low thermal conductivity and large Seebeck coefficient. However, the efficiency of these materials has not been significantly improved during the last 40 years.

During the past decade, several reports have shown improvement in thermoelectric performance. Most of these advances have been connected with the use of nanostructures. One of the most efficient values in the bismuth telluride system has been obtained from a superlattice based on bismuth telluride and antimony telluride. In this case, the improvement of the performance can be related to the lattice conductivity reduction [1]. Addition of nano-inclusions to increase interfaces has shown a significant impact on lattice thermal conductivity reduction despite its simultaneous effect on electrical conductivity [2, 3]. Alternatively, composite thermoelectric materials containing several phases may enhance the performance of thermoelectric materials by conserving a relatively high electrical conductivity while introducing more interfaces leading to a decrease in the thermal conductivity. Although several reports on synthesis of composite

thermoelectric materials have been published [4-12], the production of bulk bismuth telluride based thermoelectric composites including several constituent phases of the same family has not been reported, and its consequences on thermoelectric and transport properties have not been studied. Also, synthesis approaches to obtain nanostructure thermoelectric materials, which are amenable to mass production for industrial applications, would attract more interests. On the other hands, one of the main concerns when synthesizing nanostructured thermoelectric alloys is to conserve the nanostructure and inhibit grain growth. Making diffusion barriers at grain boundaries such as adding nano-inclusions, or mixing dissimilar phases when making composite thermoelectrics, may suppress the grain growth.

The basis of the present Ph.D. work is the production of nanostructured bismuth telluride based thermoelectric nanocomposites. These composites contain different phases such as binary, ternary, or quaternary alloys of Bi, Te, Sb, and Se, and/or nano-inclusions of molybdenum disulfide (MoS_2). These alloys are produced by mechanical alloying, and then mixed and consolidated via hot extrusion.

The general objectives of this dissertation besides a contribution to advance the knowledge in the field of bulk thermoelectric nanocomposites, were to employ cost and time efficient techniques to synthesize and produce bulk TE composites with possibility of commercialization and mass production, also to establish the relation between structure and thermoelectric properties of these materials with the aim to shed light on their functional properties.

The specific objectives of this work were to study the differentiation of transport properties, microstructures, atomic structures, and phases' distribution of nanostructured bismuth telluride based composites in comparison with single phase alloy material. Evaluation of the thermoelectric and mechanical properties of conventional single phase and composite bismuth telluride based materials, and comparison of thermoelectric properties of produced composites with theoretical expectations are another objectives of this dissertation.

We expect the myriad nanoscopic interfaces produced by means of these nanocomposites, which according to the theoretical and experimental investigations described in Chapter 1, effectively reduce the lattice thermal conductivity, thus improving the thermoelectric performance.

This Ph.D. dissertation includes a brief review on the history, theories, and current issues of thermoelectricity and thermoelectric materials and a literature review on efforts to make

thermoelectric nanocomposites and hypothetical as well as practical approaches to obtain nanocomposite thermoelectrics with enhanced performances. In addition to these topics, the atomic and electronic structures of the constituent phases of composites are presented in Chapter 1. The experimental methods such as basis of materials synthesis, characterization techniques, and samples specifications are given in Chapter 2.

The efforts whose results establish this research work as a Ph.D. dissertation are multifaceted, and indicated below as research efforts A-D.

A – Synthesizing thermoelectric composites containing Bi-Sb-Te based phases –

In Chapter 3 (Manuscript 1), we report production of six different composites of *p*-type bismuth antimony telluride alloys.

B – Synthesizing the MoS₂ nano-inclusion embedded thermoelectric nanocomposites –

Production of four different nanocomposites incorporated with MoS₂ nano-inclusions is reported in Chapter 4 (Manuscript 2).

C – Microstructures, phases, and atomic structures characterization of composites –

Analyses of microstructure, phases and crystallite sizes are provided in Chapters 3, 4, and 5 (Manuscript 3).

D – Thermoelectric properties characterization –

Results and analyses of thermoelectric properties of composites such as electrical conductivity, thermal conductivity, Seebeck coefficient and figure of merit, are described in Chapter 3 and Chapter 5.

Finally, a general discussion of this research is presented in Chapter 6, followed by the conclusion.

Chapter 1 **STATE OF KNOWLEDGE AND CRITICAL REVIEW OF THE LITERATURE**

In this chapter, an overview of theories related to principles of thermoelectricity is given. In addition, current issues in processing thermoelectric (TE) materials with enhanced performance, and proposed approaches to improve the performance of TE materials are reviewed. Moreover, the crystal structures as well as the electronic and thermal properties of alloys used in this Ph.D. work will be described.

1.1 Introduction to thermoelectricity

In this section, a short review of discovery and developments of thermoelectricity and TE materials is given. TE properties and principles are reviewed.

1.1.1 History and developments

The earliest reported discovery on thermoelectricity dates back to 1821, when Thomas Johan Seebeck observed for the first time a direct conversion between thermal and electrical energy [13]. Seebeck observed that a compass magnet would deflect when it is close to a circuit made from two dissimilar metals, with junctions at different temperatures [14]. In other words, the temperature difference at the junctions of two dissimilar metals produces an electric potential. Nowadays, this effect is known as the Seebeck effect.

In 1834, Jean Charles Athanase Peltier found that an electrical current would produce heating or cooling at the junction of two dissimilar metals. In 1838, Lenz revealed that depending on the direction of current flow, heat can be generated, or by reversing the current flow, heat could be absorbed from a given junction. The heat which is absorbed or created at the junction is proportional to the electrical current. Later, this proportionality constant was called the Peltier coefficient [15].

William Thomson (Lord Kelvin) found and described the interrelationship between Seebeck and Peltier effects. The third thermoelectric effect, which is now termed “Thomson effect”, describes relations between the Seebeck and Peltier coefficients through thermodynamics. The Peltier coefficient is simply the Seebeck coefficient times absolute temperature [16]. However, research in thermoelectricity and TE materials did not show promising developments until 1950 when

Abram Fedorovich Ioffe found that doped semiconductor alloys would have better thermoelectric performance than pure metals. He also developed the modern theory of thermoelectricity using the concept of *figure of merit* (ZT), to show the performance of TE materials [17, 18]. This spurred research in thermoelectricity and today, considerable numbers of new TE materials have been developed. During the 1990's, the new ideas that making engineered structures and nanometer scale TE materials will improve ZT , renewed interests in thermoelectricity [19-21].

1.1.2 Thermoelectric properties

In this section, the definitions of the Seebeck and Peltier coefficients are presented, as well as how they are related to one another.

The Seebeck coefficient, also known as thermopower or thermoelectric power, α , represents the power of the Seebeck effect. When there is a conductor (A) joined at both ends to another conductor (B), and B is divided in two parts being connected to a voltmeter (Figure 1.1), then by establishing a temperature difference ΔT between the two junctions, a potential difference V will appear between the free ends (which can be measured by the voltmeter). The differential Seebeck coefficient is defined as,

$$\alpha_{AB} = \frac{V}{\Delta T} \quad (1.1)$$

The typical unit of Seebeck coefficient is $\mu\text{V}/\text{K}$. Intuitively, the establishment of a temperature gradient causes electron diffusion between the two sides of the junction. Electrons in the hot region become more energetic than those in the cold region, thus, there is a relative difference in electron velocities which implies a net diffusion of electrons from hot region to the cold region. As a result, the sign of the Seebeck coefficient is typically negative for n -type materials, where electrons are the majority charge carriers, and positive for p -type materials, where holes are the primary carriers [1, 18].

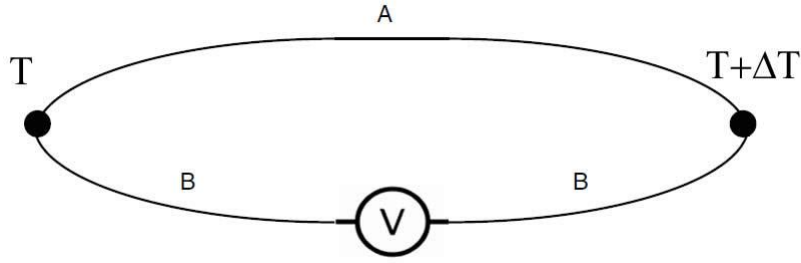


Figure 1.1: Schematic of illustration of Seebeck effect between the junctions of two dissimilar conductors when a temperature gradient is present.

The representation of the strength of the Peltier effect is the Peltier coefficient, Π , which is defined as the ratio of the rate q of heating or cooling at each junction of two dissimilar conductors to the applied electric current I ,

$$\Pi_{AB} = \frac{q}{I} \quad (1.2)$$

By applying an electric current across a junction of two dissimilar conductors, the rate of heating (cooling) will be different through each material. Consequently, heat will be either absorbed (cooling) or produced (heating) at that junction. Heating or cooling will be reversed by changing the polarity of the electric current at the junction due to the inversion of heat flow between two conductors[1, 18].

In the Thomson's studies, as mentioned earlier in this chapter, the Peltier coefficient in terms of the Seebeck coefficient is expressed by this equation,

$$\Pi_{AB} = \alpha_{AB} T \quad (1.3)$$

where T is the absolute temperature of the materials. The Thomson effect describes the production or absorption of heat from a material that is exposed to both temperature and voltage gradient [1, 18], through the Thomson coefficient, τ , which is related to the Seebeck coefficient, and in fact evaluates the magnitude of the Thomson effect by the following equation:

$$\tau = T \frac{d\alpha}{dT} \quad (1.4)$$

1.1.3 The figure of merit

The essential goal of using thermoelectric materials is energy conversion. In order to evaluate the thermoelectric performance of a material, its efficiency in energy conversion of TE devices has to be assessed. The efficiency of TE devices translates into a *figure of merit* for materials, a parameter, Z , with dimension of K^{-1} , which is given by

$$Z = \frac{\alpha^2 \sigma}{\lambda} \quad (1.5)$$

where α is Seebeck coefficient, σ is the electrical conductivity, and λ is the thermal conductivity of the material. However, mostly, the more practical *dimensionless figure of merit*, ZT , which is obtained by multiplying the figure of merit by the absolute temperature, T , is often used [1, 18, 22]. Knowing and understanding Z and its related parameters (in equation (1.5)), one can analyze and develop a TE material. In section 1.1.2, the Seebeck coefficient and its relation to other TE effects were described. The other parameters of interest in evaluation of the figure of merit of TE materials are the electrical and thermal conductivities. Transport of energy by both electrons and phonons (which are quanta of lattice vibrations modes in a crystal) contributes to thermal conduction of materials [23, 24]. The total thermal conductivity, λ , can then be written as:

$$\lambda = \lambda_e + \lambda_{ph} \quad (1.6)$$

Electrical conductivity is dependent on the ability of the charge carriers to travel through a material, under an applied external field. The charge carrier mobility, μ , illustrates how quickly the charge carriers responds to an electric field and travel through the material. The movement of charge carriers can be limited by collisions with lattice imperfections, impurities, and phonons. In semiconductors, there are in general two types of carriers contributing to the electrical conductivity, which each one (n or p) has the form

$$\sigma_{n,p} = ne\mu \quad (1.7)$$

where e is the magnitude of the electron charge, n is the concentration of charge carriers (usually denoted by p for positive carriers (or holes))[22, 25]. Hence, the total electrical conductivity is given as

$$\sigma = \sigma_n + \sigma_p \quad (1.8)$$

Thermal conductivity and electrical conductivity are both dependent on charge carrier transport, and are related by Wiedemann-Franz law. This means that efforts to increase electrical conductivity to enhance ZT , will result in an increased thermal conductivity as well. In another words, since these parameters are interdependent it is challenging to find adequate ways to enhance the figure of merit. The most studied way to improve ZT , is by thermal conductivity reduction. It is well known that amorphous materials or glass have the lowest thermal conductivity of solid materials. This led to the idea of a thermoelectric material with a glass-like thermal conductivity when it has crystal-like electronic properties [1].

When a semiconductor has a high electrical resistivity, then heat conductivity is mainly dominated by lattice vibrations (phonons), although in some semiconductors the contribution of the electronic component of the thermal conductivity is high enough to make it important. Thus, it is necessary to separate the contributions of lattice and electronic components to the thermal conductivity [24, 26-28]. The lattice thermal conductivity can be reduced by the scattering of phonons on various types of defects. These could be point, line and volume (bulk) defects such as ions, impurities, dislocations, grain boundaries or particles as well as nano-inclusions. In a system containing dissimilar materials or when an abrupt dimensional mismatch occurs, interfaces may be responsible for significant phonon scattering [1, 24].

1.2 Current issues in thermoelectrics

As we discussed in the previous section, the figure of merit is entirely dependent on the electrical conductivity, the thermal conductivity, and the Seebeck coefficient. The power factor (PF), of TE materials is defined as

$$PF = \frac{\alpha^2}{\rho} = \alpha^2 \sigma \quad (1.9)$$

where ρ is the electrical resistivity. In the 1950's and 60's, TE researches mostly focused on the PF improvement, obviously, by making efforts to increase the electrical conductivity and/or Seebeck coefficient when the thermal conductivity is not affected. Nevertheless, as it is shown in section 1.1.3, thermal conductivity has an electronic contribution (λ_e), which according to the

Wiedemann-Franz equation, is represented by a component of thermal conductivity directly proportional to the electrical conductivity [27]:

$$\lambda_e = L\sigma T \quad (1.10)$$

Here, L stands for Lorenz number, which in the case of thermoelectric materials is mostly within a range of $1.6 - 2.2 \times 10^{-8} \text{ W}\cdot\Omega/\text{K}^2$ [29].

Although the Lorenz number is not constant for all thermoelectric materials, and each material has a specific Lorenz number, this range can help to provide a rough estimation of the electronic contribution to the thermal conductivity. The difficulties arise in improving ZT since any attempt to enhance the electrical conductivity leads to a corresponding increase in the thermal conductivity. Moreover, the Seebeck coefficient is proportional to the logarithmic derivative of the electrical conductivity according to the Mott formula [30, 31],

$$\alpha = \frac{\pi^2}{3} \left(\frac{k_B^2 T}{e} \right) \left(\frac{d \ln \sigma}{dE} \right)_{E_f} \quad (1.11)$$

where k_B represents the Boltzmann constant, e is the electron (carrier) charge, and E_f stands for the Fermi energy. This equation shows the interrelations between electrical conductivity and Seebeck coefficient that introduce more challenges to maximize the figure of merit.

To sum up, between two main approaches to optimize and maximize the figure of merit, which are; power factor boost, and lattice thermal conductivity reduction, the latter one is the easier to implement, since a single parameter is involved to achieve the goal.

Some of suggested methods to lower the lattice thermal conductivity are; making alloys and solid solutions, increasing the average atomic mass [1], and using materials with intrinsic complex structures [32, 33]. However, it was in the 1990's that for the first time the idea of using low dimensional structures to enhance the figure of merit was presented [34, 35]. Though that proposed theoretical framework to increase the figure of merit was based primarily on enhancement of power factor due to quantum confinement effects rather than from any thermal conductivity reduction [36]. Later, a work on $\text{Bi}_2\text{Te}_3/\text{Sb}_2\text{Te}_3$ superlattices, and soon after another study on $\text{PbTe}/\text{PbSe}_x\text{Te}_{1-x}$ superlattices showed ZT enhancement due to phonon scattering at the interfaces between layers in superlattice structures [37, 38]. These results began to attract interest in TE research to reduce thermal conductivity by phonon scattering.

However, due to the thin morphologies of superlattices, they are more studied in thin film applications than in bulk applications. In order to utilize the benefits of low dimensional morphologies within bulk applications the concepts of composite and nanocomposite have been followed by several TE research groups during the last ten years. One of the earliest reported studies to produce such a TE composite involved the incorporation of 9-15 nm diameter Bi nanowires into porous alumina and porous silica [39].

The words, *composite* and *nanocomposite*, in the thermoelectric related literature are used with different meanings. In some reports, nanocomposite refers to adding nano-inclusions to the bulk thermoelectric materials [40, 41], in some others, it pertains to mixing two or more different particle sizes ranging from nano to micro-scale of the same material [42], or mixing two different TE phases [43]. In general, one can call a material, a TE nanocomposite when it consists of nano-inclusions, nano-particles randomly dispersed, nano-grains, and secondary phases or precipitates. More recently several approaches have been developed to produce TE nanocomposites mainly based on the idea of the phonons scattering by introducing more interfaces in the material, such as utilizing phase decomposition to create embedded nanostructures [44, 45]. Several types of nano-inclusions such as semimetals, semiconductors, metals, ceramics, and even carbon nanotubes were also used in thermoelectric materials to produce TE nanocomposites [40, 41, 46, 47].

1.2.1 Particular thermoelectric nanocomposites

There are several groups and families of TE materials including semimetals, semiconductors, and ceramics in different crystalline forms and various dimensions [48-54]. Recently, even some polymers retained attentions by their interesting TE properties [55-57]. However, in this section, some of the scientific works on bulk TE nanocomposites with a special focus on the well-known classified compounds are reviewed.

1.2.1.1 Skutterudites

Filled skutterudites are among the most promising TE materials. Skutterudites comprise compounds with a general formula of MX_3 (where M is Co, Rh, or Ir, and X is a pnictogen atom like P, As, or Sb) [29, 58]. The typical crystal structure of skutterudites is depicted as in Figure 1.2. In this structure, the metal atoms M forming a simple cubic sub-lattice and pnictogen atoms X placed in planar, near-square rings.

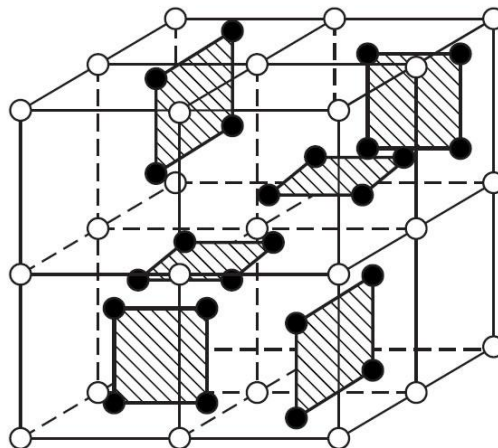


Figure 1.2 : The skutterudite crystal structure, metal atoms are the white circles and pnictogen atoms are the black ones [58].

Looking to the skutterudites crystal structure, it is easy to see the open nature of the structure. In fact, two of the eight cubes in the structure remain empty. These empty spaces in the structure are called voids of the structure. Filling these voids by atoms of other elements such as ions of rare-earths, alkaline earths, or alkali metals, results in the formation of filled skutterudites. These materials are suitable for electronic as well as lattice properties modifications, which make them potential TE materials [29, 58].

Recently, several reports showed the interest of making nanocomposites of skutterudites by introducing nano-inclusions into the skutterudite matrix [59-64]. These studies are mostly on the cobalt triantimonide based materials due to their electrical properties (high carrier mobility and large effective mass). However, the high thermal conductivity of these materials is the main issue that remains unsolved to maximize their TE performance [65]. Indeed, adding nano-inclusions could be an option to reduce thermal conductivity and improve the TE properties.

Chubilleau et al. [64] reported a study of adding ZnO nano-inclusions to CoSb_3 skutterudite. They added 2-12 wt.% of ZnO nano-particles to the synthesized CoSb_3 particles and sintered the mixtures by spark plasma sintering (SPS) technique. Their results showed a significant enhancement in the Seebeck coefficient values in addition to a decrease in the thermal conductivity. However, the smallest amount of nano-inclusions (i.e. 2 wt.%) had the most beneficial effect on the figure of merit while the sample with 12 wt.% ZnO nano-inclusions showed a drastic increase in electrical resistivity. Another report from this research team

investigated the effect of PbTe inclusions on the CoSb₃ skutterudite. In this report [63], nanoparticles of PbTe (6 nm in diameter) were introduced, in various wt.% from 0 to 8, into CoSb₃ skutterudite matrices. They showed that PbTe-CoSb₃ TE composites are *n*-type materials whereas the single phase CoSb₃ skutterudite is a *p*-type semiconductor. They claimed that this change in the conduction mode is due to the small amount of Sb for Te substituting in the composites. Also, the agglomerates of PbTe were observed at grain boundaries. Thermal conductivity reduction was observed for all composites regardless of the amount of nano-inclusions in the material. Fu et al. [66] used AgSbTe₂ nano-inclusions in Yb_{0.2}Co₄Sb₁₂ filled skutterudite to make TE nanocomposites. They added 2, 4, and 8 wt.% of the nano-inclusions in the matrix and investigated the TE properties. It was shown that the electrical conductivity of these nanocomposites is higher than that of the matrix single phase sample. The proposed explanation involves two reasons; the added nano-inclusions are *p*-type semiconductors, while the matrix has an *n*-type conduction mode, therefore, the charge carrier concentration of the nanocomposites decreased as the nano-inclusion content increased, but carrier mobility increased by a factor of three. Furthermore, AgSbTe₂ nano-inclusions precipitated at the grain boundaries of the matrix, which as it is claimed, led to improvement in electrical conductivity at grain boundaries. As it is reported, there is an energy barrier with a height of about 0.48 eV at the boundaries of nano-inclusions and the filled skutterudite matrix. This barrier needs to be overcome by the charge carriers leading to low energy electrons filtration. As a result, enhancement of the Seebeck coefficient is achieved. Although the lattice thermal conductivity of nanocomposites in this study decreased, there is an increment in the electronic contribution to their thermal conductivity, thus, there is no systematic relation between the amount of nano-inclusions and the total thermal conductivity. However, due to the simultaneous increment of the Seebeck coefficient and the thermal conductivity reduction in the nanocomposites, their reported *ZT* values of these nanocomposites improved. The maximum *ZT* was obtained for the nanocomposites with 4 wt.% of AgSbTe₂ nano-inclusions at 300 K, which is one of the best reported *ZT* values (1.27 at about 600 K) in the skutterudite based composites [59, 61, 66-69].

Besides using nano-inclusions in skutterudites to reduce the lattice thermal conductivity, a remarkably low lattice thermal conductivity was observed in the single-, double-, and triple-filled skutterudites. For instance, the lattice thermal conductivity of triple-filled Ba_uLa_uYb_wCo₄Sb₁₂ is reported as low as 1-2 Wm⁻¹K⁻¹ at 300 K and ~ 0.2 Wm⁻¹K⁻¹ at 800 K (samples without filling

showed lattice thermal conductivity between 4-6 $\text{Wm}^{-1}\text{K}^{-1}$ at 300 K and between 2-4 $\text{Wm}^{-1}\text{K}^{-1}$ at 800 K). Although there are still some disagreements on the lattice thermal conductivity of multiple-filled skutterudites at high temperatures yet the multiple-filling certainly reduced the lattice thermal conductivity of these materials in several reports [70, 71].

1.2.1.2 Half-Heuslers

The half-Heusler (HH) alloys with the general formula of ABC are one of the well-known intermetallic compounds. These alloys crystallize in the cubic structure that could be understood as a simple rock salt structure which formed by atoms of type A and C, and filled by atoms of type B at one of the two body diagonal positions (see Figure 1.3) [72]. HH alloys are suitable TE materials for high temperature applications due to their high temperature stability [73]. The reported HH nanocomposites are mostly nano-inclusion embedded HH alloys or with nano-scale precipitates within the matrix. Nano-particles of ZrO_2 , C_{60} , $\gamma\text{-Al}_2\text{O}_3$, WO_3 , and NiO are used as nano-inclusions in the HH matrix [74-86]. Huang et al. reported a 35% reduction of thermal conductivity by the addition of 6 vol% ZrO_2 nano-inclusions to a ZrNiSn matrix compared to the single phase alloy. This led to a 15% improvement in the ZT value of this nanocomposite at 900 K in contrast to the pure ZrNiSn compounds (see Figure 1.4) [80]. Another study of HH nanocomposites showed that the lattice thermal conductivity of nanocomposites of $\text{Zr}_{0.5}\text{Hf}_{0.5}\text{Ni}_{0.8}\text{Pd}_{0.2}\text{Sn}_{0.99}\text{Sb}_{0.01}\text{-ZrO}_2$ with 3, 6, and 9 vol% ZrO_2 nano-inclusions approximately reduced 5%, 14%, and 34%, respectively, compared with the lattice thermal conductivity of matrix phase. Besides the action of nano-inclusions as phonon scattering centers, this relatively big impact on the lattice thermal conductivity reduction was explained by the induced defects in the material by adding nano-inclusions [85]. In addition to the effect of ZrO_2 nano-inclusions on thermal conductivity of HH nanocomposites, Poon et al. and Chen et al. reported the energy filtering effect in HH- ZrO_2 nanocomposites, but this energy filtering effect was not strong enough to considerably improve the Seebeck coefficient [85, 86].

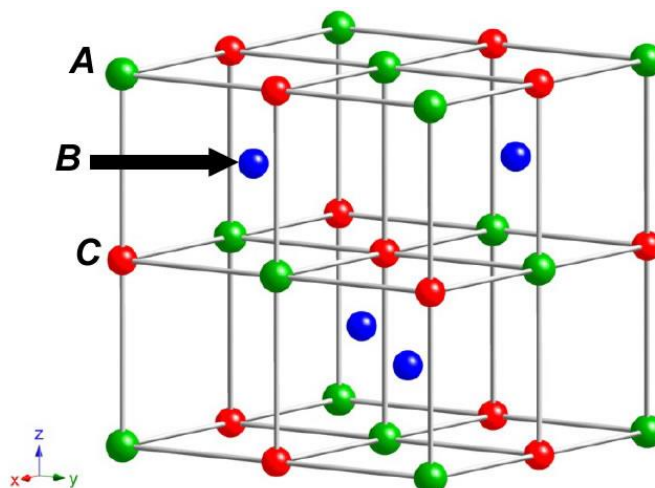


Figure 1.3 : Typical crystal structure of half-Heusler alloys [72].

Another approach to produce HH nanocomposites is the formation of nano-scale precipitates within the homogeneous matrix. Xie et al. reported the formation of nano-scale InSb inclusions in the MCoSb (M= Ti, Zr, or Hf) system. By addition of In into the mixed starting materials during the induction melting, indium could react with antimony and resulted in the formation of nano-precipitates [82]. They experimentally showed that by formation of this nano-scale phase in the matrix, the Seebeck coefficient, electrical conductivity, and thermal conductivity could be tuned somewhat individually. By formation of these nano-precipitates, the InSb phase injects electrons that can increase the carrier concentration (electrical conductivity) of the HH nanocomposite, and the interfaces between the precipitates and matrix act as a potential energy barrier resulting in an improvement of the Seebeck coefficient. In the meantime, higher phonon scattering at these interfaces leads to a lattice thermal conductivity reduction. Due to the combination of all these effects, the ZT of the HH nanocomposites with 1 at.% InSb has reached an enhancement of ~160% ($ZT=0.5$ at 820 K) compared to the HH matrix [82].

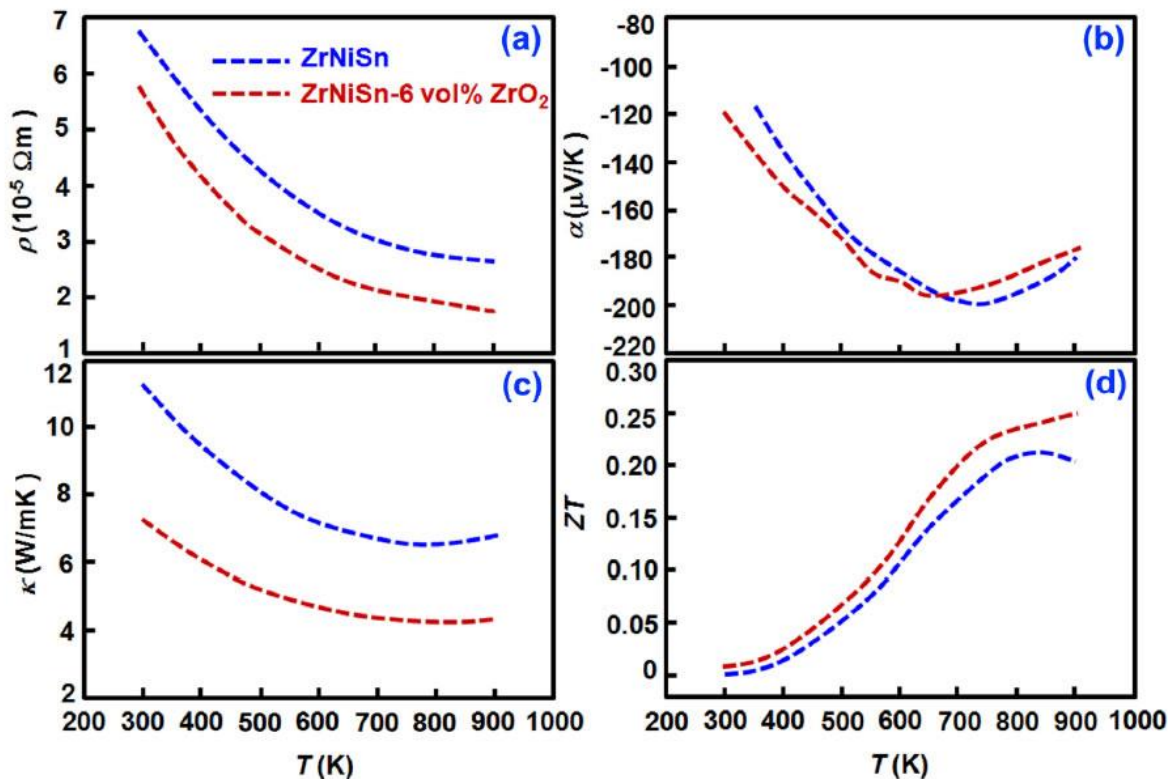


Figure 1.4 : Thermoelectric properties of ZrNiSn-ZrO₂ nanocomposites: (a) electrical resistivity, (b) the Seebeck coefficient, (c) thermal conductivity, and (d) figure of merit [80].

1.2.1.3 Chalcogenides

In general, when there is at least one chalcogen anion and at least one electropositive element in a chemical compound, it is called a chalcogenide. All the elements in the group 16 of the periodic table are defined as chalcogen, however, the term chalcogenide is more generally used for tellurides, selenides, and sulfides, rather than the other elements of this group [87]. Some of the well-known TE chalcogenides such as PbTe, PbSe, or even PbS crystallize in a rock salt crystal system. However, there are other TE chalcogenides or dichalcogenides such as bismuth telluride and molybdenum disulfide with hexagonal crystal structure [88-92].

Embedding nano-inclusions in the chalcogenide TE nanocomposites has been widely studied. For instance, using PbS nano-particles in PbSe matrix, adding PbTe nano-inclusions into PbS, or embedding Sb, Ag₂Te, AgSbTe₂, NaSbTe₂, and SrTe nano-particles in PbTe have been reported [44, 93-97]. In almost all of these studies, the lattice thermal conductivity of the nanocomposites

decreased. Figure 1.5 illustrates the comparison of lattice thermal conductivity in various PbTe based nanocomposites.

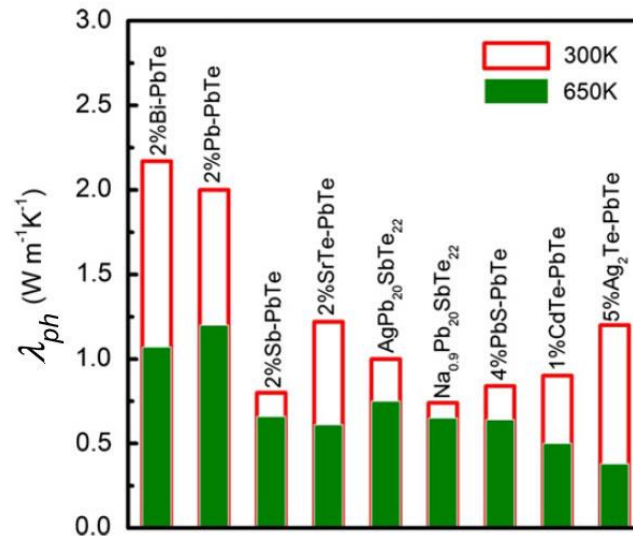


Figure 1.5 : Lattice thermal conductivity in PbTe-based nanocomposites with different type of nano-inclusions [29].

The concept of coherent and incoherent nano-inclusions has received more attention recently. When the nano-inclusions and the matrix have similar lattice parameters, and there is a lattice alignment at the contact of the two phases, the interface is called coherent. In contrast, an incoherent interface involves lattice parameters mismatch between nano-inclusion and the matrix, which leads to a clear boundary between two phases. Although both coherent and incoherent interfaces in nanocomposites could significantly reduce the lattice thermal conductivity, yet the mechanisms of phonon scattering in each one is different from the other to some extent. In fact, coherent interfaces act more like point defects, therefore they do not effectively scatter phonons with long wavelength, while the incoherent interface will filter out the phonons, and the phonons with long wavelength could not pass through the nano-inclusion. In addition, for the incoherent interfaces, the mismatched phonon modes also lead to lattice thermal conductivity reduction [29]. The incoherent interfaces not only have impact on thermal conductivity but also have a negative impact on electrical conductivity. These differences between coherent and incoherent interfaces in nanocomposites could be the main reason to see different effect of nano-inclusions on the lattice thermal conductivity as shown in Figure 1.5 [29]. To obtain coherent interfaces in the TE nanocomposites, the idea of using in-situ approach to synthesize these materials, such as

formation of nano-scale precipitates or other secondary phases via nucleation and growth through material synthesis stages, is used in several reports [72, 96, 98, 99]. Ikeda et al. presented several studies on in-situ processes of PbTe based TE materials. They studied the effect of cooling rate until the material cooled below the eutectic temperature of the alloy on the microstructure and phases of pseudo-binary alloys of PbTe-Sb₂Te₃. As it is shown in Figure 1.6 they obtained finer microstructure by increasing the solidification rate [100].

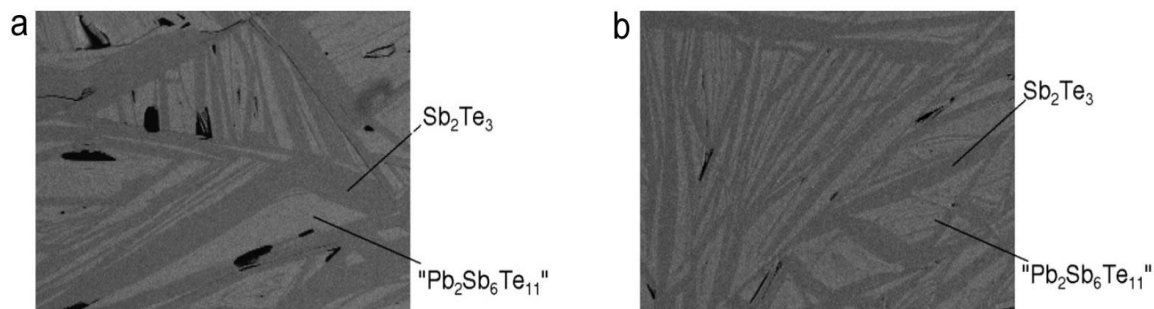


Figure 1.6 : The microstructure of solidified alloys with the composition of Te-36at.%Sb-5at.%Pb (a) cooled in air, (b) quenched in water [100].

They also tried to produce a layered (lamellar) microstructure of Sb₂Te and PbTe by decomposition of metastable Pb₂Sb₆Te₁₁ phase when they showed the possibility of interlamellar spacing control during decomposition process (see Figure 1.7) [98]. The decomposition of the Pb₂Sb₆Te₁₁ solid solution occurs during annealing at a temperature below the eutectoid temperature. The lamellae of the PbTe and Sb₂Te₃ are crystallographically oriented with an average lamellar spacing as small as 180 nm, corresponding to a PbTe layer thickness of 40 nm [98].

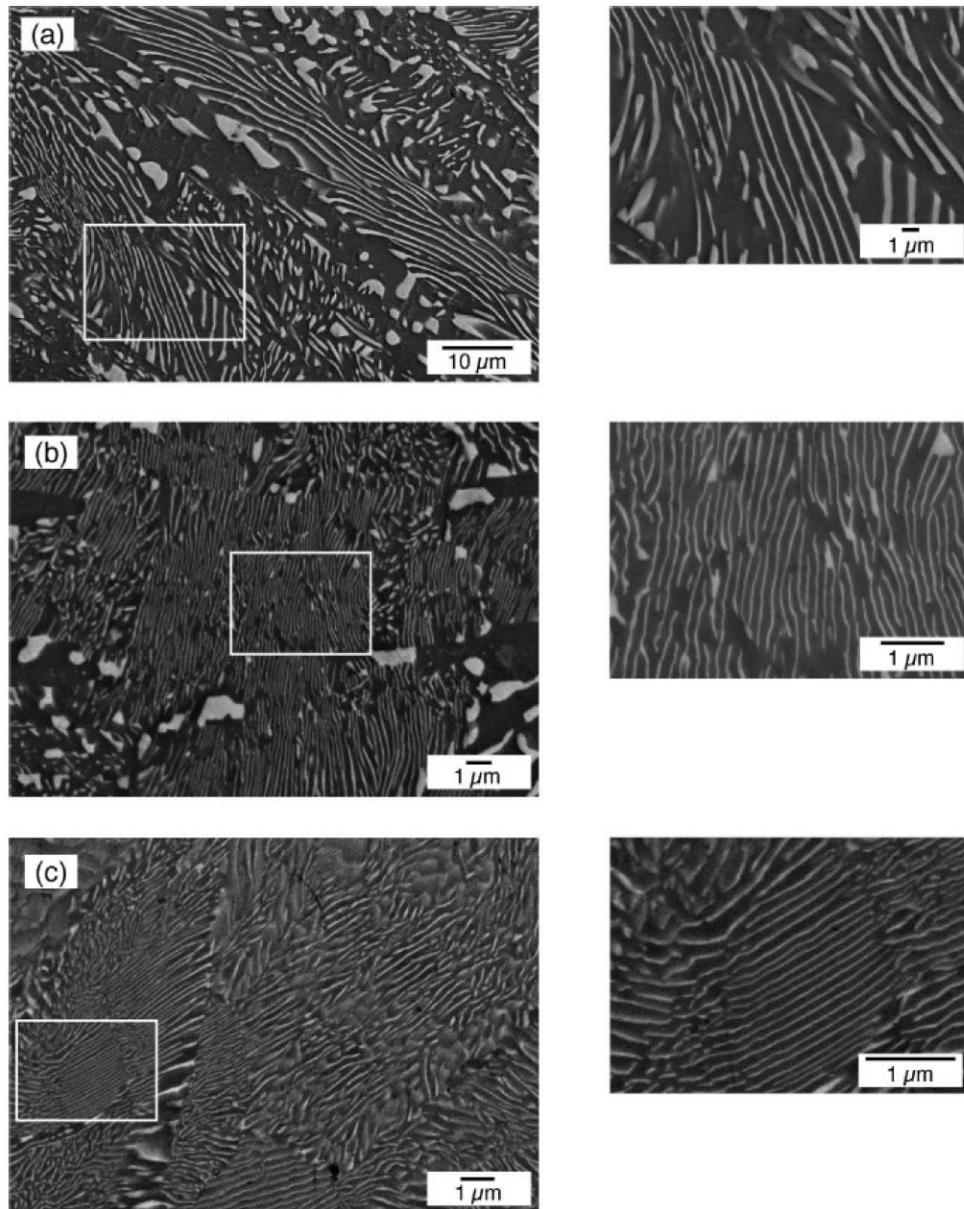


Figure 1.7 : Microstructure of transformed $\text{Pb}_2\text{Sb}_6\text{Te}_{11}$ to PbTe and Sb_2Te_3 lamellae by annealing. The darker regions are Sb_2Te_3 , the lighter regions PbTe . (a) annealed at $500\text{ }^\circ\text{C}$ for 5 days, (b) annealed at $400\text{ }^\circ\text{C}$ for 5 days, (c) annealed at $300\text{ }^\circ\text{C}$ for 5 days [98].

Moreover, this research group studied the formation of Widmanstätten precipitates in the PbTe while Pei et al. studied Ag_2Te precipitates in the $\text{PbTe}\text{-Ag}_2\text{Te}$ system and showed the precipitates formation mechanism in this composite is similar to the Widmanstätten precipitates in $\text{PbTe}\text{-Sb}_2\text{Te}_3$ [99, 101].

Bi_2Te_3 -based materials and similar families of these materials such as Sb_2Te_3 are well-known TE materials for room temperature applications. Obviously, making nanocomposites of bismuth telluride based TE materials attracted lots of attentions by different research groups. The reported bismuth telluride based TE nanocomposites are mostly placed in the category of nanocomposites made by nano-inclusions [102-107]. Similar to the other TE nanocomposites, the main goal of making nanocomposites of bismuth telluride based materials is to reduce the thermal conductivity by introducing more phonon scattering centers with different scales. However, in some reports such as that of Xie et al., reduction in lattice thermal conductivity led to a power factor reduction in *n*-type bismuth telluride nanocomposites due to the increased carrier concentration [104]. The challenge in the bismuth telluride based materials, especially in *n*-type material, is mostly due to the anisotropy of electronic properties. Aligning the randomly oriented grains has been obtained by flowing methods such as press or hot extrusion [108-110]. Besides the phonon scattering observed in the particle dispersed nanocomposites, some reports also showed a carrier filtering effect. Ko et al. claimed a significant increase in Seebeck coefficient of $\text{Pt/Sb}_2\text{Te}_3$ due to the filtering effect of lower energy carriers [106]. A study of the addition of SiC nano-particles to both *n*-type and *p*-type bismuth telluride based alloys by Liu et al. showed that the power factor slightly increased in *p*-type material, while it was reduced in the *n*-type alloys. They investigated the charge carrier concentrations and mobility in these nanocomposites, and reported that by adding 1% SiC the carrier concentration in *p*-type composites increased more than *n*-type ones. Also, they observed greater reduction in carrier mobility of *n*-type nanocomposites comparing to the *p*-type. In fact, electrons scattered more than holes by adding SiC nano-particles, to *n*-type and *p*-type bismuth telluride. This difference revealed that using nano-particles gives the possibility of selective scattering of charge carriers, which is useful to reduce the bipolar effect. This difference was explained by the carrier exchange between the nano-particles and the matrix that is related to the conduction mode of each one. SiC nano-particles are *p*-type semiconductors, so in *n*-type material *p-n* junctions will be formed at the interfaces of nano-particles and the matrix. As it is discussed in this report, some of the carriers will be consumed by the formation of *p-n* junctions, and consequently, the *p*-type matrix showed greater increased in the carrier density when less carrier mobility reduction was observed compared to the *n*-type matrix [107]. Other study on SiC-BiSbTe nanocomposite showed that interfaces between SiC and bismuth telluride

based matrix is coherent, which is expected due to the similarity in the lattice parameters of both compounds (see Figure 1.8) [111].

As we mentioned earlier in this section, formation of lamellae in the near-eutectic compositions of pseudo-binary systems in PbTe, is one the approaches to make nanocomposites with coherent interfaces. Yim et al. reported a similar work for PbTe-Bi₂Te₃ system [112]. Different compositions of Pb-Bi-Te were prepared by melting them at 973 K for 24h, and then the samples were quenched in the water. As it is illustrated in Figure 1.9, the microstructure of these composites contains lamellae of phases such as Bi₂Te₃, PbTe, and PbBi₂Te₄. The lattice thermal conductivity of the composites with smaller lamellae is lower than the others due to higher density of interfaces. However, they still did not achieve by this method to conserve the electrical conductivity as high as the binary alloys of PbTe and Bi₂Te₃.

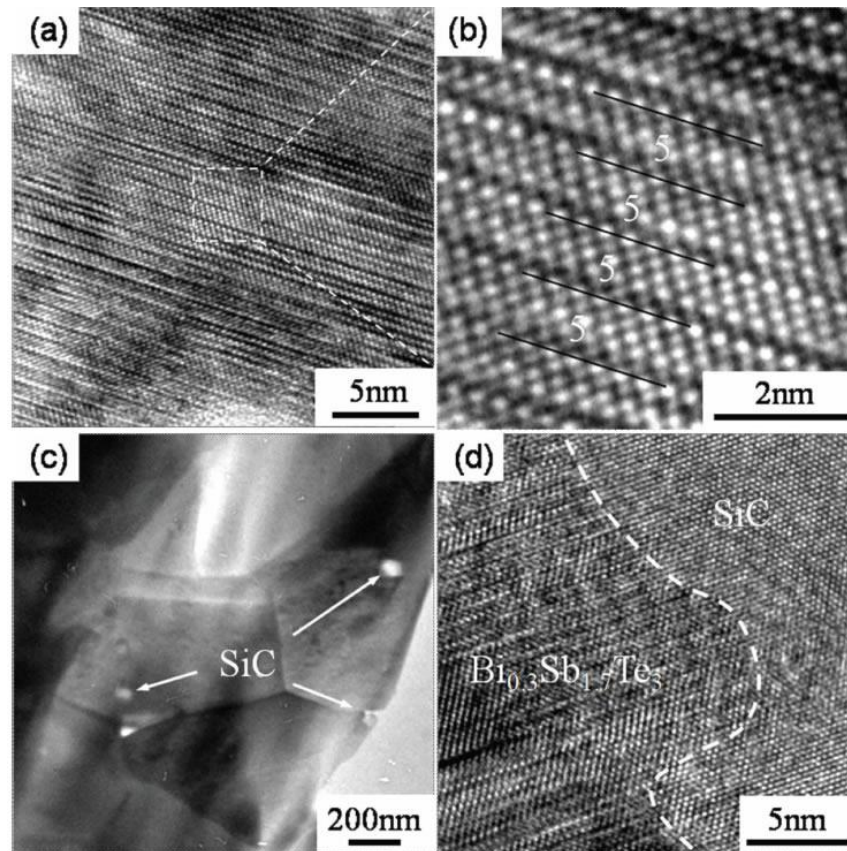


Figure 1.8 : TEM images of (a) Bi_{0.3}Sb_{1.7}Te₃ matrix (b) magnified area of panel a, (c) SiC nanoparticle in the matrix, (d) HRTEM image of the interface between SiC nano-particle and the matrix [111].

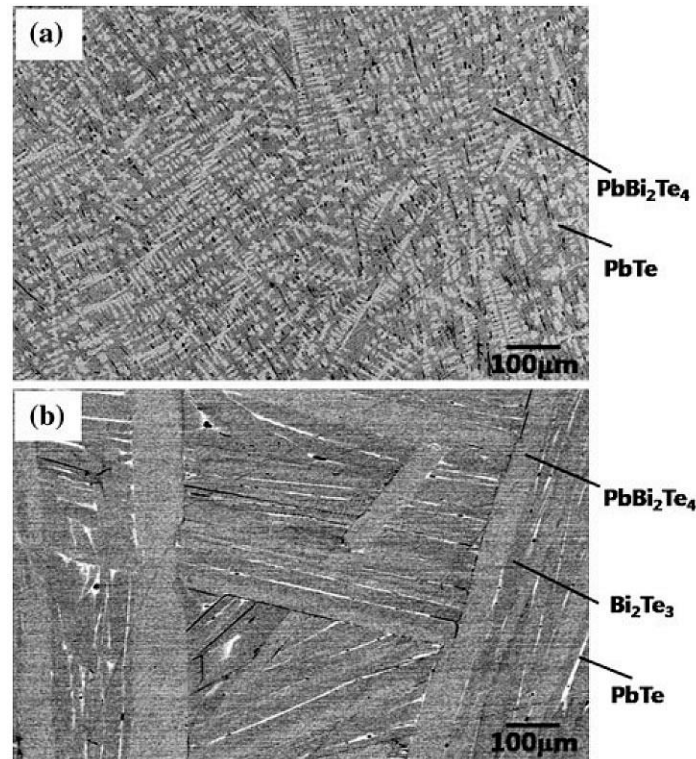


Figure 1.9 : Microstructure of water-quenched Bi_2Te_3 - PbTe alloys with chemical composition of: (a) $\text{Pb}_2\text{Bi}_2\text{Te}_5$ and, (b) $\text{PbBi}_6\text{Te}_{10}$ [112].

1.2.2 Random nanocomposites vs. ordered nanocomposites

In 2011 Liu et al. [29], proposed to categorize the TE nanocomposites in two classes; ordered nanocomposites, and random nanocomposites. The various nanocomposites of each category are schematically shown in Figure 1.10.

TE materials are mostly heavily doped semiconductors. Consequently, by increasing the doping level, the carrier mobility decreases due to ionized impurity-carrier scattering. To minimize this scattering a strategy of modulation doping is proposed. In a composite material with an un-doped matrix phase, the carrier mobility in the matrix is high. If one can manage to introduce a heavily doped secondary phase, which can provide the necessary carrier density without strongly affecting the mobility in the composite, the modulation doping is successfully achieved.

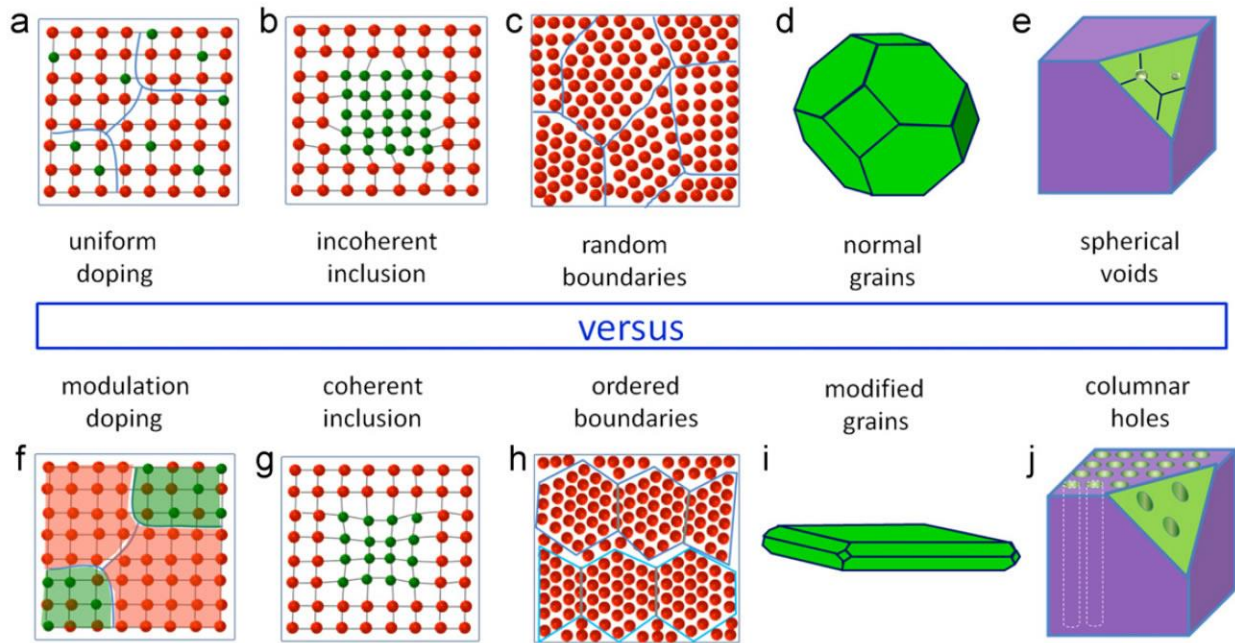


Figure 1.10 : Schematic of random nanocomposites (a-e), and ordered nanocomposites (f-j) [29].

In the previous section, several examples of nanocomposites with coherent and incoherent interfaces were given. These studies [72, 96, 98, 99] mostly reported less deteriorating effect of coherent interfaces on the carrier mobility than the incoherent ones. Using these investigations, Liu et al. attributed the nanocomposites with coherent inclusions to the ordered nanocomposites, and the nanocomposites with incoherent inclusions to the random nanocomposites [29].

Another criterion in this classification is related to the type of the grain boundary. The effect of grain boundaries and type of grain boundaries on the transport properties of the TE materials has not been completely investigated. Although, it has been confirmed that some of the grain boundaries such as twin boundaries, have less impact on the transport properties of charge carriers yet they scatter the phonons. However, there are studies that showed ordered grain boundaries assist the electrons' transport in the *n*-type Bi₂Te₃-based polycrystals, which led to an increase of the power factor up to 40% in the specific direction of the sample [108, 109].

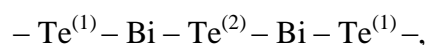
Decoupling of the charge carriers and phonons transport is one of the challenges in TE research. However, transport behavior of nanowires and thin films along the in-line direction showed that in these types of materials (not bulk materials), there is a significant phonon scattering while less influence on the charge carriers due to the boundary confining effect [35, 36, 113]. On the other hand, in the TE materials with cubic crystal structure, the grains have comparable sizes in all

directions with isotropic thermal and electrical properties. The grain boundary could have similar phonon confining effect along one direction, thus, modification of the grain shape into wire-like or plate-like is suggested to decouple the charge carrier transport and phonons transport in bulk materials [29].

According to the theoretical and experimental studies on the size and order of voids in TE materials, thermal conductivity will be reduced in the materials with columnar voids when impact on the carrier mobility is small [114, 115]. Although it is really challenging to make such tiny voids in current TE materials, this is an inspiring starting point for this category of TE nanocomposites.

1.3 Bismuth telluride- based alloys

Bismuth telluride, Bi_2Te_3 , was reported for the first time as an effective TE material in 1954 [116]. It has a rhombohedral unit cell, although its crystal structure can be also expressed in terms of a hexagonal unit cell [91]. The single crystals of bismuth telluride are anisotropic. It is such that Bi and Te atoms are grouped and arranged in parallel layers which are stacked within a unit cell in the [111] direction following the sequence:



This sequence is continually repeated. There are two different bonding types between the Bi and Te atoms. Atoms of Bi are strongly bound to the Te atoms by covalent-ionic bonds on both types of site, but the layers of $\text{Te}^{(1)}$ atoms are weakly bound by van der Waals forces to neighboring $\text{Te}^{(1)}$ layers [1, 91, 117]. Each Bi atom is bound on one side to three $\text{Te}^{(2)}$ atoms with a 3.22\AA bond length and on the other side to three $\text{Te}^{(1)}$ atoms with a 3.12\AA bond length [117]. Figure 1.11 illustrates the schematic of crystal structure of bismuth telluride in hexagonal representation [118].

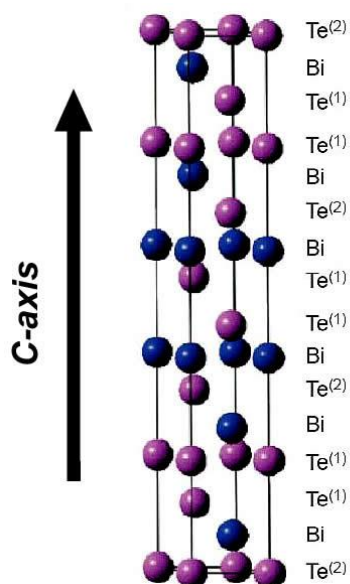


Figure 1.11 : Hexagonal representation of bismuth telluride crystal structure. Bi atoms in blue spheres and Te atoms in purple [118].

The crystals of bismuth telluride are easily cleaved along the direction of the layers, perpendicular to trigonal or c-direction [1]. There are two a-axes normal to the c-axis. Not only the mechanical properties are different in the plane of a-axes and c-direction, but also the electrical and thermal properties are different. For instance, the thermal and electrical conductivities are lower perpendicular to cleavage planes than parallel to them.

The lattice component of the thermal conductivity in the c-direction of bismuth telluride crystals is less than in the plane of the a-axes by a factor of 2.1. One of the first series of measurements of the thermal conductivity of bismuth telluride samples showed a relatively low value of $2.5 \text{ Wm}^{-1}\text{K}^{-1}$ in the direction parallel to cleavage planes, and in the direction perpendicular to cleavage planes it became much lower, down to $0.7 \text{ Wm}^{-1}\text{K}^{-1}$. It has reported that *n*-type Bi₂Te₃ has a lower thermal conductivity compared to *p*-type [119, 120].

However, the electrical conductivity is even more intensely anisotropic and the ratio of electrical conductivity in the a-direction to electrical conductivity in c-direction is different for *n*-type and *p*-type materials. Particularly, in *n*-type material this ratio varies with the doping level as it is illustrated in Figure 1.12.

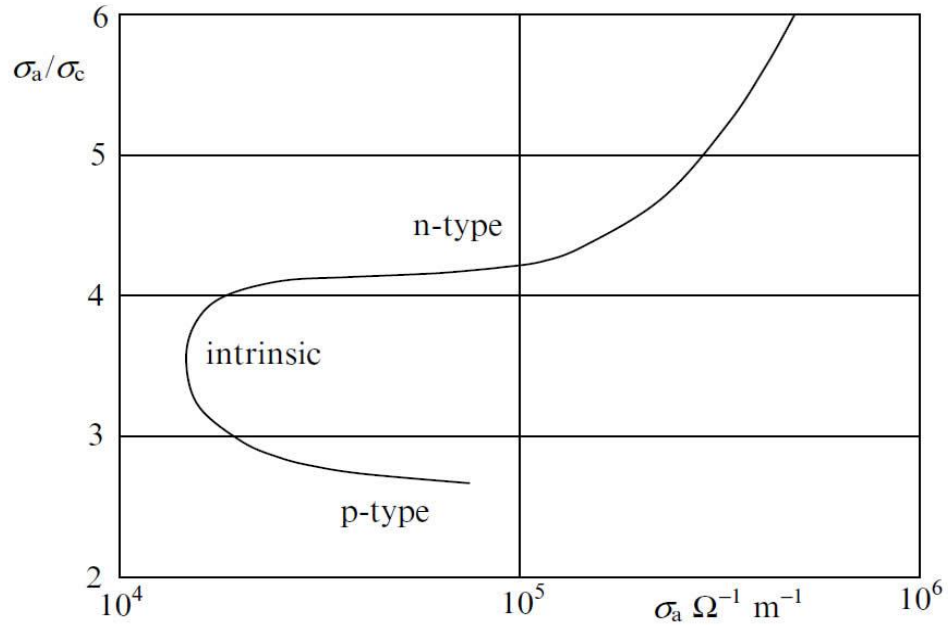


Figure 1.12 : Plot of the ratio of electrical conductivities of single crystal bismuth telluride at 300 K in the a-direction (σ_a) and c-direction (σ_c) vs. σ_a [1].

The energy gap of bismuth telluride was found to be 0.145 eV at room temperature [121, 122]. It has been reported that bismuth telluride, in the strict 2:3 stoichiometry form, is intrinsically *p*-type material. It has also been found that the presence of Te in excess of 62% leads to a shift from *p*-type to *n*-type as it is shown in Figure 1.13 [123-126].

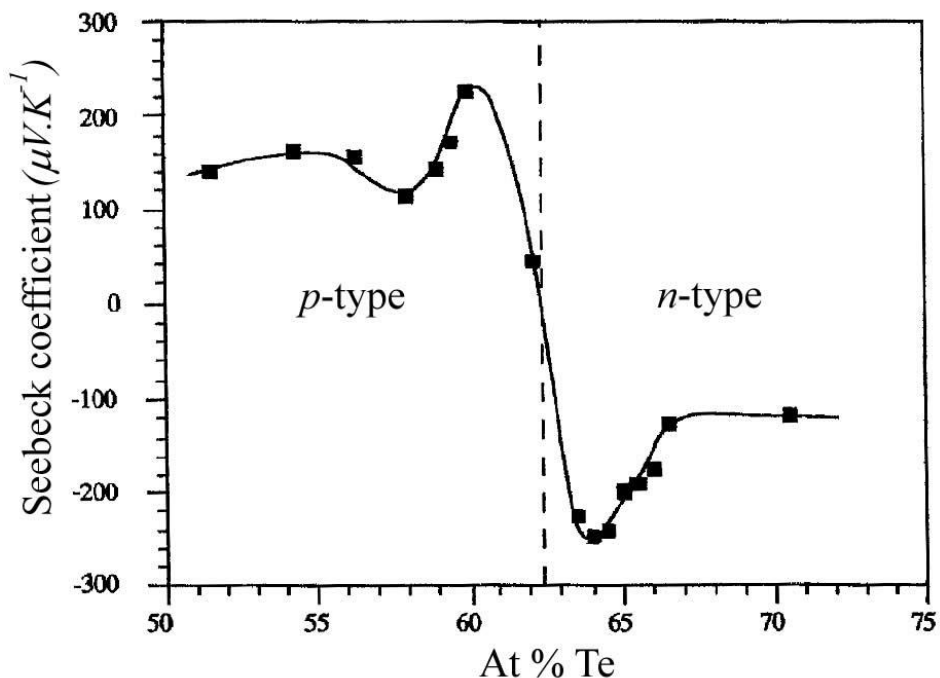


Figure 1.13: Seebeck coefficient of bismuth telluride as a function of Te at.%. Dash line indicate at around 62 at.% the conduction mode of bismuth telluride changes [123].

After the ideas of Ioffe et al. [127] on semiconductor solid solutions, alloying of Bi_2Te_3 with isomorphous compounds such as Bi_2Se_3 and Sb_2Te_3 was studied. Studies have shown that a solid solution of Bi_2Te_3 with Sb_2Te_3 is expected to be the best p -type material while a solid solution of Bi_2Te_3 with Bi_2Se_3 is likely to be the best n -type material. As has already been mentioned, Bi_2Te_3 is a p -type intrinsic semiconductor and its main cause is the non-stoichiometric compound obtained from the melt. As this compound is alloyed with Sb_2Te_3 , it would be much more difficult to make these solid solutions n -type, since the non-stoichiometry becomes more pronounced. In another words, making such a solid solution makes a strong p -type material that would be hard to be n -type doped while making a solid solution of Bi_2Te_3 and Bi_2Se_3 leads to a less strong p -type material, which requires less doping to turn into a n -type material.

Several studies have shown that solid solutions have a lower lattice thermal conductivity, λ_{ph} , compared to pure Bi_2Te_3 . In Figure 1.14 and Figure 1.15, the lattice thermal conductivities of $(\text{Bi-Sb})_2\text{Te}_3$ alloys by changing the molar percentage of Sb_2Te_3 in the systems are respectively illustrated, based on data obtained from the literature [1, 24, 122, 128].

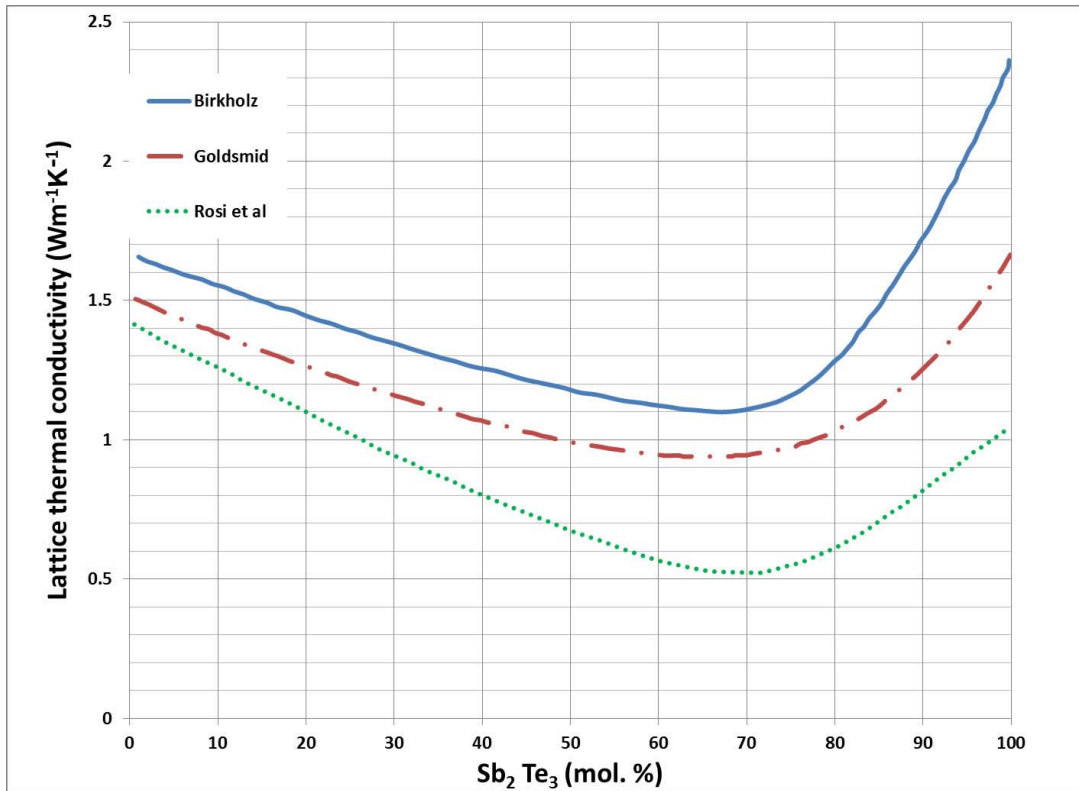


Figure 1.14: Plot of lattice thermal conductivity against molar percentage of Sb_2Te_3 in solid solutions of $(\text{Bi-Sb})_2\text{Te}_3$ (based on data of Birkholz, Goldsmid, and Rosi et al. [24]).

Figure 1.16 shows TE figures of merit as a function of conductivity of compounds and alloys of bismuth telluride based on a study of Goldsmid and Delves [129]. Both quantities vary with the charge carrier concentration; however, for both n -type and p -type material in pure compound as well as solid solutions, the optimum electrical conductivity has nearly the same value.

Single crystals and alloys of Bi_2Te_3 are too brittle. Single crystals particularly are so fragile that they cannot be practically applicable. Using nearly aligned polycrystalline material of small grain size leads to high figure of merit with adequate mechanical strength. The suggested approach to produce such alloys of bismuth telluride is cold or hot pressing followed by sintering. However, materials produced by hot extrusion process showed stronger alignment of crystals which is particularly beneficial for n -type bismuth telluride. In general, the best reported technique to produce textured bismuth telluride alloys is hot extrusion which has shown the potential to produce both n -type and p -type textured alloys with different compositions.

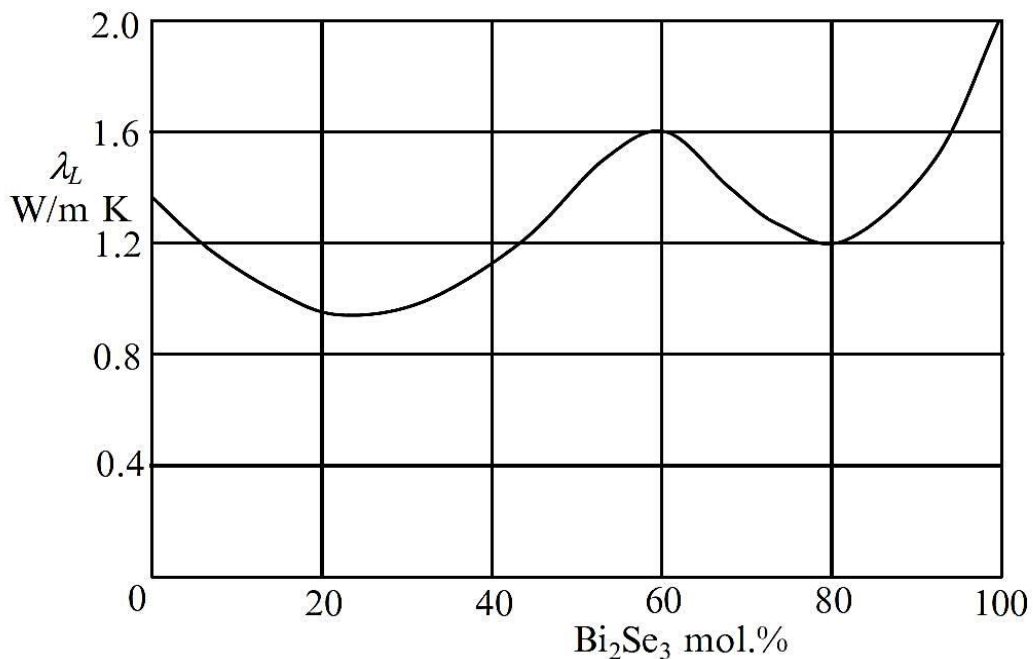


Figure 1.15: Plot of lattice thermal conductivity at 300 K against molar percentage of Bi_2Se_3 in solid solutions of $(\text{Bi-Sb})_2\text{Te}_3$ [1].

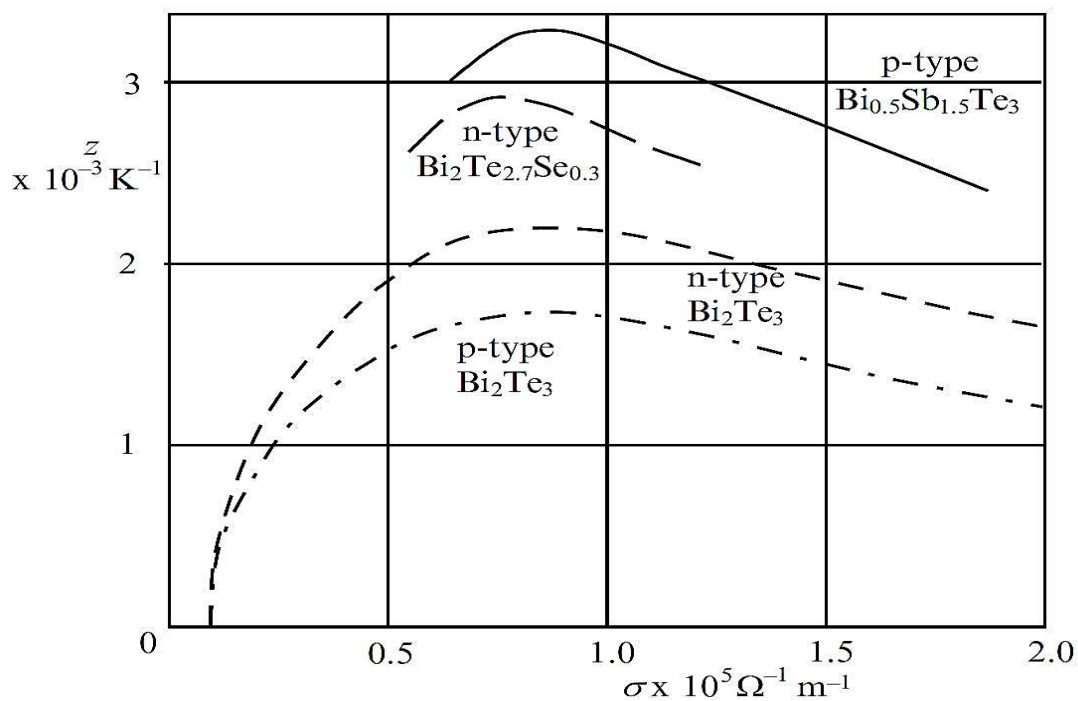


Figure 1.16: The thermoelectric figure of merit plotted against electrical conductivity for *n*-type and *p*-type solid solutions and pure compound of bismuth telluride [1].

Also, the distinct advantage of varying temperature and pressure together during the sintering, is grain growth restriction which is necessary to conserve the nanostructure of the material since an applied stress adds a new component to the driving force for densification. Hydrostatic stress also induces a stress-assisted diffusion mechanism. These mechanisms enhance the densification rate [110, 130, 131].

1.4 The molybdenum disulfide system

Molybdenum disulfide (MoS_2) is a transition-metal dichalcogenide material with layered structure. During the past decade, MoS_2 has attracted great interest due to its typical optical, catalytic, electronic, and thermoelectric properties, as well as its reputation for dry lubrication [92, 132-138]. As illustrated in Figure 1.17, its structure can be thought of as a series of sheets. Each sheet has a molybdenum atomic layer placed between two sulfur atomic layers. Considering these sheets as basal planes, they set up a hexagonal crystalline structure such that each basal plane has a molybdenum atom surrounded by six sulfur atoms. The weak Van der Waals forces make the sulfur-sulfur bonds between basal planes which are 3.08 Å long. However, sulfur and molybdenum atoms are connected by strong covalent bonds. There is an electrostatic repulsion between the layers due to the configuration in the structure, which makes a net positive charge on the surface of the layers. Due to the weak interlayer Van der Waals interactions, shear deformation between the two sulfur layers is facilitated, which makes MoS_2 one of the most popular solid lubricants [92, 139-141].

Bulk MoS_2 is known to be an indirect gap semiconductor. The reported experimental value of its indirect band gap is 1.29 eV [133, 142]. Some studies reported a semiconducting behavior for nano-particles of MoS_2 [143, 144]. However, several reports have shown that the electronic structure of MoS_2 changes by decreasing the particle size (number of layers) [136, 142, 145-147]. While the quantum confinement effect has been predicted for 3D semiconductor nano-particles of MoS_2 , no apparent quantum confinement effect is reported for MoS_2 nano-platelets (2D) even as small as 2nm [136].

On the other hand, 3D nano-particles of MoS_2 showed semiconductor behavior with direct band gap. Li and Galli [136], as well as Mak et al. [147] reported their band gap calculations for

different number of infinite-wide S-Mo-S sheets, and they showed band gap decreases monotonically from ~ 1.8 to 0.86 eV as number of sheets increases from 1 to infinity. Though, Kumar and Ahluwalia calculations showed that MoS_2 nano-platelets are indirect band gap semiconductors up to bilayer limit, but in the monolayer limit the band gap changes to direct band gap (see Figure 1.18) [136, 146, 147].

Also, interesting studies on the edge configurations and edge geometries of MoS_2 nano-platelets and nano-ribbons have been reported. These nano-platelets are portions of bulk layers with different and various edge geometries. These edge geometries are predicted to lead to different electronic structure and thermal conductivity of MoS_2 monolayer or even a few-layer particle [136, 148]. For example, Liu et al. investigated the thermal conductivity of MoS_2 monolayer and nano-ribbons using molecular dynamic simulations. As illustrated in Figure 1.19, the two types of MoS_2 nano-ribbons that they studied are the armchair nano-ribbons and zigzag nano-ribbons. They showed that thermal conductivity of MoS_2 monolayers of different width (3-18 nm) with fixed 11 nm length in nano-ribbons with armchair edge configuration is less than that of the zigzag edge configuration. However, for the MoS_2 nano-ribbons 3nm wide or broader, the thermal conductivity is almost independent on width of the nano-ribbons [148].

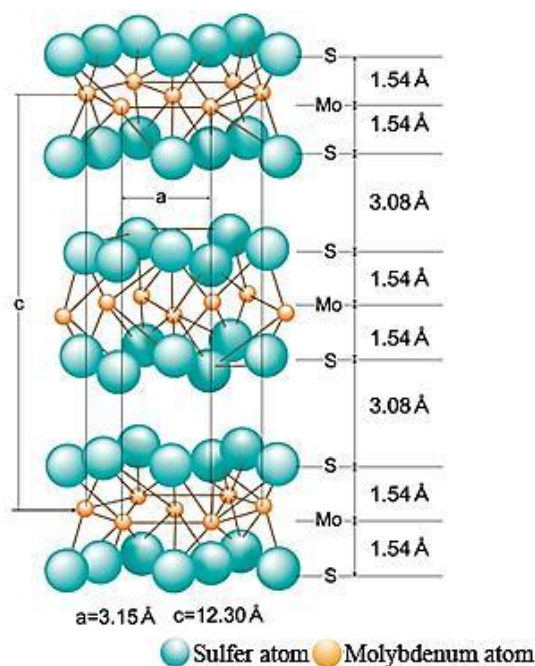


Figure 1.17: Crystal structure of molybdenum disulfide and distances between its atomic layers [140].

Very recently, few studies on thermoelectric performance of MoS₂ monolayers have been reported [92, 149]. Previous experimental results have shown that the thermal conductivity of MoS₂ film is in the order of 0.1-1 W/mK [92, 150]. Since semiconductors with low thermal conductivity are mostly preferable to obtain TE materials with high performance, it is important to investigate other TE properties of monolayer MoS₂. Huang et al. calculations of ZT for n -type and p -type MoS₂ monolayer using ballistic transport approach based on full electronic band structure showed that a p -type MoS₂ monolayer has the highest ZT value at room temperature [92]. Buscema et al. showed that the photocurrent generation in MoS₂ monolayer is dominated by the photo-thermoelectric effect. They reported a tunable Seebeck coefficient by an external electric field, between -4×10^2 and $-1 \times 10^5 \mu\text{VK}^{-1}$ for MoS₂ monolayer [149]. These studies and results attract great interests for further studies on TE properties of MoS₂ in the nano-scale.

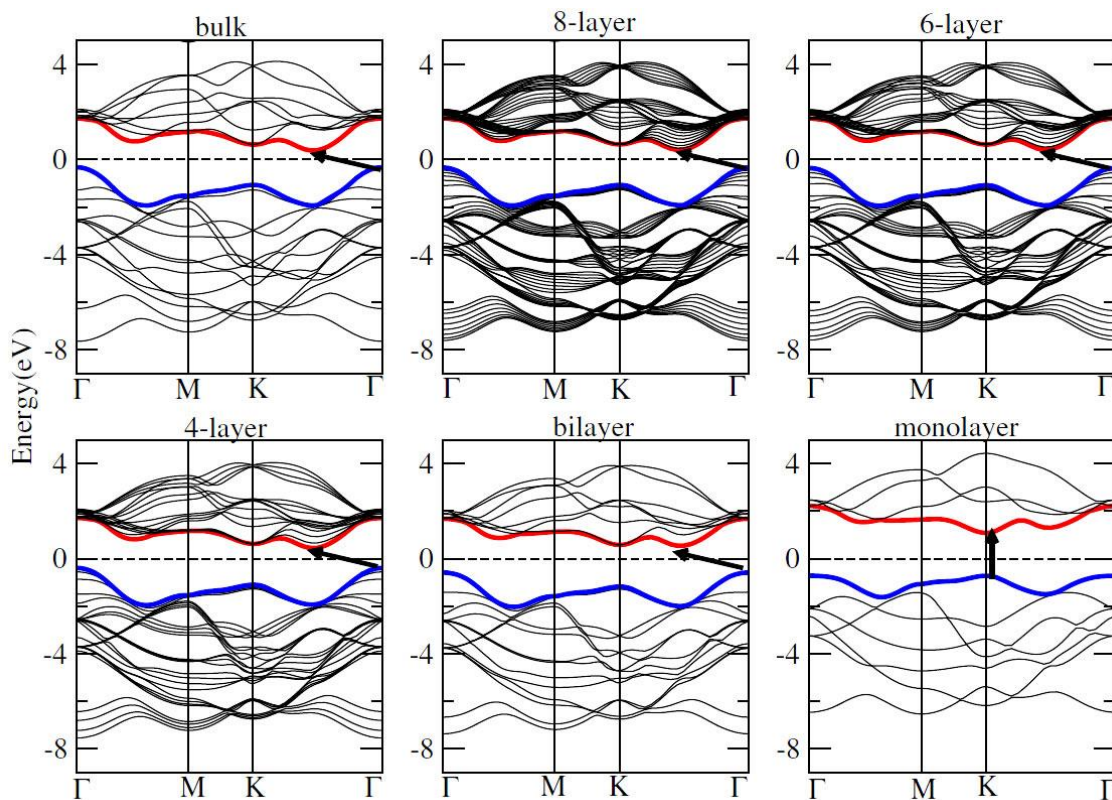


Figure 1.18 : Size-dependent electronic band structure of MoS₂. The bottom of the conduction band (in red) and top of the valance band (in blue) are highlighted. The Fermi level is set at 0 eV and the arrow shows the smallest value of the indirect or direct band gap[146].

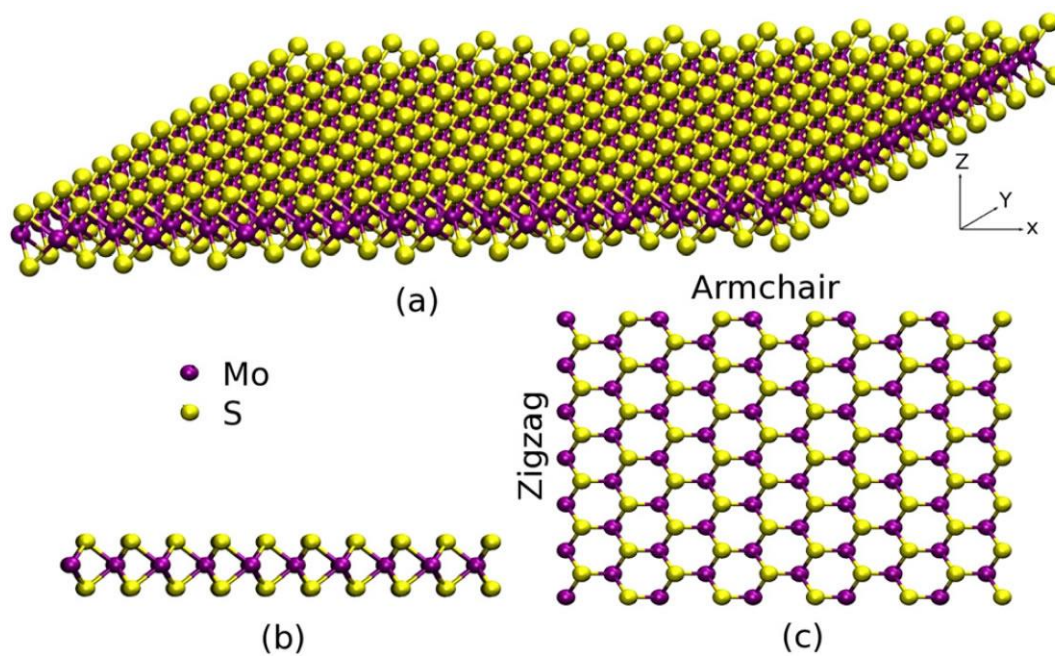


Figure 1.19 : Schematic of different edge configurations in (a) MoS₂ monolayer, (b) side view of monolayer, (c) top view of MoS₂ monolayer. The horizontal orientation shows the armchair configuration and the vertical orientation shows the zigzag configuration [148].

Chapter 2 EXPERIMENTAL METHODS

2.1 Starting Materials

To synthesize bismuth telluride based alloys high-purity (99.999%) pellets of Bi, Sb, Te, and Se were used as starting materials. The size and shape of these elemental pellets are demonstrated in Figure 2.1. To obtain *p*-type alloys we doped the alloy by Sb, and to obtain *n*-type alloys we used SbI_3 , which is a stable solid at room temperature as a dopant.



Figure 2.1 : Elemental pellets of starting materials used to synthesize bismuth telluride based alloys.

MoS_2 nano-particles (99.99% purity) with a nominal particle size smaller than 90 nm (supplied by MKnano, Division. of M K Impex Corp.) were used as nano-inclusions in one series of nanocomposites. As illustrated in Figure 2.2, nano-particles of molybdenum disulfide are mostly agglomerated and form particles as large as a couple of microns. It is clear from the image that the nano-particles are mostly flakes with submicron diagonal size, and thickness less than 100 nm.

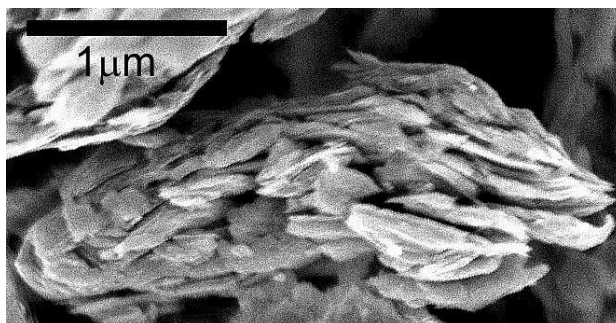


Figure 2.2 : Morphology of MoS₂ nano-particles as provided by supplier.

2.2 Synthesis

In this study, the process of mechanical alloying is used to achieve alloying of elemental materials. In this alloying approach, mechanical energy is used rather than thermal energy to bring about the chemical reactions. To obtain the desired alloy, the elemental materials are placed in a container according to the desired stoichiometry along with stainless steel balls of 2mm diameter as milling medium. Several techniques are used to agitate the milling medium inside the container. In our study, we used an attritor with a fixed container where milling media inside is agitated by a mixing bar (agitator) (see Figure 2.3). Milling media have collisions with the container or/and other milling media. At each collision a small portion of elemental materials is trapped at the point of impact, lead to occurrences of cold welding, fracturing, and re-welding of particles. By repetition of these processes an alloy of the primary elements forms. Obviously, impacts between media, container, and materials result in heat generation. To cool down the total system, we used the water cooled attritor container. The optimum processing variables in milling such as milling time, milling media, or ball-to-powder weight ratio were obtained by studies of former students of the Polytechnique thermoelectric research group [151].

One of the most effective approaches to produce full density bulk samples of powder materials is powder hot extrusion. The crystallographic texture obtains as a consequence of the large deformation along the extrusion direction. Also, the distinct advantages of varying temperature and pressure together during the sintering, is grain growth restriction since an applied stress adds a new component to the driving force for densification.

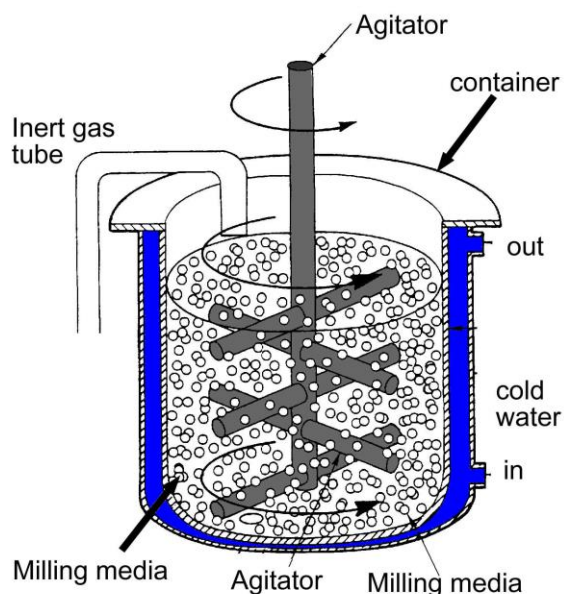


Figure 2.3 : Schematic of attrition system used for mechanical alloying.

This growth restriction is necessary to conserve the nanostructure of the material. The hydrostatic stress also induces a stress-assisted diffusion mechanism. These mechanisms enhance the densification rate [110, 131]. The contamination of powders during mechanical alloying is unavoidable and it is mainly due to the erosion and wear of parts and medium of the attritor (balls, agitator, and tank). These parts are made of stainless steel, which consists mainly of Fe, Cr, and Ni atoms. Table 2.1 presents the average amount of each of these elements in the mechanically alloyed powders after 14 hours of milling. For this level of impurities, no detrimental effect was observed on the TE properties.

In the current Ph.D. work, hot extrusion was implemented for densification and consolidation of the composite powders. Once more, the optimum process parameters such as time, pressure, and temperature were obtained by studies of former student of the Polytechnique thermoelectric research group that can be found in Ref. [152].

Table 2.1 : Powder contamination during mechanical alloying.

Contaminant	Fe	Cr	Ni
Amount in the powder (ppm)	28.0	1.90	0.55

More detailed specifications of different synthesis procedures of produced composites are given in Chapter 3 and 4.

2.3 Characterization techniques and sample preparations

2.3.1 Microstructure analyses

The microstructure of samples has been analyzed using a Field Emission Gun- Scanning electron microscope (FEG-SEM, JEOL JSM-7600 TFE). To reveal the microstructure, samples were cut, mechanically ground and polished, and electrolytically etched. The etchant solution (electrolyte) contains 570 ml distilled water, 56 g sodium hydroxide, and 48 g tartaric acid. The cathode is made of stainless steel. The optimum surface current density was experimentally found to be 1.2 A/cm², when the most favorable etching times of 180 s and 60 s were established for *p*- and *n*-type materials, respectively. Also, morphology and microstructure of fracture surfaces of the samples were analyzed by FEG-SEM.

2.3.2 Atomic structure analyses

A JEOL JEM-2100F high-resolution transmission electron microscope (HRTEM) was used to analyze the grain size, distribution, and shape of nano-inclusions as well as nanostructure of the nanocomposites. All samples for HRTEM observation were in powder form. Powdered samples of extruded nanocomposites were obtained as a byproduct of sawing them with a diamond blade saw. Powders were dispersed in the using an ultrasonic bath, and then placed on a Cu grid with square mesh.

2.3.3 Phases, elemental, and crystallite size analyses

X-ray powder diffraction (XRD) is a well-known analytical technique principally used for phase identification of crystalline materials. This technique can also provide information about unit cell dimensions.

In this work, the phase compositions of mechanically alloyed powders, as well as hot extruded bulk of all composites and alloys were examined by a Philips X'Pert diffractometer using Cu $K\alpha$ radiation (λ (wavelength)= 0.15418 nm). The average crystallite size of all samples is estimated by using Scherrer's equation [153]:

$$D = \frac{0.9\lambda}{B \cos\theta} \quad (2.1)$$

where D is the average crystallite size, λ is the X-ray wavelength, B is the full width at half maximum of the reflection peaks, and θ is the diffraction angle. For XRD analysis, samples were cut from the produced rods in disk shapes with 2.54 cm diameter and around 2 cm thickness with a polished surface where the surface perpendicular to the extrusion axis exposed to the X-ray beams (see Figure 2.4).

As presented in equation (2.1), crystallite size is inversely proportional to the peak width. However, there are other sources of peak broadening. The main other considerable sources of peak broadening are instrumental broadening (imperfection in diffractometer) and broadening due to the micro-strain in the crystals (when macro-strain in the materials leads to peak position shift). Consequently, the corrected value of B can be obtained by;

$$B_{corrected}^2 = B_{sample}^2 - B_{instrument}^2 \quad (2.2)$$

The common way to measure the instrumental broadening is to use a perfect sample, i. e. single crystal of large grains (in practice a near-perfect sample) whose its broadening contribution to the total broadening is negligible compared to that of instrumental broadening. Therefore, the measured broadening can be considered as instrumental broadening. In this work we used near-perfect crystal of BaF₂ to obtain broadening due to instrument. In addition, the sample contribution to the peak broadening arises from several factors including crystallite size. The other factor which has a significant contribution to the peak broadening caused by sample is micro-strain in the crystal lattice. Yet, to obtain the true crystallite size values by eq. (2.1) we should deduct the contribution of micro-strain in sample broadening. The common way is to make a standard sample of the same material when the micro-strain in the standard sample is relieved [154].

Unfortunately, in case of bismuth telluride based samples, making such standard sample is so challenging. In fact, annealing the sample to obtain larger grains and heal the crystal defects at low temperatures could not help to make a standard sample. On the other hand, annealing at temperatures, above 300°C, may lead to the composition change in the sample, since Te is volatile.

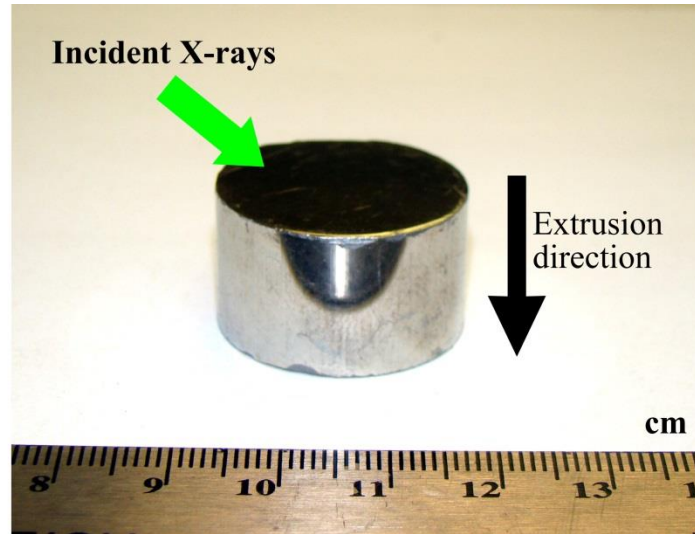


Figure 2.4 : An example of samples prepared for XRD analyses. The upper surface is ground with SiC grinding paper (1200 grit), then polished using slurry of Alumina (particles < 0.05 microns).

The HRTEM we used is equipped with an energy dispersive X-ray spectrometry (EDS) detector. This detector allows the acquisition of qualitative elemental information in a sample. We used EDS to indicate the presence of nano-inclusions in the nanocomposite samples.

2.3.4 Thermoelectric properties

TE properties can be obtained using a measurement system (ZT-scanner 2.2, (TEMTE Inc., Canada)) based on the Harman method [155]. Using this system we could obtain the values of TE properties in the temperature range from 290 to 480 K. Prepared samples are cuboids with dimension 5.2×5.2×5.6 mm (Figure 2.5), cut by dicing saw machine, then Ni plated to make contacts on two opposite polished faces.

In fact, the total voltage drop (V_{total}) across the TE sample is composed of two components; the Seebeck voltage (V_s), and the resistive voltage drop (V_ρ). The V_ρ falls immediately (in few microseconds) to zero once the current is switched off. The remaining voltage, which is V_s , decays gradually as the sample returns to thermal equilibrium (see Figure 2.6). Finally, Z value will be directly determined as the ratio of the V_s and V_ρ [155]:

$$Z = \frac{\alpha^2}{k\rho} = \frac{V_s}{V_\rho T} \quad (2.3)$$

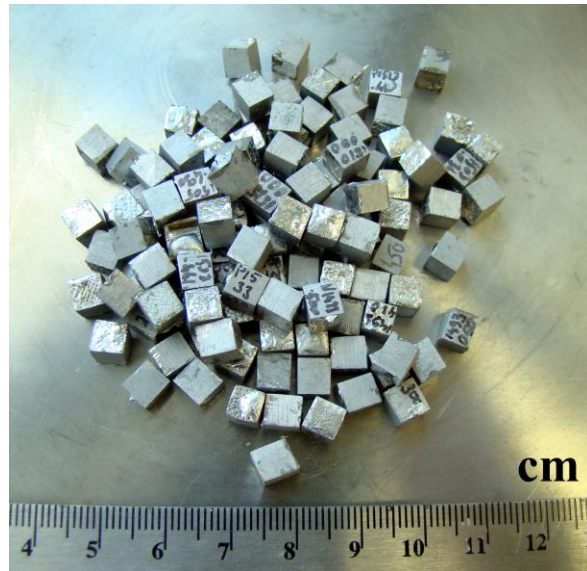


Figure 2.5: Samples prepared for TE properties measurement.

In this method, the thermal conductivity can be determined from measurement of the temperature gradient and geometry of the specimen when an identified direct current is passed through the sample. Also, the electrical resistivity will be measured, and Seebeck coefficient will be calculated by measuring the existed potential (Seebeck voltage) due to a temperature gradient in the sample.

Since the Z values are directly determined by measuring the potential, the only measurement error is coming from measurement instrument and contacts. So the measurement error for Z values is around 2%. We should add, since the charge carrier concentration of two bulk samples, even from the same produced rods, are not exactly the same which leads to slightly different TE properties, the repetition of measurements of several samples to obtain the error bars on the graphs is not applicable. In addition, our experience on repetition of measurement on the same sample showed no significant changes of the values to be reported. However, the instrument error for measured parameters except Z is around 5%.

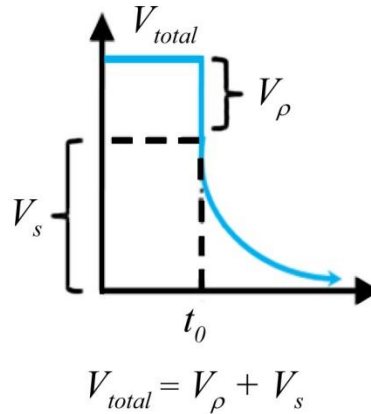


Figure 2.6: Schematic of voltage vs. time graph for a TE material once the current is switched off.

2.3.5 Transport properties

When a conductor carrying a current in a stationary state is subjected to a magnetic field perpendicular to the electric field producing the current, a transverse field is established, which is perpendicular to both applied fields. This effect is known as Hall effect [156], whose magnitude can be measured by a voltmeter to determine the potential difference produced by the transverse field. Utilizing the Hall effect measurement system, we can obtain the charge carrier type, density, and carriers' mobility in the semiconductors.

In this work, we used a system to measure Hall data over a temperature range from 15 to 360 K using the Van der Pauw approach [157]. The samples with thickness around 0.4 mm and (square) area cross section around $5 \times 5 \text{ mm}^2$ were prepared by dicing saw and mechanical polishing. During the measurement a magnetic field of 4 kG was used, and currents between 8 to 9 mA applied to the samples. The corner edges of each sample were soldered to four copper wires on sample holder using In as solder. Figure 2.7 shows example of samples cut and wires soldered for Hall effect measurements.

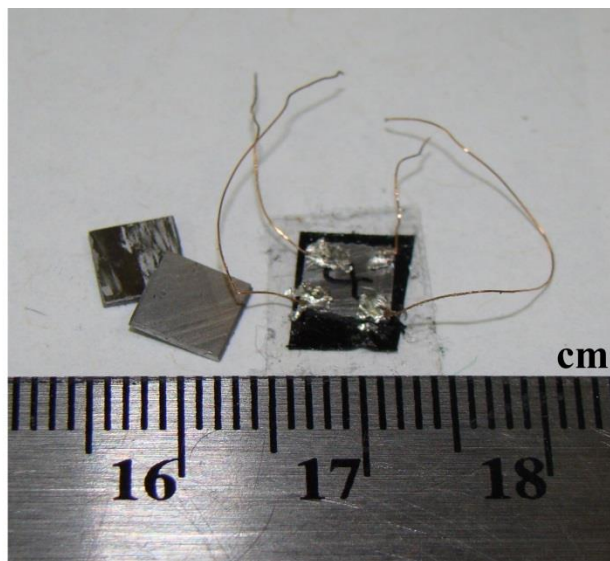


Figure 2.7: Samples prepared for Hall Effect measurements.

2.3.6 Mechanical spectroscopy

Using the impulse excitation technique (IET), which is the mechanical spectroscopic analysis of impulse excited resonant vibrations, one can evaluate some intrinsic parameters of materials such as defects in the material, and Young's modulus. In this technique, vibration will be induced to a freely suspended bar shaped sample by an impulse excitation. A given light impact to the sample makes it vibrate at one or more of its resonant frequencies. Using IET we can determine resonant frequency, and internal friction, i. e. the dissipation of vibration energy, also known as damping, or mechanical loss. Observation of alterations in elastic properties, which are determined by changes of the microstructure, is possible by measuring resonant frequencies as a function of time or temperature [158-161].

During this work, a home built mechanical spectroscopy (MS) set-up was used. The rod shape samples as extruded were cut in 12 cm length, installed in a sample holder to establish the suspension condition, and then placed in a furnace. The impulse excitation is caused by the impact of a stainless ball with 2 mm diameter (see Figure 2.8). Resonant frequencies of longitudinal oscillations of each sample were acquired in a temperature range from room temperature to 573 K. The collected data were treated and Young's modulus, internal friction, and activation energy of internal friction were calculated. More detailed explanations of the MS set-up and its data treatment is available in Ref. [162].

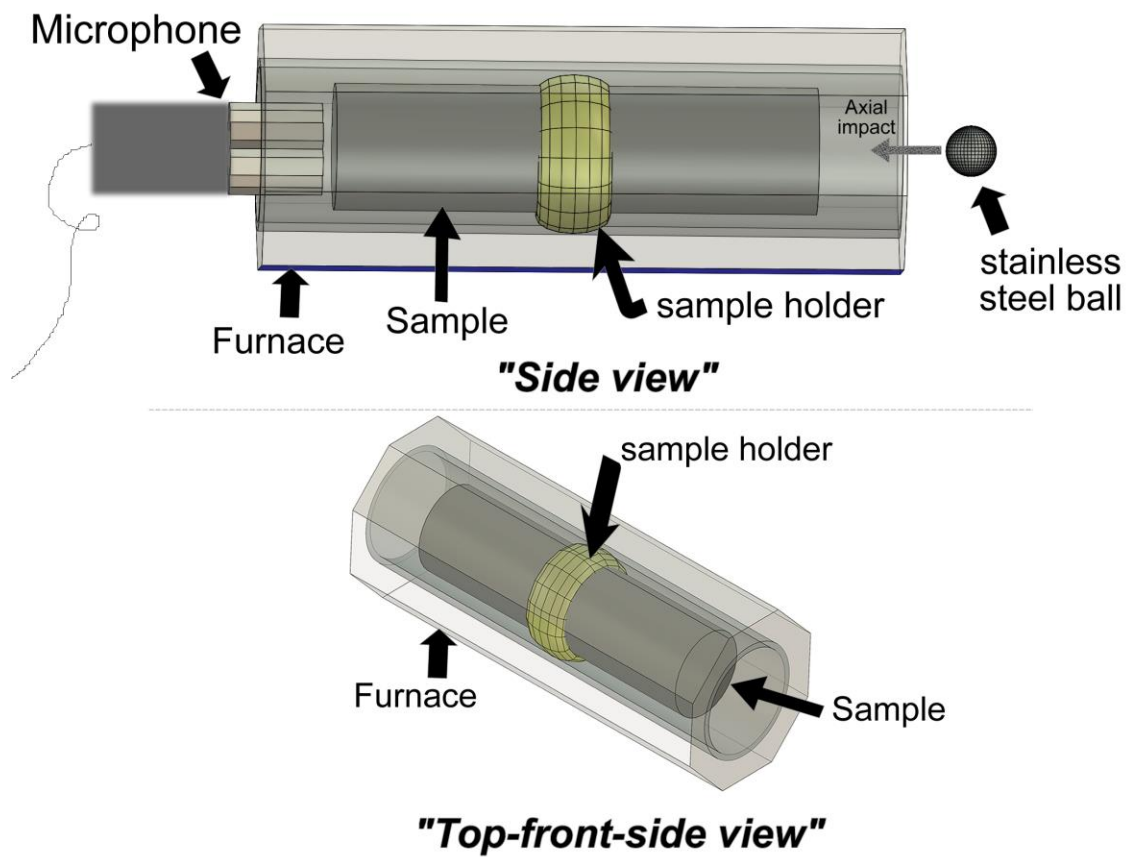


Figure 2.8 : Schematic of MS setup as sample installed in the furnace.

Chapter 3

ARTICLE 1: *P*-TYPE BISMUTH TELLURIDE-BASED COMPOSITE THERMOELECTRIC MATERIALS PRODUCED BY MECHANICAL ALLOYING AND HOT EXTRUSION

M.K. Keshavarz¹, D. Vasilevskiy¹, R.A. Masut¹, S. Turenne¹

¹École Polytechnique de Montréal, C.P. 6079, Succ. Centre-Ville, Montréal (Québec), H3C 3A7, Canada

This article published in Journal of Electronic Materials, Published in July 2013, Volume 42, Issue 7, pp 1429-1435, DOI: [10.1007/s11664-012-2284-2](https://doi.org/10.1007/s11664-012-2284-2), “The final publication is available at link.springer.com”.

Foreword

The interests and advantages in making composite TE materials were discussed in Chapter 1. It was mentioned that the goal of producing composite TE materials is mostly thermal conductivity reduction. However, one of the challenges in producing such materials is to improve other TE properties simultaneously or at least keep them intact.

As it was discussed in Chapter 1, the coherent and incoherent interfaces between different phases in composite materials have attracted more attention as an effective parameter to influence the physical and mechanical properties of composites. When the secondary phase and the matrix make coherent interface, both phases are in a good lattice alignment. In contrast, incoherent interface involves dissimilarity of lattice parameters of phases in the composite, which leads to a clear boundary between two phases. Although both coherent and incoherent interfaces in composites could significantly reduce the lattice thermal conductivity, several reports, as mentioned in Chapter 1, have shown a negative effect of incoherent interfaces on the electrical conductivity, which leads to power factor reduction in TE materials. Although the mechanisms of phonons and charge carrier scattering in each one is different to some extent, it has not yet been clarified to what extent the difference in the lattice parameter between the phases can affect the

electrical and thermal conductivity. It is predicted that coherent interfaces act more like point defects, but it is not clear from what order of alteration in lattice parameters of phases in the composite, the interface would have negative impact on charge carrier transport properties.

In this chapter we report synthesis and investigation of bismuth telluride based composite TE materials consisting of phases with similar crystal structures. We expected to keep the power factor from degrading when introducing more coherent interfaces between dissimilar phases in the composite. At the same time, these interfaces should lead to higher phonon scattering rates resulting in lower thermal conductivity.

3.1 Abstract

We produced six different composites of *p*-type bismuth antimony telluride alloys and studied their structure and thermoelectric properties. The components of the composites were obtained in powder form by mechanical alloying. Mixed powders of two different compositions were consolidated by hot extrusion to obtain each bulk composite. The minimum grain size of bulk composites as revealed by scanning electron microscopy shows a 50% reduction compared to the conventional $(\text{Bi}_{0.2}\text{Sb}_{0.8})_2\text{Te}_3$. XRD analysis only shows peak broadening with no clear indication of separate phases, and indicates a systematic decrease of crystallite size in the composite materials. Scattering mechanisms of charge carriers were evaluated by Hall effect measurements. The thermoelectric properties were investigated via the Harman method from 300K up to 460K. The composites show no significant degradation of the power factor and high peak *ZT* values ranging from 0.86 to 1.04. The thermal conductivity of the composites slightly increases with respect to the conventional alloy. This unexpected behavior can be attributed to two factors: (1) composites do not yet contain a significant number of grains whose sizes are sufficiently small to increase phonon scattering, and (2) each of the combined components of the composites corresponds to a phase with thermal conductivity higher than the minimum value corresponding to the $(\text{Bi}_{0.2}\text{Sb}_{0.8})_2\text{Te}_3$ alloy.

3.2 Introduction

Research to increase the thermoelectric (TE) figure of merit (*ZT*) is focused on a variety of novel materials and approaches. Reducing the grain size of polycrystalline TE materials down to the nano-scale has resulted in significant reduction of the lattice thermal conductivity and

improvement in the figure of merit [163, 164]. Important advances have come in recent years from the development of nanostructured semiconductors due to thermal conductivity reduction [165-168]. These results have encouraged researchers to investigate other approaches to decrease the thermal conductivity of TE materials while conserving their electrical conductivity. Besides reducing grain size to the nanometer scale, another perhaps more advantageous approach, is the introduction of a high density of interfaces between dissimilar materials [1, 24].

Bismuth telluride based alloys are known as one of the most efficient TE materials for refrigeration or power generation near room temperature [164]. Several attempts have been carried out to reduce the grain size of bismuth telluride based alloys, finally resulting in a lower lattice thermal conductivity [163, 169]. On the other hand, using nanocomposites such as those obtained by adding foreign nano-inclusions in bulk materials may affect the carrier mobility and lead to the reduction of electrical conductivity as well as thermal conductivity [170, 171]. In contrast, dissimilar grain boundaries, which are efficient phonon scatterers, have an effect on the transport of electrons that depends on their ordering and coherence [109, 164].

In this work, we introduce interfaces by mixing two different compositions (or phases) of bismuth telluride based alloys. We believe that phases with similar electronic and crystal structure may better keep carrier coherence and consequently conserve the mobility of carriers while increasing phonon scattering at the boundaries between phases or grains. To obtain such composite materials, different compositions were synthesized by mechanical alloying of pure elements and then mixed in pairs followed by hot extrusion consolidation. As is explained in detail in the following section, the compositions of the constituents and their proportions are carefully controlled so that on the average they have the same atomic density as that of homogeneous $(\text{Bi}_{0.2}\text{Sb}_{0.8})_2\text{Te}_3$, the conventional alloy. The microstructure, TE and carriers' transport properties of each composite were investigated and compared to the conventional alloy. Our goal is to understand the effect of the scattering mechanisms, introduced by the composites that we produce, on carrier and thermal transport. We obtain indications that our composites, as produced, do not significantly affect the power factor, but contrary to expectations, we observe a slight increase in their thermal conductivity. The remaining challenges of this approach will be identified and discussed.

3.3 Experimental procedures

Due to our previous studies on homogeneous alloys of bismuth (Bi), antimony (Sb) and tellurium (Te), the maximum TE performance is obtainable when the molar ratio of bismuth to antimony in the alloy is 1:4. Thus, to make the composite materials comparable with the conventional $(\text{Bi}_{0.2}\text{Sb}_{0.8})_2\text{Te}_3$ alloy the total molar ratio of bismuth to antimony in all composites was maintained constant as 1:4. A variety of compositions in powder form were produced that ranged in composition from somewhat similar to the conventional homogenous ternary alloy, to the extreme of two binary compounds of bismuth telluride and antimony telluride. The list of the composites, detailing the different phases which were mixed, is presented in Table 3.1.

High purity (99.99% or above) pellets of Bi, Sb and Te were used as starting materials for synthesis of different phases by mechanical alloying for 10 hours. Each selected pair of powders was then mixed manually in a container and sieving was repeated three times not only to remove larger particles or contaminations but also to complete the mixing process. X-ray Diffraction (XRD) analyses of several samples confirmed the homogeneity of the mixture. The mixture was then introduced into the extrusion cylinder for hot extrusion, which was carried out at a fixed temperature in the range of 360 to 460°C, depending on material load and applied pressure. All processing steps were carried out under an argon atmosphere. The final composite products are in the shape of rods with 2.54 cm diameter and 40 cm length. A detailed description of the mechanical alloying and hot extrusion processes can be found in ref. [172]. For comparative analysis of thermoelectric properties we targeted the same charge carrier concentration of $2 \times 10^{19} \text{ cm}^{-3}$ for each composite as well as the conventional alloy. This was done by doping with Sb, which is a common process for the homogeneous bismuth telluride based *p*-type alloys.

The microstructure and phase analysis of powders and bulk composites were investigated by scanning electron microscopy (SEM), for which bulk samples were mechanically polished and underwent an electrolytic etching to reveal grain boundaries. X-ray diffraction (XRD) was used to analyze evolution of texture and grain size of extruded composites. The thermoelectric properties including Seebeck coefficient, thermal conductivity, electrical resistivity and figure of merit of all the composites in Table 3.1 were evaluated via the Harman method from 300K up to 440K on cubic samples (5mm side) with electrodeposited Ni coatings on two opposite faces. Hall Effect measurements were carried out as a function of temperature between 15-360 K to obtain

carriers' concentration and mobility. Samples for Hall measurements were cut from Harman's samples to square laminas 0.5 mm thick, with indium "point" contacts on their corners.

Table 3.1: Composition and weight percentage of different phases mixed in powder form to produce composite TE alloys by hot extrusion.

Composite #	Phases in the composite		Weight %	
0 (Conventional)	$(\text{Bi}_{0.2} \text{Sb}_{0.8})_2 \text{Te}_3$		100	
	Phase 1	Phase 2	Phase 1	Phase 2
1	$(\text{Bi}_{0.24} \text{Sb}_{0.76})_2 \text{Te}_3$	$(\text{Bi}_{0.16} \text{Sb}_{0.84})_2 \text{Te}_3$	50.51	49.49
2	$(\text{Bi}_{0.28} \text{Sb}_{0.72})_2 \text{Te}_3$	$(\text{Bi}_{0.12} \text{Sb}_{0.88})_2 \text{Te}_3$	51.05	48.95
3	$(\text{Bi}_{0.32} \text{Sb}_{0.68})_2 \text{Te}_3$	$(\text{Bi}_{0.08} \text{Sb}_{0.92})_2 \text{Te}_3$	51.6	48.4
4	$(\text{Bi}_{0.36} \text{Sb}_{0.64})_2 \text{Te}_3$	$(\text{Bi}_{0.04} \text{Sb}_{0.96})_2 \text{Te}_3$	52.2	47.8
5	$(\text{Bi}_{0.4} \text{Sb}_{0.6})_2 \text{Te}_3$	$\text{Sb}_2 \text{Te}_3$	52.7	47.3
6	$\text{Bi}_2 \text{Te}_3$	$\text{Sb}_2 \text{Te}_3$	24.2	75.8

3.4 Results and discussion

3.4.1 Microstructure and grain size

Bismuth telluride based alloys have marked anisotropic properties, and as a result it is necessary to texture the material to obtain a better performance in a particular orientation. In our study, such texturing was produced by the hot extrusion process. However, at the beginning of the extruded rods (first few centimeters), the grain structure is not yet as well textured as the remaining lengths of the rods in both the conventional alloy and in the composites. Also, the first portion of the extruded powders spends less time exposed to high temperature, consequently favoring

conservation of the nanostructure obtained during mechanical alloying. The rest of each extruded rod, on the other hand, is well textured and shows homogenous properties throughout. Microstructural analyses of the conventional alloy and of the composites prepared by hot extrusion show grains of about the same size, in the range from 1 to 3 μm , for all samples in the homogenous portions of the rods (Figure 3.1). In contrast, the microstructure at the front ends of the extruded rods in all composites shows about 50% reduction in grain size in comparison with the conventional alloy (compare Figure 3.2 (a) and (b)). SEM backscattered electrons images (Figure 3.2) illustrate lamellae within the grains in both the conventional alloy and a typical composite (# 5), where one can observe that distances between lamellae are much shorter in the composite. In addition, there are different contrast levels in several grains as demonstrated in Figure 3.2 (b) that could be due to different phases presented in the composite materials. These contrast levels are observed both at the front end of the extruded rods and in the homogenous part of the rods.

The crystal structure of the phases in all composites are similar, consequently, diffraction of X-rays from planes of different phases in each composite lead mostly to peak broadening instead of two separate peaks for each plane due to the lack of homogeneity of the materials (See Figure 3.3). Since we were unable to clearly identify separate peaks of different phases, we assumed each composite as a single phase material to evaluate the peak broadening in the composite series. Peak broadening was clearly observed in the composite materials which led to a reduction in the calculated average crystallite size of the composites. The crystallite size which is the size of an average coherent scattering domain, and represents a region with perfect arrangement of unit cells or perfect crystals was obtained from XRD using Scherrer's formula and averaging over the most intense diffraction planes. To calculate the average crystallite size of each sample we selected the seven most intense diffraction peaks of the XRD pattern. Figure 3.4 shows these calculated crystallite sizes for all the composites including the conventional alloy. The composition numbers correspond to each composite material and "0" represents the conventional alloy as it has been detailed in Table 3.1.

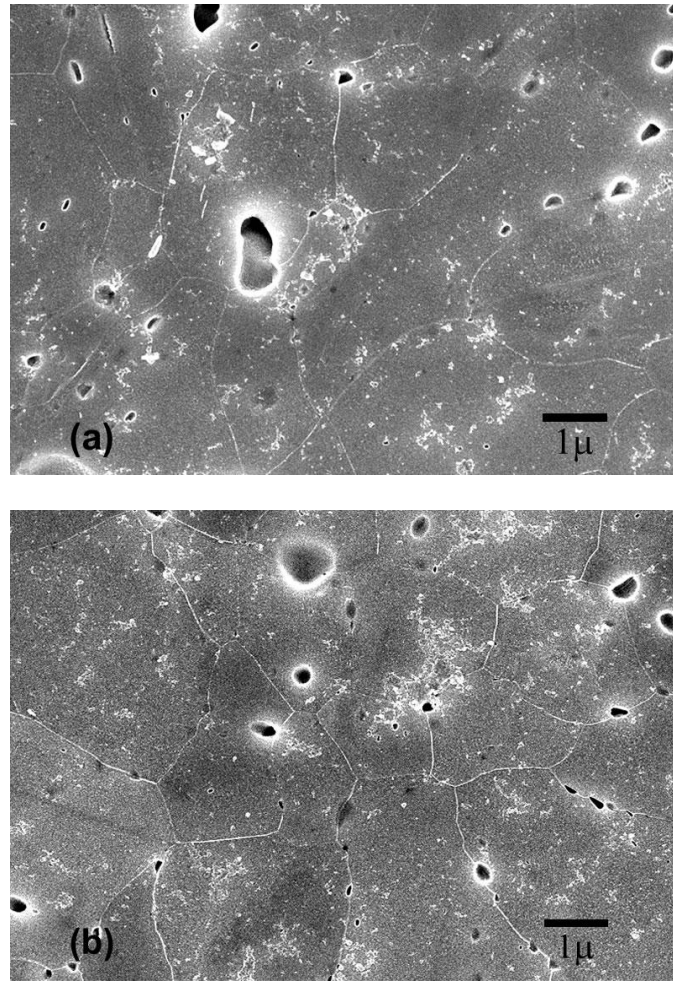


Figure 3.1: Microstructure of homogenous part of the extruded rods in conventional alloy (a) and composite #6 (b) obtained by using Secondary electron images. The porosity is typical for hot extruded alloys.

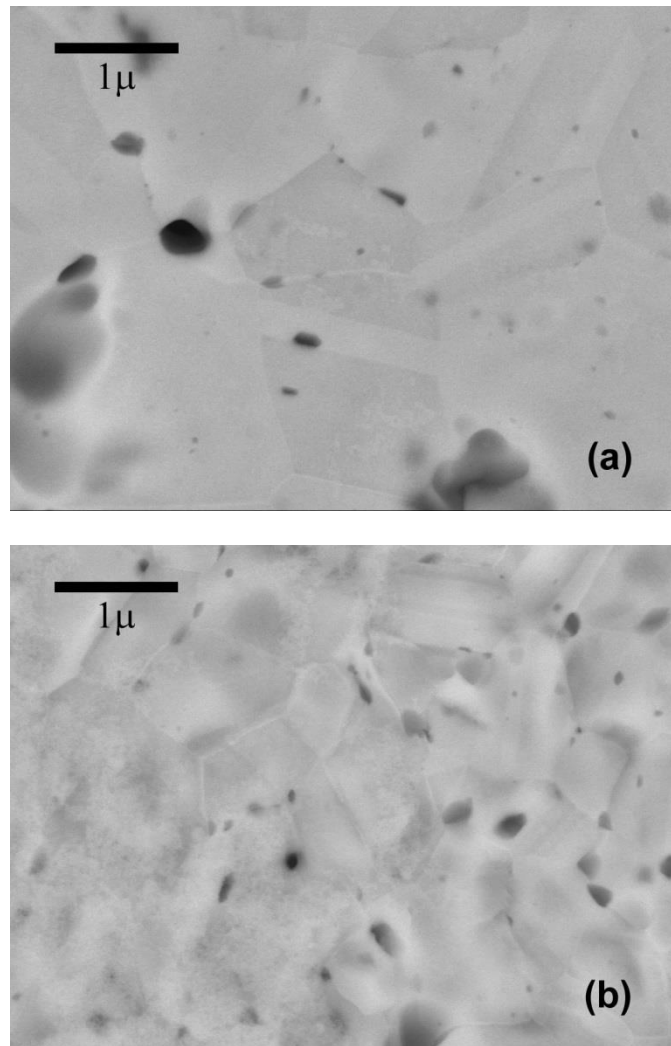


Figure 3.2: Backscattered electron images showing the microstructure at the beginning of the extruded rods in conventional alloy (a), and in composite #5 (b). Observe the grains size reduction and the lamellae within grains (stacking faults or twins). They are much smaller in the composites.

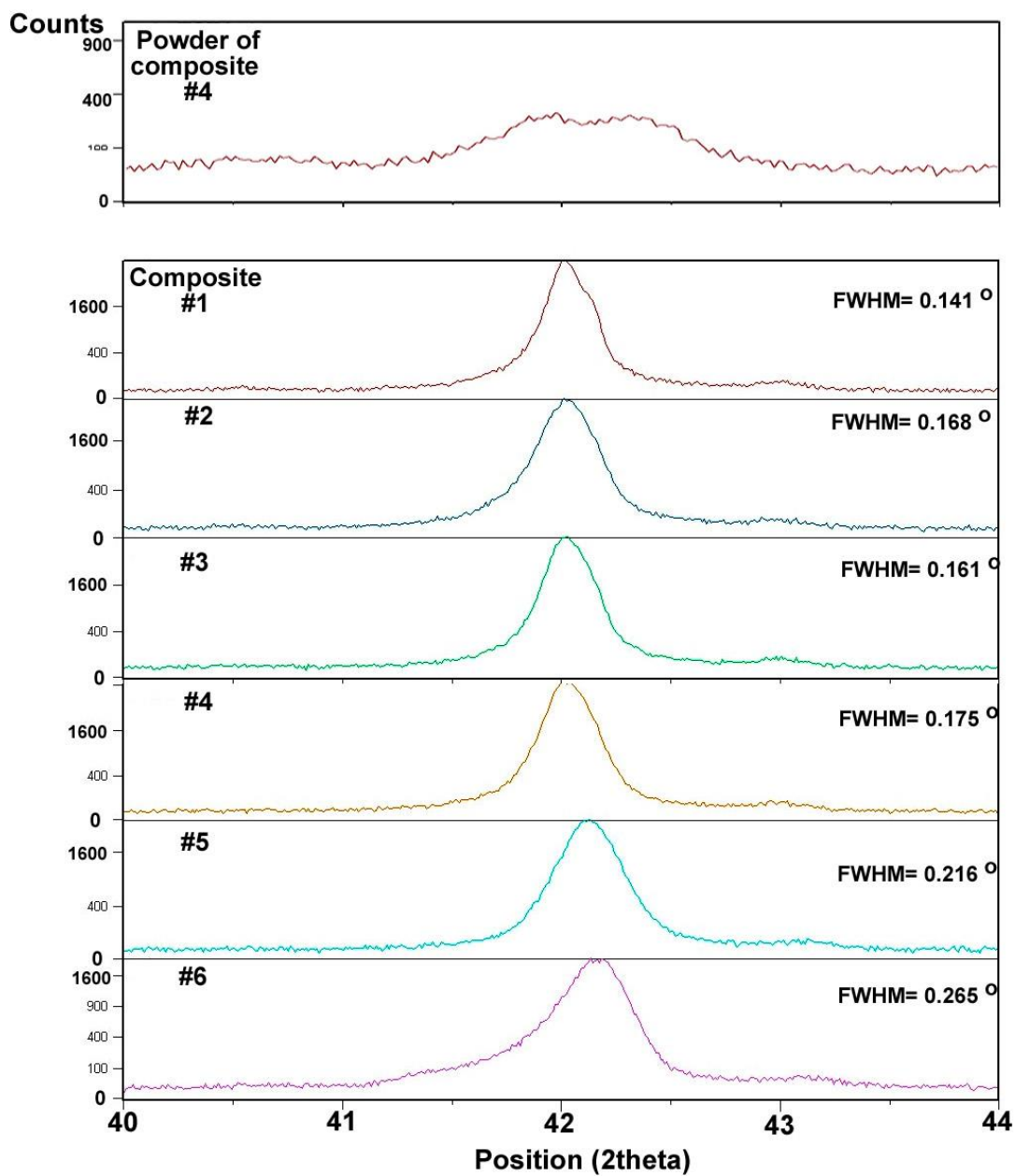


Figure 3.3 : Evolution of peak broadening in the composites for the (110) and (113) diffracting planes. There is no conclusive evidence of separate peaks in these curves.

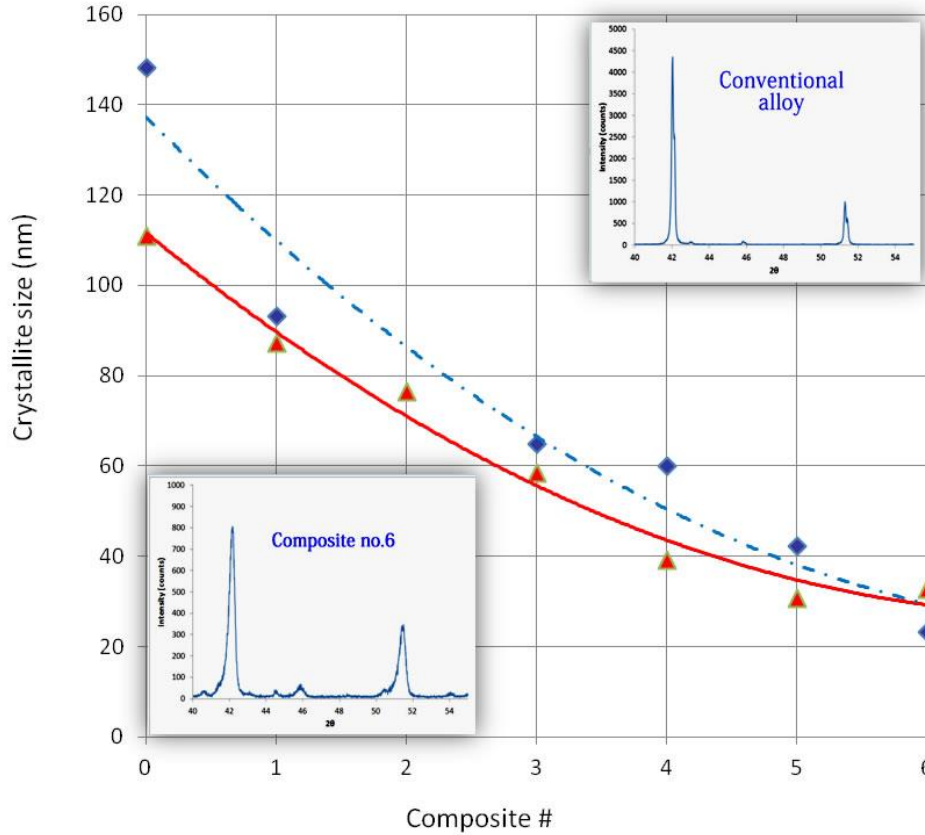


Figure 3.4: Calculated crystal sizes from XRD data of extruded composites and conventional alloy from the homogenous part of the rods (blue diamonds) and from the beginning of the extruded rods (red triangles). Inserted XRD patterns for conventional alloy and composite #6 illustrate peak broadening (patterns taken from the homogeneous part).

3.4.2 Carrier transport analysis

XRD analysis of the composites indicates that the structure of the composites is different from that of the conventional alloy. This difference in structure may affect carrier and phonon transport properties in the material. To study the behavior of charge carriers in the composites they were characterized from 15 K to 360 K using Hall effect measurements. Since there are several possible scattering mechanisms present in these alloys [173], the total mobility should contain at least the following contributions

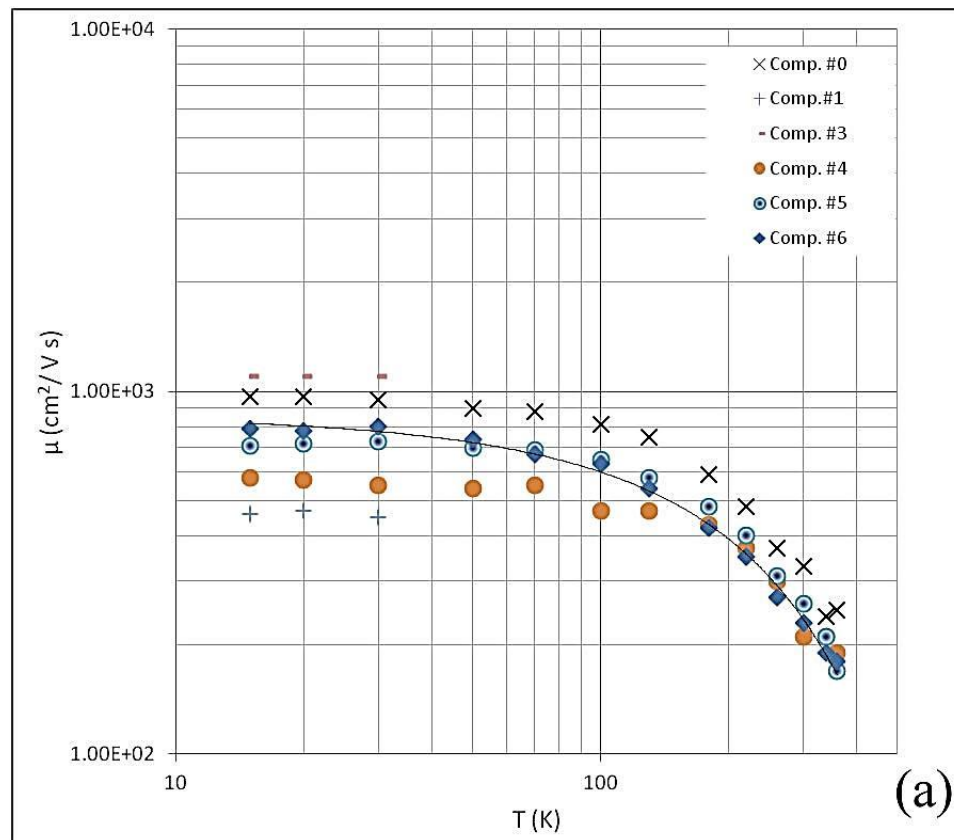
$$1/\mu = 1/\mu_{ii} + 1/\mu_{ph} + 1/\mu_{alloy} + 1/\mu_{comp}. \quad (3.1)$$

which represent scattering from ionized impurities (ii) and lattice vibrations (ph), alloy scattering, and the additional effect of possible composite interfaces on carrier scattering.

The mass and the strain field fluctuations caused by the difference of masses and radii between the impurities atoms and the host atoms in alloyed materials effectively scatter only the phonons. In these alloys, the scattering of charge carriers has been mainly attributed to the difference ΔX between the electronegativities of the substituting elements [174]. In our particular case, since the difference ΔX for bismuth and antimony is relatively small ($X(\text{Bi}) - X(\text{Sb}) = 0.03 \text{ eV}$, as compared to 0.45 eV between Te and Se), the scattering due to alloying is thus expected to be negligible, and in the absence of any evidence of its impact we will ignore it.

Figure 3.5(a) shows plots of Hall mobility versus temperature comparing the six composites to the conventional alloy.

The Hall effect measurement system we used does not allow sample temperatures exceeding room temperature; therefore we used Harman test results from room temperature up to 380K to obtain the conductivity for a larger temperature range (Figure 3.5 (b)).



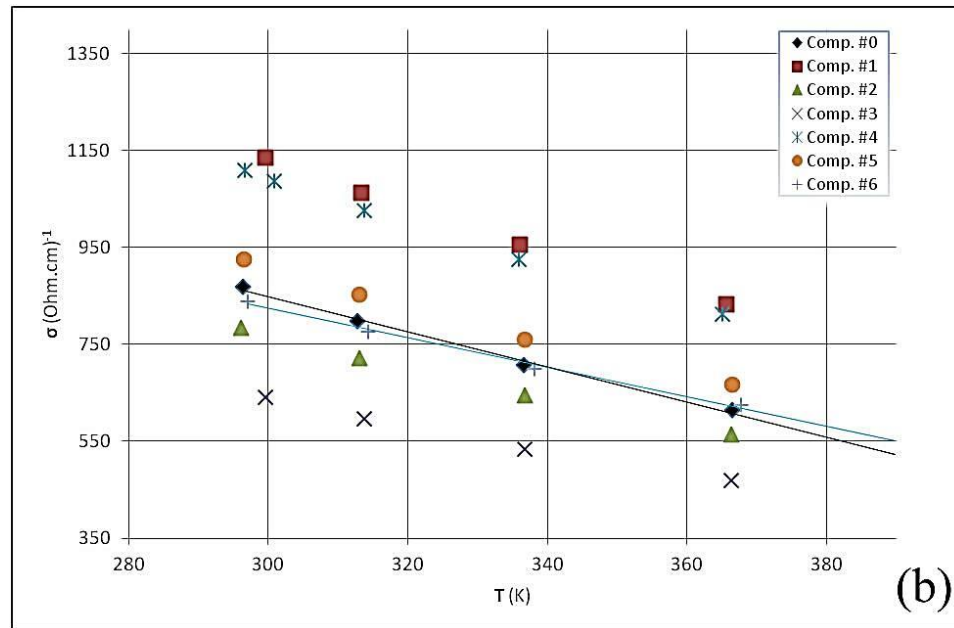


Figure 3.5: (a) Hole Hall Mobility vs. temperature obtained from Hall measurements in the range 15-360K, (b) Conductivity vs. temperature from Harman measurements in the range 290-380K.

In the higher temperature range (Figure 3.5 (b)) the plot of electrical conductivity vs. temperature for all samples shows the expected behavior for holes transport controlled only by acoustic phonons.

Although an examination of the temperature dependence of the Hall effect is the usual procedure to determine the scattering mechanisms, we note that different theoretical models of ionized impurity scattering have been proposed [175], and they do not agree for doping levels higher than 10^{18} cm^{-3} , which is the case for this study. However, they do agree that the inverse mobility is proportional to the concentration of the scattering centers. Figure 3.6 shows a linear relationship passing through the origin for the inverse Hall mobility, measured at 15K, as a function of charge carrier concentration (each composite has a different carrier concentration, not all values are near the targeted value). This result reveals that at low temperature holes are predominantly scattered by ionized impurities, and there is no evidence of a mechanism specifically linked to the composite nature of the studied materials. In other words, the mobility values of holes in composites are limited by two dominant scattering mechanisms: ionized impurity scattering at lower temperatures and acoustic phonon scattering near and above room temperature. If the additional interfaces of the composites have any effect on the transport properties, then these effects clearly remain below the identified mechanisms, and can be ignored compared to them.

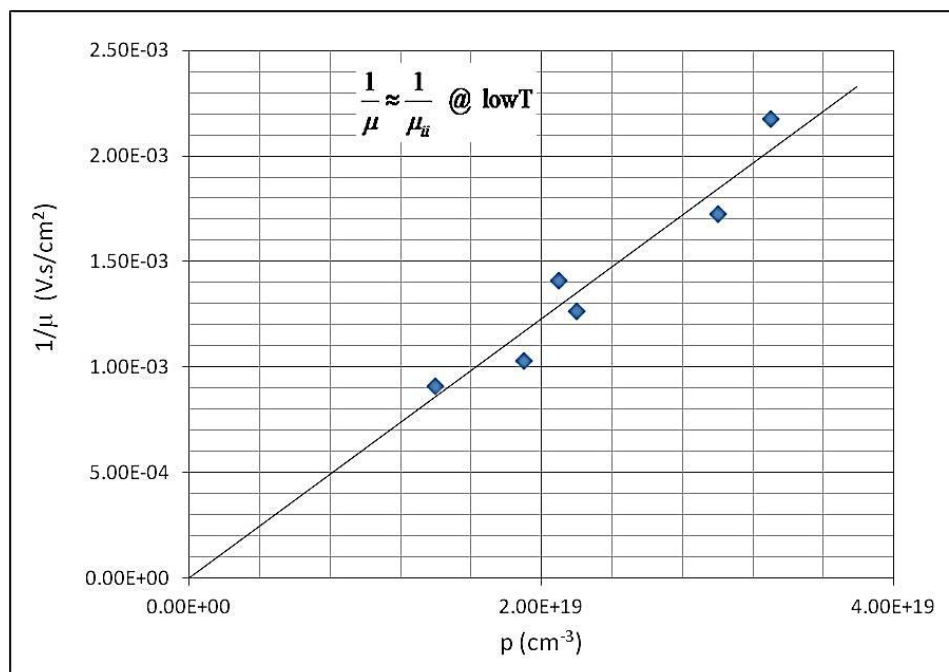


Figure 3.6: Inverse Hall mobility vs. carrier concentration at $T=15\text{K}$ acquired from Hall measurements.

3.4.3 Thermoelectric properties

As was shown in the previous section, the concentration of charge carriers is different for each composite, which displaces the peak ZT values as a function of temperature. Thus, to better compare the performance of different composites, we evaluated the dimensionless figure of merit ZT of all composites in the temperature interval from 295K to 460K, containing their peak values, and calculated the maximum ZT value for each composite. Figure 3.7 shows the peak ZT values of the composites, which are compared with those of the conventional homogeneous $(\text{Bi}_{0.2}\text{Sb}_{0.8})_2\text{Te}_3$ ternary alloy. The measured peak ZT values in the samples prepared from the front ends of the extruded rods are always lower than those of samples prepared from the homogeneous parts of the rods, which can simply be explained by degrees of texturing of an anisotropic material. The peak ZT values decrease almost monotonically when changing the composition from the conventional ternary alloy (0) to the composite (#6) with the two most extremely separated phases. However, they remain within a range from 0.86 to 1.04, which indicates an acceptable, if not optimal, performance.

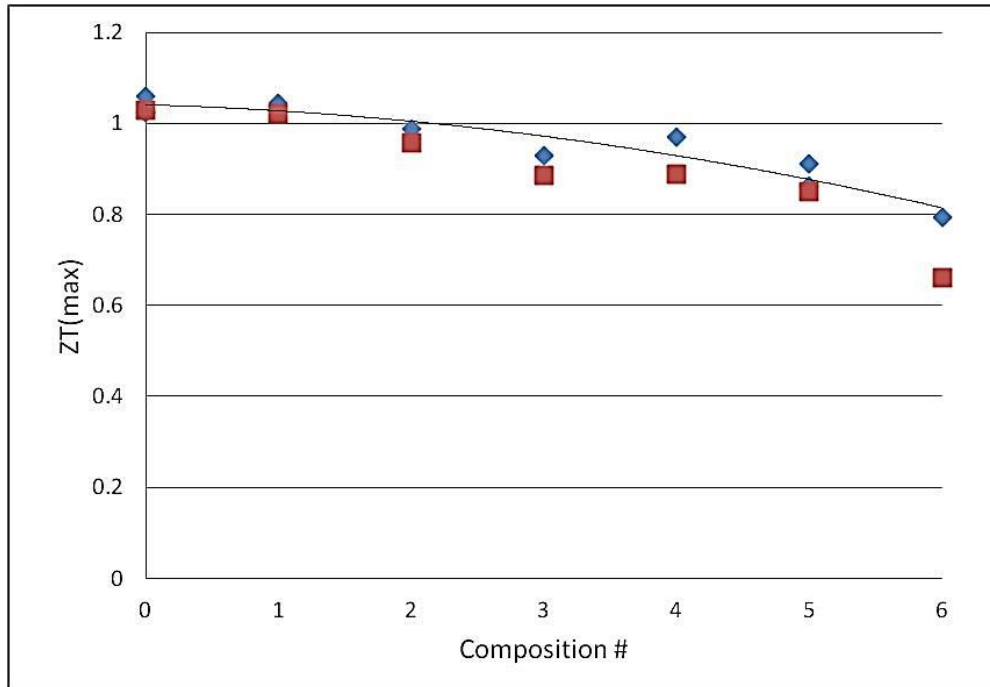


Figure 3.7: Peak ZT values of all composites and conventional alloy for both beginning (red squares) and homogenous part (blue diamonds) of the extruded rods. The solid line is included to highlight the decrease in peak ZT values in composites.

As is shown in Figure 3.8, there is no major degradation of the power factor ($PF = \alpha^2 \sigma$, where α is the Seebeck coefficient and σ is the electrical conductivity) of the composites. This result confirms that the composites do not seem to provide a significant effect (positive or negative) on the carrier transport properties.

On the other hand, the thermal conductivity of the composites showed a slight increasing trend, whereas a reduction was expected. (Figure 3.9). Two factors acting in conjunction can explain this increase: i) composites do not yet contain a significant number of grains whose sizes are sufficiently small to increase phonon scattering, and ii) each of the combined components of the composites corresponds to a phase with thermal conductivity higher than the minimum value corresponding to the $(\text{Bi}_{0.2}\text{Sb}_{0.8})_2\text{Te}_3$ alloy.

The second cause can be better understood by looking at the lattice thermal conductivity data as a function of composition for the $(\text{Bi}_x\text{Sb}_{1-x})_2\text{Te}_3$ alloys, presented in Figure 3.10. Each bulk composite was fabricated from two different phases, whose original compositions (from Table 3.1) are plotted on the same figure (right scale). As the figure shows, the thermal

conductivity of the composites is not expected to fit with the minimum lattice thermal conductivity of the single phase conventional alloy, it rather falls on the increased values to the right or left of the minimum. For example, using Birkholz data [24] and composite #5 with 47.3 wt.% of Sb_2Te_3 and 52.7 wt.% of $(\text{Bi}_{0.2}\text{Sb}_{0.6})_2\text{Te}_3$ we estimate lattice thermal conductivities of the phases as 2.33 and $1.13 \text{ Wm}^{-1} \text{ K}^{-1}$, respectively, while the minimum lattice thermal conductivity on that plot is $1.1 \text{ Wm}^{-1} \text{ K}^{-1}$.

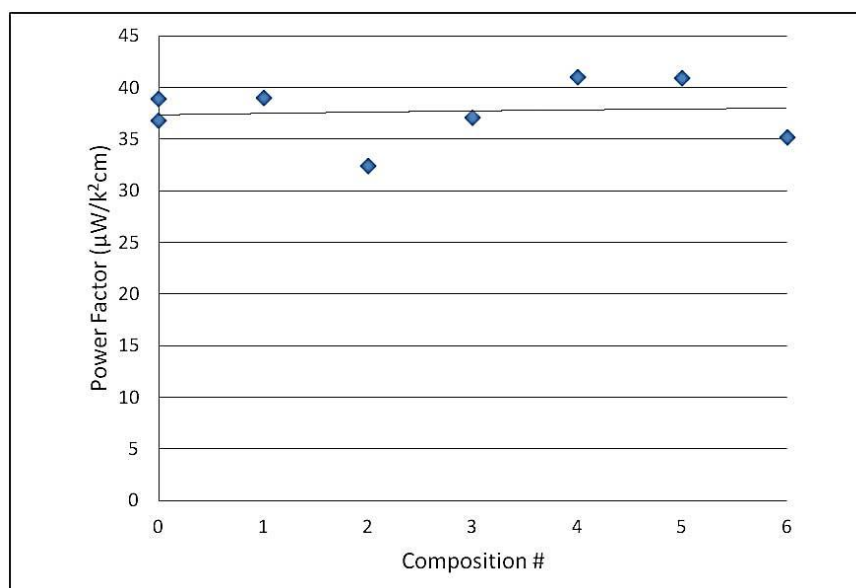


Figure 3.8: Maximum power factor of the conventional alloy and of the composites as was measured by our Harman setup. The solid line is included as a guide showing the overall tendency of the power factor.

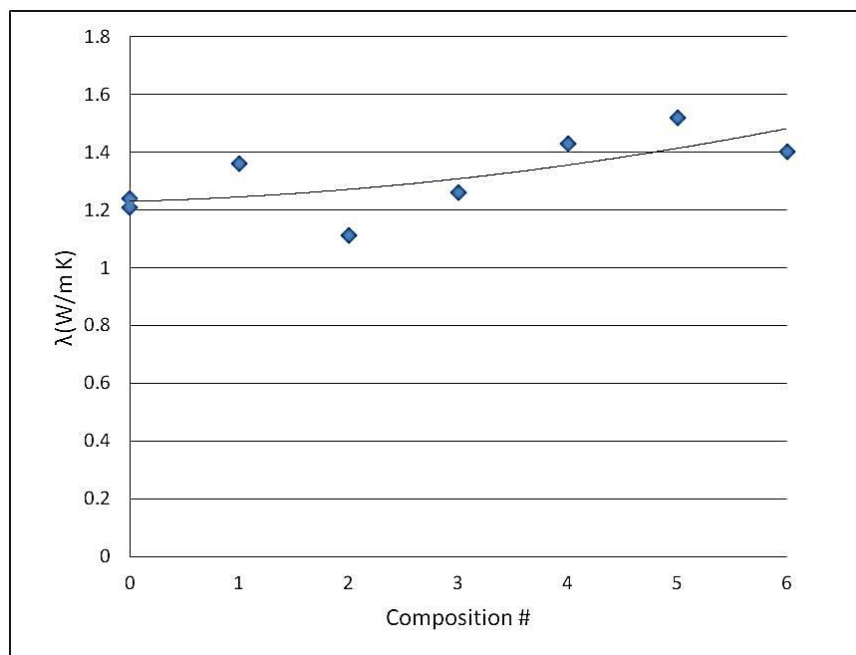


Figure 3.9: Thermal conductivities of the composites and the conventional alloy as were obtained by Harman measurements. The solid line is included to highlight the upward trend.

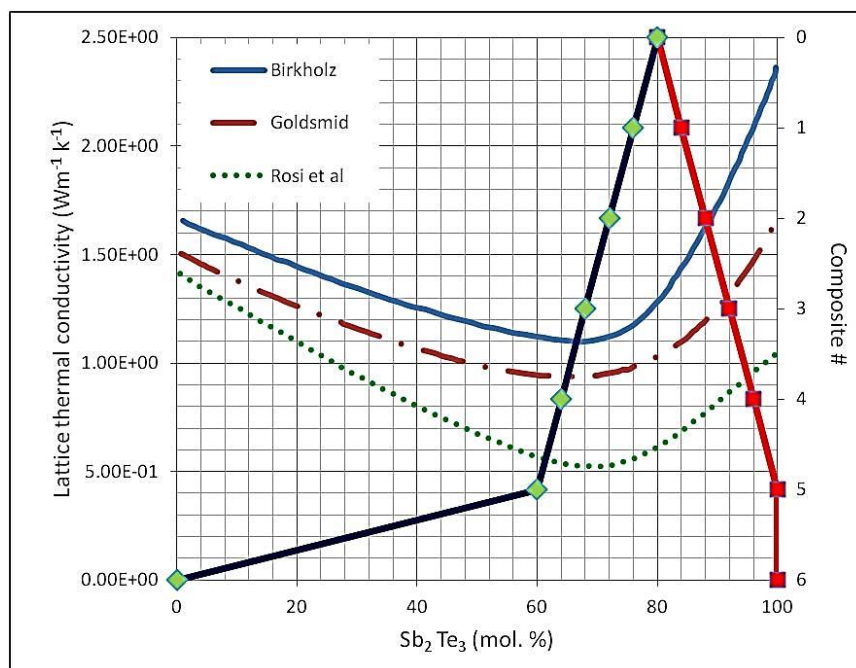


Figure 3.10: The composition (from Table 3.1) of the constituents of the composite materials (# on right axis) showing the molar percentage of Sb₂Te₃ in each phase (phase 1: green diamonds and phase 2: red squares). The graph also shows the values of the thermal conductivity (left axis) taken from the literature [24].

3.5 Conclusion

We have produced *p*-type $(\text{Bi}_x\text{Sb}_{1-x})_2\text{Te}_3$ composites whose grain sizes show a significant reduction compared to the conventional alloy. According to our XRD analysis, crystallites show a systematic decrease in size as the composite phases become more different from the conventional alloy. However, we cannot rule out that peak broadening in the composites may be due to the existence of multi-phases in the material in which case the true crystal size of the composites should be between the lower limit (shown in Figure 3.4) and the upper limit (that of the conventional alloy). Transport and TE properties indicate no degradation of the power factor, and the peak *ZT* values of the composites decrease from 1.04 to 0.86. Contrary to expectations, the thermal conductivity of the composites increases, which may be due to two concurrent factors: (1) the combined components of the chosen composites do not seem to correspond to a molar composition with the minimum thermal conductivity for this alloy system; and (2) composites do not yet contain a significant number of grains whose sizes are sufficiently small to increase phonon scattering.

3.6 Further discussion

Although the lattice parameters of phases used to produce composites as presented in Table 3.1, mostly need to be calculated, some examples of lattice parameters of similar phases to those alloys are given in Table 3.2. As shown, the differences in lattice parameters of these alloys are almost negligible. Our study of the transport properties of the composites proved that coherent interfaces made by dissimilar phases when they have somewhat similar lattice parameters do not have significant negative effect on charge carrier transport. The Hall effect results show that there is not substantial carriers scattering due to interfaces of dissimilar phases, resulting in no degradation of the power factor of these composites.

Table 3.2 : Lattice parameters of alloys based on Bi, Sb, and Te (adapted from database of X'pert Highscore analyzer software).

Phase Lattice parameters	$(\text{Bi}_{0.5}\text{Sb}_{0.5})_2\text{Te}_3$	$(\text{Bi}_{0.2}\text{Sb}_{0.8})_2\text{Te}_3$	$\text{Bi}_{0.5}\text{Sb}_{1.5}\text{Te}_3$	Sb_2Te_3	Bi_2Te_3
a (Å)	4.33	4.3	4.28	4.26	4.39
b (Å)	4.33	4.3	4.28	4.26	4.39
c (Å)	30.40	30.28	30.52	30.45	30.44

Chapter 4

**ARTICLE 2: SYNTHESIS AND CHARACTERIZATION OF BISMUTH
TELLURIDE-BASED THERMOELECTRIC NANOCOMPOSITES
CONTAINING MoS₂ NANO-INCLUSIONS**

Mohsen K. Keshavarz, [†] Dimitri Vasilevskiy, [†] Remo A. Masut,[‡] and Sylvain Turenne[†]

[†]Department of Mechanical Engineering, École Polytechnique de Montréal, Montréal, Québec, H3C 3A7, Canada

[‡]Regroupement québécois sur les matériaux de pointe (RQMP) and Department of Engineering Physics, École Polytechnique de Montréal, Montréal, Québec, H3C 3A7, Canada

This article is submitted to Journal of Materials Characterization, Submitted in March, 2014.

Foreword

In the previous chapter we presented our efforts to produce TE composites of Bi, Sb, Te alloys with coherent interfaces between dissimilar phases. We investigated TE properties of the composites produced; however, thermal conductivity of composites was not reduced as was expected. One of the main reasons for this behavior, as we mentioned in Chapter 3, could be size of grains in these composites, which are probably not small enough to promote phonon scattering. Still, the grain growth inhibition was observed in the composites comparing to the conventional single alloy.

The idea presented in this chapter is related to grain growth suppression by adding a secondary phase in the TE matrix. Several reports of thermal conductivity reduction due to nano-inclusions in the TE materials, as well as special structure of molybdenum disulfide that makes it a well-known solid lubricant that could facilitate the extrusion process, gave us the motivation to synthesize and study bismuth telluride based nanocomposites containing molybdenum disulfide nano-inclusions.

In this chapter, synthesis of nanocomposites with different percentages of nano-inclusions is explained. The formation and dispersion of nano-inclusions were analyzed, and the impact of nano-inclusions on the microstructural, and crystalline sizes and defects was investigated.

4.1 Abstract

Bulk nanocomposites of $(\text{Bi}_{0.2}\text{Sb}_{0.8})_2\text{Te}_3$ and $(\text{Bi}_{0.95}\text{Sb}_{0.05})_2(\text{Te}_{0.95}\text{Se}_{0.05})_3$ containing MoS_2 nano-inclusions were obtained by mechanical alloying and hot extrusion. The nano-inclusions are observed to decorate the grain boundaries of the matrix, leading to a significant reduction of average grain size and crystallite size compared to those of the conventional single phase alloy. Consequently, the thermal conductivity of these nanocomposites also decreases (~ 1.4 W/m·K at 450 K for 0.4 wt.% MoS_2) when compared to the conventional alloy (~ 1.8 W/m·K). The structural changes in the nanocomposites obtained by mechanical spectroscopy in the temperature range 293-540 K show an increase of the internal friction accompanied by a systematic reduction of its activation energy with increase in MoS_2 content.

4.2 Introduction

In the past decade, considerable progress has been made in the development of thermoelectric (TE) materials for energy conversion devices [19, 21, 176]. The TE material performance is usually characterized by a dimensionless figure of merit $ZT = \sigma\alpha^2 T/\lambda$, where σ is the electrical conductivity, α stands for the Seebeck coefficient, T and λ are the absolute temperature and thermal conductivity, respectively [1]. One approach to enhance the performance of TE materials is to reduce the lattice thermal conductivity. Studies have shown that to reduce this contribution to the thermal conductivity, a higher density of interfaces in any geometry can be useful [177]. To enhance phonon scattering and consequently decrease thermal conductivity, nanostructures with size smaller than the phonon mean free path have been suggested [178]. TE nanocomposites produced by adding nano-inclusions or mixing particles of a nanostructured phase or of dissimilar phases have been reported as sources of increased phonon scattering [40, 42, 43, 104]. Several types of nano-inclusions or nano-particles such as semiconductors, metals, semimetals and ceramics including carbon nanotubes or fullerenes have been introduced in a variety of TE

materials [40, 41, 46, 179, 180]. Yet, little is known about their effects on structural and mechanical properties important for module fabrication and reliability.

In this work we introduce nano-particles of molybdenum disulfide (MoS_2) as a secondary phase in a bismuth telluride based alloy to produce TE nanocomposites. MoS_2 is well known as a solid lubricant; however it is also a semiconductor with interesting electronic properties [92, 132, 136] and we expect that the tendency of this material to create flakes with a few atomic layers could generate inclusions small enough for effective phonon scattering. We were able to implement such nanocomposites by powder metallurgy, and will show the considerable reduction of thermal conductivity as well as the induced changes in structural properties.

4.3 Experimental procedure

For the preparation of nanostructured powders of $(\text{Bi}_{0.2}\text{Sb}_{0.8})_2\text{Te}_3$, shots of 5N-purity elements of Bi, Sb and Te were proportionally weighed and mixed under an inert atmosphere of argon. In addition, Sb was used as a *p*-type dopant in quantities of 0.09 - 0.18 wt.%. Then, the mixed elements were mechanically alloyed in an attritor for 15 hours. To obtain the nanocomposites, pure (99.99%) nanoparticles of MoS_2 with a nominal particle size smaller than 90 nm (supplied by MKnano, Division of M K Impex Corp.) were added to the already synthesized powders of $(\text{Bi}_{0.2}\text{Sb}_{0.8})_2\text{Te}_3$ in the attritor tank and mixed for 1-4 hours. Concentrations of MoS_2 in the range from zero (conventional single phase alloy) to 0.8 wt.% were introduced in the nanocomposite compounds $(\text{Bi}_{0.2}\text{Sb}_{0.8})_2\text{Te}_3:\text{MoS}_2$. The mixtures were sieved ($\leq 180\mu\text{m}$) prior to extrusion processing. The hot extrusion was carried out at temperatures in a range from 653 to 733 K with the same extrusion rate (~ 0.6 mm/min) for all composites. All the steps were completed under Ar atmosphere to avoid any oxidation. A similar procedure was carried out to produce *n*-type $(\text{Bi}_{0.95}\text{Sb}_{0.05})_2(\text{Te}_{0.95}\text{Se}_{0.05})_3$ compound as a single phase conventional alloy and one *n*-type nanocomposite containing 0.3 wt.% MoS_2 . The donor dopant in the *n*-type materials was SbI_3 , in form of tiny chunks.

A JEOL JEM-2100F high-resolution transmission electron microscope (HRTEM) was used to analyze the nanostructure of the nanocomposites and energy dispersive x-ray spectrometry (EDX) with convergent beam in the HRTEM utilized for elemental composition analysis. All samples for HRTEM observation were in powder form. Powdered samples of extruded

nanocomposites were obtained as a byproduct of sawing them with a diamond blade saw. Chemical compositions of the nanocomposite samples were characterized by x-ray diffraction (XRD). The mean crystallite size of the extruded bulk nanocomposites was calculated using Scherrer's equation. A JEOL JSM-7600 TFE high-resolution scanning electron microscope (SEM) was used to assess the microstructure of nanocomposites, while the surface microstructure was revealed by electrolytic etching.

Using the mechanical spectroscopy (MS) setup described in ref. [181], the structural changes in our nanocomposites were evaluated and compared to the conventional *n*- and *p*-type alloys. The MS measurements were carried out from room temperature to 573 K.

Figure of merit (*ZT*) and values of α and σ were measured using ZT-Scanner 2.3 based on the Harman setup [173, 182] in the temperature range 290 to 480 K, from which we also obtain a measurement of λ . Cubic samples of 5 mm edges with Ni plated contacts on two opposite polished faces were prepared for Harman tests.

4.4 Results and discussion

HRTEM images and EDX analysis of the extruded nanocomposites confirm the presence of MoS₂ nano-particles in these samples. Figure 4.1(a) illustrates several nano-particles of MoS₂ decorating one whole side of a matrix grain. Nano-particles of MoS₂ were generally observed in a nano-flake shape, as we expected, having a few atomic layers thickness at grain boundaries (Figure 4.1(b)). The observed distances between the dark layers in the HRTEM images of MoS₂ nano-particles is 0.63 nm, which is comparable with the reported inter-planar Mo distance in single-layer MoS₂ (~0.615 nm) [133].

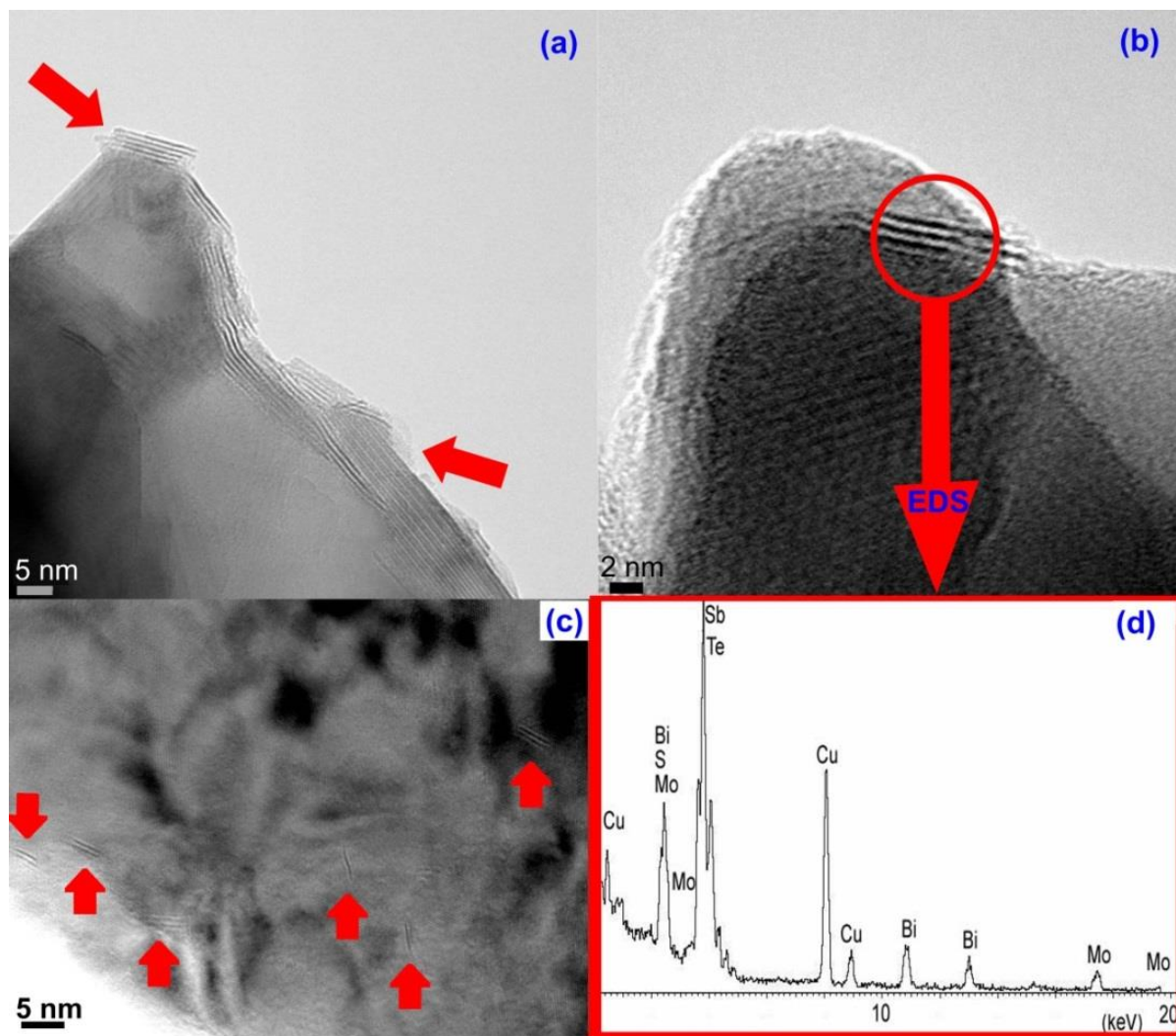


Figure 4.1: HRTEM images of (a) decorated grains of $(\text{Bi}_{0.2}\text{Sb}_{0.8})_2\text{Te}_3$ with nano-flakes of MoS_2 in extruded nanocomposite containing 0.8 wt.% MoS_2 , (b) MoS_2 nano-flake with few atomic layers decorating a grain in a extruded nanocomposite with 0.2 wt.% MoS_2 , (c) several MoS_2 nano-particles (indicated by arrows) dispersed in the matrix of an extruded nanocomposite with 0.4 wt.% MoS_2 and (d) EDX spectrum of indicated area in panel (b).

Figure 4.1(c) shows that MoS_2 nano-particles are dispersed throughout the matrix in the nanocomposites, as indicated by the arrows. EDX spectroscopy of areas containing these nano-particles confirmed the presence of Mo and S in nano-flakes of the extruded samples (Figure 4.1(d)). The intense Cu peaks originate from the copper grid used on the sample holder of the HRTEM. The powder particles are deposited on this Cu grid for observation.

SEM images taken with backscattered electrons of the conventional $(\text{Bi}_{0.2}\text{Sb}_{0.8})_2\text{Te}_3$ single phase alloy and of one of the nanocomposites of $(\text{Bi}_{0.2}\text{Sb}_{0.8})_2\text{Te}_3:\text{MoS}_2$ containing 0.4 wt.% MoS_2 are presented in Figure 4.2. The size of the grains in the single phase conventional alloy is in the few microns range, while the mean grain size in nanocomposites is less than 500 nm. We observed this grain size reduction in all nanocomposites, both *n*-type and *p*-type, containing different quantities of MoS_2 nano-particles. In these images, to better reveal the grain structure, the gray scales of the images were inverted using an image tool software. Consequently, darks spots which are pores mainly introduced or enlarged due to electrolytic etching, became white spots in these images.

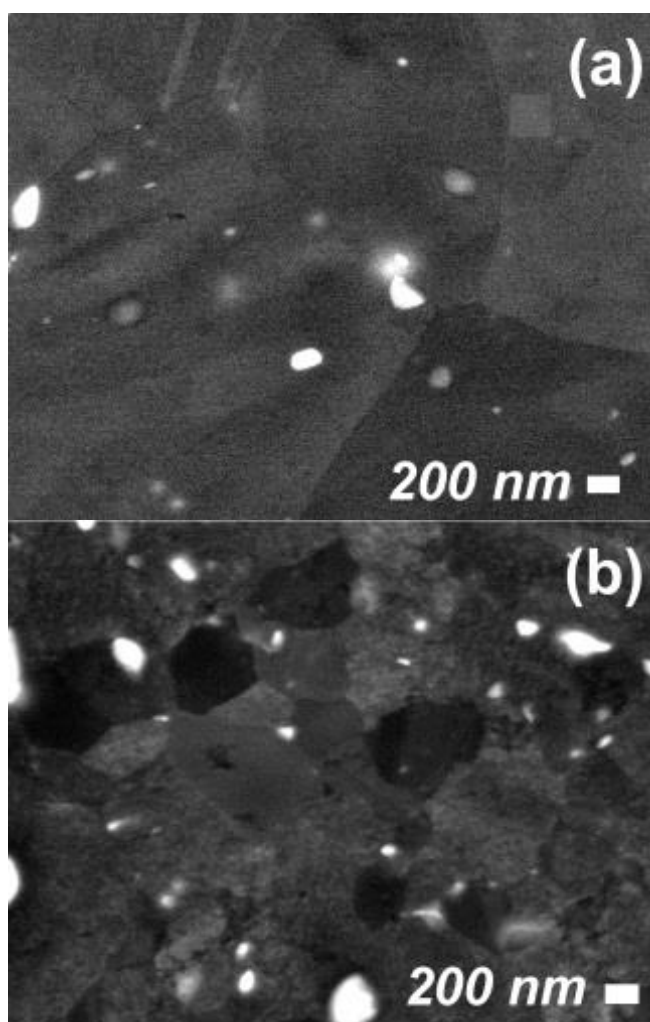


Figure 4.2: Backscattered electrons SEM images revealing: (a) the microstructure of a conventional single phase $(\text{Bi}_{0.2}\text{Sb}_{0.8})_2\text{Te}_3$ alloy (0 wt.% MoS_2), (b) the sub-micron matrix grains in $(\text{Bi}_{0.2}\text{Sb}_{0.8})_2\text{Te}_3:\text{MoS}_2$ nanocomposite containing 0.4 wt.% MoS_2 .

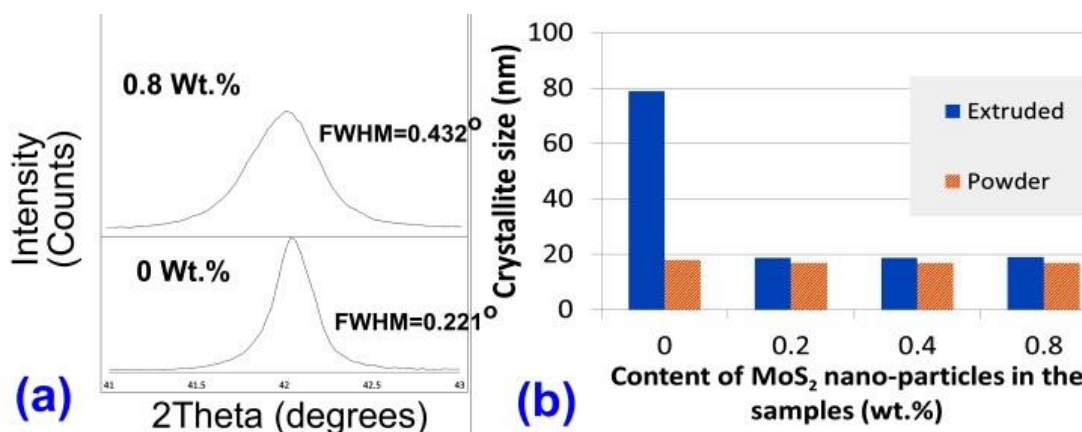


Figure 4.3: Peak broadening in nanocomposites (a) selected peaks corresponding to (110) plane, (b) crystallite sizes of the powders and extruded samples of conventional alloy and nanocomposites, as determined by Scherrer's formula.

XRD analyses of both nanocomposites and conventional single phase alloy indicate that the $(\text{Bi}_{0.2}\text{Sb}_{0.8})_2\text{Te}_3$ compound is the main phase observed in all *p*-type samples. The XRD results suggest that no chemical reaction takes place between $(\text{Bi}_{0.2}\text{Sb}_{0.8})_2\text{Te}_3$ and MoS_2 during the mixing and/or hot extrusion processes. However, peak broadening is observed in all the nanocomposite samples compared to the conventional alloy. Figure 4.3(a) highlights broadening in one of the peaks (corresponding to diffraction from the (1 1 0) plane) for the nanocomposite with 0.8 wt.% MoS_2 nanoparticles. These broadenings lead to sharp reduction of the calculated crystallite sizes, using Scherrer's formula, in all extruded nanocomposites compared to the extruded conventional alloy. Figure 4.3(b) shows that after the hot extrusion process the average crystallite size in composites increased only 10% compared to the nearly 400% growth observed in the single phase bismuth telluride based alloy. The XRD observations confirm TEM analyses of no apparent interatomic diffusion of Mo or S in the matrix, and strongly suggest that mechanical alloying and hot extrusion do not break the Mo-S bonds, while (perhaps) slightly reforming the nano-particles shape.

We suggest two mechanisms of grain growth suppression in these novel TE nanocomposites. First, the observed inter-dispersed MoS_2 nano-flakes covering the outer surface of the matrix grains form a localized barrier to migration of matrix atoms. These barriers will lead to less atom diffusivity at grain boundaries and result in negligible grain growth. Second, the addition of

MoS₂ nano-particles, which is a well-known solid state lubricant [136], facilitates the extrusion process by reducing the heat generated by plastic deformation. Consequently, materials containing MoS₂ nano-particles in the extrusion die were exposed to lower effective temperatures. Therefore, matrix grains recrystallization and growth is strongly inhibited compared to the conventional alloy.

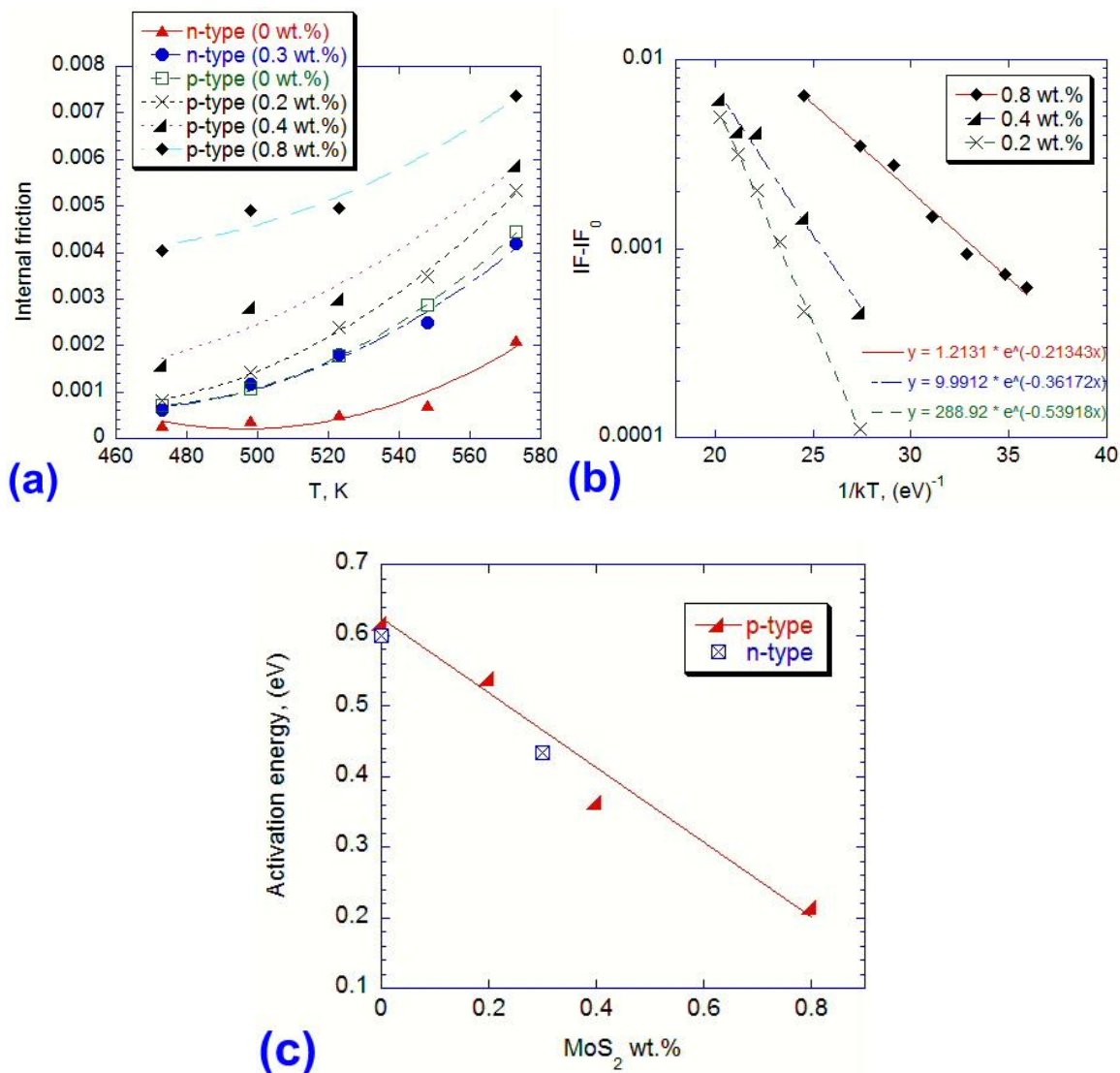


Figure 4.4: (a) Measurements of the internal friction of nanocomposites with different amount of MoS₂ nano-particles compared with conventional alloys, as a function of absolute temperature; (b) Arrhenius plot of p-type nanocomposites, and (c) illustration of the internal friction activation energy trend as a function of MoS₂ content.

The significant structural changes in extruded TE material when MoS₂ nano-inclusions were introduced can also be characterized by MS. Compared to extremely localized characterization techniques, such as HRTEM, MS presents the complementary advantage of measuring properties averaged over the entire extruded rods. The internal friction (IF), is a dimensionless quantity related to the mechanical energy dissipation mechanisms and is expected to be altered by structural changes and its associated defects [160, 183]. We investigated IF in the temperature interval from 300 to 573 K for both *p*- and *n*-type nanocomposites as well as conventional TE alloys. If we consider the IF for temperatures above 470 K we observe an important increase for all samples with MoS₂ nano-inclusions, as it can be seen in Figure 4.4(a). From this figure we also observe an increase of IF with temperature, an activated process from which we can obtain activation energies. Figure 4.4(b) shows a progressive decrease in the activation energy of IF for samples with increasing amount of MoS₂.

The exponential increase of internal friction with temperature can usually be attributed to viscous plastic deformation in the material. The value of this featureless IF background (IF_{bg}), also known as damping background, is highly structure-sensitive. It is known to increase in polycrystalline materials when the grain size decreases or when there is accumulated material deformation [183]. It is clear that the increase of IF_{bg} by the addition of MoS₂ nano-particles in our nanocomposites is consistent with the observed reduction of crystallite size by XRD, as with most nanostructured materials, which are known as high damping materials [183]. Our XRD results show that the crystallite sizes in the nanocomposites, although significantly smaller when compared to the conventional alloy, are almost independent of the MoS₂ concentration (see Figure 4.3(b)). Therefore, the measured increase in IF_{bg} and the trend observed in the reduction of the activation energy is an indication that crystal defects largely contribute to the IF_{bg} [160, 183]. As we have shown earlier, adding nano-inclusions led to grain size reduction or, equivalently, a higher density of grain boundaries in the nanocomposites in contrast to the conventional alloys. Moreover, the total area of interfaces between nano-particles of MoS₂ and the matrix, which are other sources of crystal defects in the material, also increase with the addition of MoS₂. Differences in the lattice parameters of the matrix and nano-inclusions lead to incoherent interfaces between the two phases, giving rise to localized strain at these interfaces [184]. Thus, it is not surprising that IF_{bg} intensifies since increasing MoS₂ will increase the strained regions at incoherent interfaces in the material [185, 186]. As pressure (sonic) waves

propagate in these nanocomposites, creep relaxation becomes easier (its activation energy is reduced) as we incorporate more interfaces.

The presence of distributed nano-particles of MoS₂ in nanocomposites expectedly influences the electrical and heat transport properties of the TE nanocomposite alloys. For a sample with 0.4 wt.% of MoS₂ nano-inclusions, at temperatures above 450 K, the thermal conductivity is reduced by about 20% compared to the thermal conductivity of the conventional alloy (e.g. at 450 K, $\lambda_{comp.}=1.4$ W/m·K and $\lambda_{conv.}= 1.8$ W/m·K). We have also observed a higher electrical resistivity in composite samples resulting in an approximately 10% decrease in ZT at room temperature compared to that of the conventional (Bi_{0.2}Sb_{0.8})₂Te₃ alloy. However, there is a marked difference in the ZT temperature dependence, where the nanocomposite increases in performance and surpasses the conventional alloy at higher temperatures. For instance, at a temperature of 370 K, the ZT value of a sample with 0.4 wt% MoS₂ reaches 0.93, an increase of 8% with respect to that of the conventional alloy.

4.5 Conclusion

In summary, p -type (Bi_{0.2}Sb_{0.8})₂Te₃:MoS₂ nanocomposites with enhanced figure of merit at temperatures higher than 370K were obtained through mechanical alloying and hot extrusion. The microstructure of the nanocomposites exhibited reduced grain sizes of these materials compared to conventional (Bi_{0.2}Sb_{0.8})₂Te₃ alloy. XRD analyses also show crystallite size reduction in the nanocomposites, which increases scattering of mid- and long-wavelength phonons. Important reductions in thermal conductivities of the nanocomposites were observed. MS investigations show a systematic increase of IF by adding MoS₂ nano-inclusions, which confirm microstructural changes in the nanocomposites. One n -type nanocomposite with 0.3 wt.% MoS₂ was also produced to confirm the feasibility as well as the similarity of the structural changes of both p - and n -type nanocomposites by MoS₂ nano-particle addition. This work shows that nanocomposites with MoS₂ nano-inclusions offer a novel alternative to increase the TE performance of bulk bismuth telluride based alloys.

4.6 Further discussion

The calculated lattice parameters of molybdenum disulfide $a=3.15\text{\AA}$, $b=3.15\text{\AA}$, and $c=12.30\text{\AA}$ in comparison with the lattice parameters of the matrix alloy, $(\text{Bi}_{0.2}\text{Sb}_{0.8})_2\text{Te}_3$, $a=4.33\text{\AA}$, $b=4.33\text{\AA}$, and $c=30.28\text{\AA}$ show large lattice mismatches at the interfaces between MoS_2 nano-particles and the matrix. The nano-inclusions with the size and distribution as it appeared in the produced nanocomposites are expected to effectively scatter both medium- and long-wavelength phonons [187]. In the meantime, the local disordered regions of interfaces between nano-particles and matrix contribute to the scattering of shorter wavelength phonons.

It is known that microstructure besides inclusion size and dispersion of inclusions affect the physical properties of semiconductors [3, 188-190].

By introducing the nano-particles in a semiconductor matrix, due to different lattice mismatches to relevant semiconductors, some strain states appear. Depending on type of stress (i.e. tensile or compressive) caused by the nano-particles which leads to some strain in the structure of the matrix, shifting in the position of the Fermi level within the semiconductor's band is expected [191, 192].

In general, engineering the microstructure of materials leads to better performance of materials. In the case of nano-inclusions embedded semiconductors, one can predict that by controlling the atomic structure and microstructure of the matrix particularly at the interface of nano-inclusions and the matrix, electrical and thermal properties of the bulk can be modified. Nano-inclusions can be embedded inside the grains or at the grain boundaries while by increasing the quantity of nano-inclusions the possibility of agglomeration of nano-particles at grain boundaries increases, which leads to more restricted mobility of charge carriers or augmentation of charge carrier concentration in the grain.

In our study, all observed nano-inclusions in the nanocomposites are detected at the grain boundaries. A few agglomerations of nano-particles at grain boundaries observed in the nanocomposite with maximum amount of MoS_2 nano-particles (0.8 wt.%) as illustrated in Figure 4.1(a). However, there is no sign of agglomeration in nanocomposites containing less MoS_2 . Hence, we do not expect charge carrier mobility restriction in the nanocomposites due to the nano-particles agglomeration.

Chapter 5

ARTICLE 3: EFFECT OF SUPPRESSION OF GRAIN GROWTH OF HOT EXTRUDED $(\text{Bi}_{0.2}\text{Sb}_{0.8})_2\text{Te}_3$ THERMOELECTRIC ALLOYS BY MoS_2 NANOPARTICLES

Mohsen K. Keshavarz¹, Dimitri Vasilevskiy¹, Remo A. Masut¹, Sylvain Turenne¹

¹École Polytechnique de Montréal, C.P. 6079, Succ. Centre-Ville, Montréal (Québec), H3C 3A7, Canada

This article published in the Journal of Electronic Materials, Available online since February, 2014, DOI: [10.1007/s11664-014-3019-3](https://doi.org/10.1007/s11664-014-3019-3), “The final publication is available at link.springer.com”.

Foreword

In this chapter we report investigation of TE properties of produced bismuth telluride based nanocomposites. The effect of nano-particle addition up on Young's modulus of the nanocomposites is also studied.

It is mentioned in the previous chapters that nano-inclusions affect not only the microstructure of the TE materials but also their electronic and thermal properties. The interest of making such nanocomposites stems from idea of significant thermal conductivity reduction by adding nano-inclusions. We tried to satisfy this interest by implementation of synthesis method with ease of manipulation and possibility of mass production.

In this chapter, besides presenting Manuscript 3, supplementary characterization results of *n*-type nanocomposite are presented, which confirms the feasibility of using the same procedure to make *n*-type nanocomposites with similar behavior as *p*-type nanocomposites which have been studied.

5.1 Abstract

Nanostructured bulk materials are presently considered as one of the most promising venues to enhance performance of thermoelectric (TE) materials and devices. Powder metallurgy offers the distinctive advantage, compared to conventional synthesis, that it can start directly from nano-sized particles. However, further processing such as extrusion usually requires elevated temperatures leading to grain growth. We have found that the introduction of molybdenum disulfide (MoS_2) semiconductor nano-particles, a well-known solid lubricant, suppresses grain growth in bismuth telluride based alloys, thus improving the extrusion process. Scanning electron microscope images show that introducing MoS_2 particles with concentrations of 0.2, 0.4 and 0.8 wt% in *p*-type $(\text{Bi}_{0.2}\text{Sb}_{0.8})_2\text{Te}_3$, under otherwise identical extrusion conditions, reduces the average grain size by a factor of four. Scherer's formula applied to x-ray diffraction data indicates that average crystallite sizes in powders (~ 17 nm) are not significantly different from those of alloys extruded with MoS_2 (~ 18 nm), which is in stark contrast with those in the conventional alloy $(\text{Bi}_{0.2}\text{Sb}_{0.8})_2\text{Te}_3$, extruded under the same conditions (~ 80 nm). Harman measurements of TE properties show a decrease of the thermal conductivity, accompanied by a reduction of the room temperature figure of merit (ZT values) from 0.9 to 0.7 due to a lower power factor. However, once above 370 K, the performance of alloys containing MoS_2 surpasses that of $(\text{Bi}_{0.2}\text{Sb}_{0.8})_2\text{Te}_3$, with a reduction of the thermal conductivity which is more significant at temperatures above the cross point of the ZT values.

5.2 Introduction

The increased application of thermoelectric (TE) materials in energy conversion devices used for power generation and refrigeration depends on a substantial increase of their mechanical and TE performance [19, 21, 176, 193, 194]. The material TE performance is characterized by its dimensionless figure of merit $ZT = \sigma\alpha^2T/\lambda$, where the Seebeck coefficient (α), the electrical conductivity (σ) and the thermal conductivity (λ) are three interdependent properties, which depend on the absolute temperature (T) [1].

Bi_2Te_3 -based alloys have been studied for decades and are considered as the TE materials with highest performance for applications near room temperature [1, 164, 195] and it has been

suggested that nanostructuring bulk alloys may offer the desired substantial increase of TE performance.

During the past decade, several studies have proposed nanostructures as efficient scatterers of long and mid-wavelength phonons without significantly changing the charge carrier mobility and consequently enhance ZT mainly by reducing the lattice thermal conductivity [96, 104, 105, 169, 196].

One of the approaches to reduce lattice thermal conductivity is the use of composites structures and the main reason is the introduction of more phonon scattering centers, hopefully without an important decrease of the power factor ($\sigma\alpha^2$). In the proposed composites phonon scattering centers were increased by adding nano-inclusions, or mixing particles of a nanostructured phase or of dissimilar phases seeking to increase the density of interfaces in the material [40-43, 104]. Several types of nano-inclusions such as semimetals, semiconductors, metals, ceramics and even carbon nanotubes and fullerenes have been introduced in a variety of TE materials [40, 41, 46, 179, 180]. For example, nanocomposites of Bi-Sb-Te/ C_{60} (fullerene) have been recently produced by mechanical alloying of nano-powders of Bi-Sb-Te with C_{60} in a planetary mill followed by hot pressing where Bi-Sb-Te nano-crystals covered by C_{60} resulted in crystallite size and thermal conductivity reduction [180].

In this work we introduce nano-particles of molybdenum disulfide as a secondary phase in bismuth telluride-based nanocomposites. Molybdenum disulfide (MoS_2) is a member of the transition-metal dichalcogenide family, built up of weakly bonded S-Mo-S layers. Each Mo atomic plane in MoS_2 is sandwiched between two S atomic planes, with strongly covalent bonds between Mo and S. The weak van der Waals (vdW) interaction between the sheets of sulfide atoms of adjacent S-Mo-S layers allows easy interlayer sliding, which causes a low coefficient of friction in MoS_2 , and renders it a valuable solid lubricant. Due to the weakness of these vdW bonds between interlayers of MoS_2 and the strong covalent intralayer bonds, the formation of nano-particles containing only a few MoS_2 layers is possible by mechanical approaches [136, 197, 198]. Previous study shows that nano-particles of MoS_2 behave as semiconductors [136]. In addition, a low thermal conductivity of MoS_2 film has been reported, in the order of 0.1-1 W/mK [197].

We use mechanical alloying (MA) to synthesize the matrix of the nanocomposites in the form of powders, and then disperse nano-particles of MoS₂ in order to suppress grain growth during the subsequent hot extrusion process. We will show that a few MoS₂ layers will act as barriers at grain intersections. In doing so, we obtain smaller grains and crystallites (i.e. more interfaces) as well as dispersed nano-inclusions, resulting in increased phonon scattering. We present details of the microstructure, nanostructure and TE properties of these nanocomposites. We show that MoS₂ nano-inclusions are very effective to suppress grain growth and bring about a reduced thermal conductivity of the nanocomposites compared to the conventional (Bi_{0.2}Sb_{0.8})₂Te₃ alloys.

5.3 Experimental procedure

High purity (99.999%) shots of Bi, Sb and Te were proportionally weighed to obtain a (Bi_{0.2}Sb_{0.8})₂Te₃ compound, mixed and then mechanically alloyed in an attritor. In addition, we used Sb in quantities of 0.09 - 0.18 wt.% of the total mix as a *p*-type dopant. Pure (99.99%) nano-particles of molybdenum disulfide (MoS₂) with a nominal particle size smaller than 90 nm (supplied by MKnano, Divn. of M K Impex Corp.) were added to the synthesized (Bi_{0.2}Sb_{0.8})₂Te₃ compound powder in an attrition tank and mixed for 1 - 4 hours. The concentration of MoS₂ in the mixed powder varied in the range of zero (conventional single phase alloy) to 0.8 wt.%. The mixed powders were then subjected to hot extrusion carried out at temperatures in a range from 380°C to 460°C. All the steps were performed under Ar atmosphere to avoid oxidation. A similar material processing was also followed to produce one nanocomposite of *n*-type (Bi_{0.95}Sb_{0.05})₂(Te_{0.95}Se_{0.05})₃ alloy containing 0.3 wt.% MoS₂ nano-particles.

X-ray diffraction measurements of these samples were carried out with a Philips X'Pert instrument. The mean crystallite size of the bulk nanocomposites was calculated using Scherrer's equation. The nanostructure was analyzed using a Jeol JEM-2100F high-resolution transmission electron microscope (HRTEM). We also used energy dispersive X-ray spectroscopy (EDX) in the HRTEM for elemental analysis of our specimens. Converged beam with the minimum size of 4 nm on top of the specimen was used for EDX analysis. Powdered samples for HRTEM were obtained as a byproduct of sawing extruded specimens with a diamond blade saw. The microstructure of nanocomposites was assessed by high resolution scanning electron microscope (SEM) observations with a Jeol JSM-7600 TFE.

The elastic properties of TE materials play a key role in the simulations of the thermo-mechanical stress which appears in cooling or generator TE modules[199]. Young's modulus of each of the extruded rods (25.4 mm diameter) was calculated by measuring the density and the frequency of the excited longitudinal fundamental oscillations of 120 mm long samples using the mechanical spectroscopy setup described in Ref.[200], in the temperature range from 293 to 573 K.

The TE properties of the extruded materials such as σ , S and λ and the figure of merit ZT of nanocomposites were studied using a Harman setup in the temperature range 290 to 480 K. Cubical samples of 5 mm edges with Ni plated contacts on two opposite faces were used for Harman tests.

5.4 Results

5.4.1 Microstructure and mechanical properties analyses

Figure 5.1a-d present typical images of fracture surfaces perpendicular to the extrusion axis. They clearly show the morphological evolution from the conventional single phase $(\text{Bi}_{0.2}\text{Sb}_{0.8})_2\text{Te}_3$ alloy to the nanocomposites of $(\text{Bi}_{0.2}\text{Sb}_{0.8})_2\text{Te}_3/\text{MoS}_2$ containing increasing quantities of the nano-inclusions.

SEM images in Figure 5.1 unambiguously show that the mean size of the $(\text{Bi}_{0.2}\text{Sb}_{0.8})_2\text{Te}_3$ matrix grains in the nanocomposites gradually decreases with increasing MoS_2 content. Image tools software was used for the evaluation of the mean grain sizes of conventional alloy and nanocomposites with 0.8 wt.% MoS_2 . Results show a grain size reduction in nanocomposites by a factor of nearly four.

Although no specific details will be reported here, it is important to note that a similar reduction of grain size was also found for the nanocomposite of *n*-type $(\text{Bi}_{0.95}\text{Sb}_{0.05})_2(\text{Te}_{0.95}\text{Se}_{0.05})_3$ with 0.3 wt.% MoS_2 .

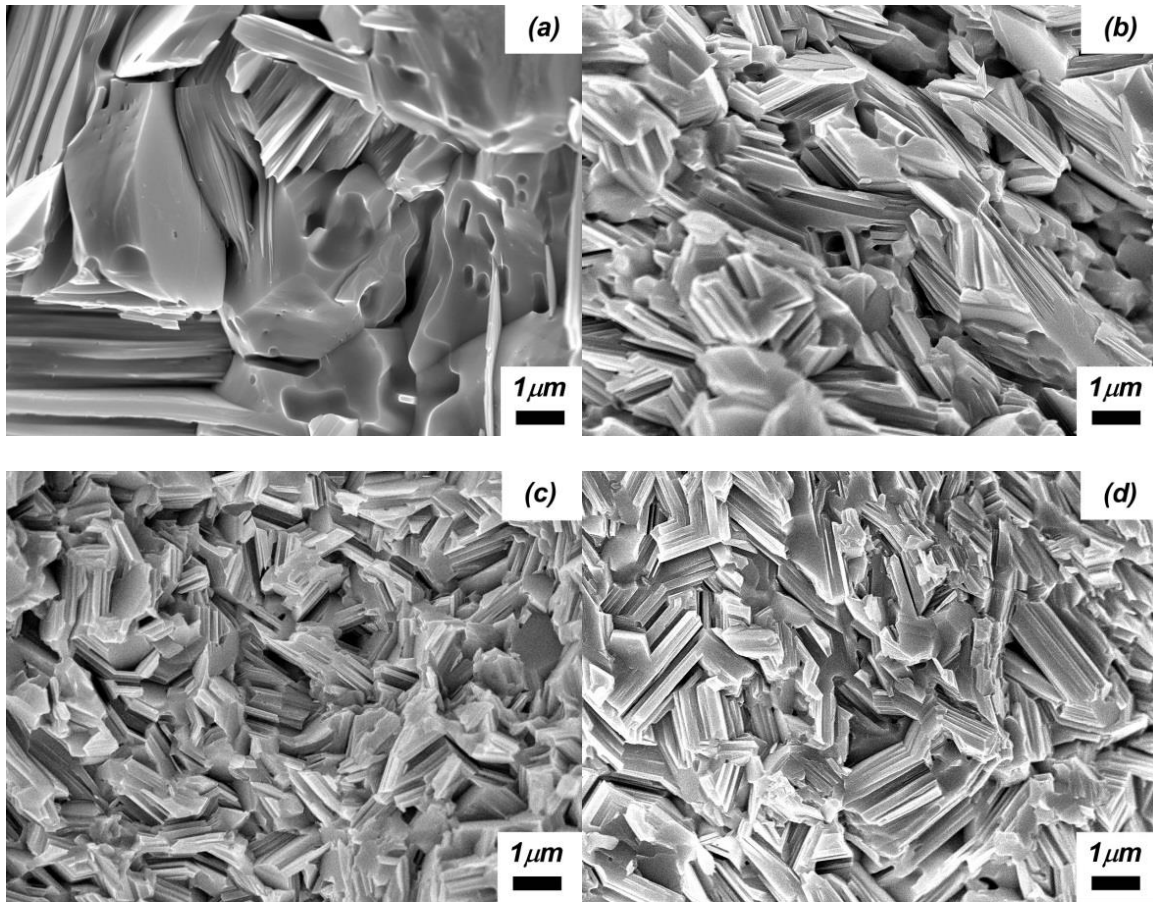


Figure 5.1: SEM images of the fracture surfaces perpendicular to the extrusion axis of a) conventional $(\text{Bi}_{0.2}\text{Sb}_{0.8})_2\text{Te}_3$ alloy (0 wt.% MoS_2), and nanocomposites with b) 0.2 c) 0.4 d) 0.8 wt.% MoS_2 .

Figure 5.2 illustrates the measured, approximately linear, reduction of Young's modulus E when the temperature increases from 293 to 573 K for all samples with different content of MoS_2 . Figure 5.2 also shows the gradual increase in the value of Young's modulus with the MoS_2 content in the nanocomposite. The alloy with 0.8 wt.% of MoS_2 nano-inclusions shows a 12 % increase in E compared to the conventional alloy.

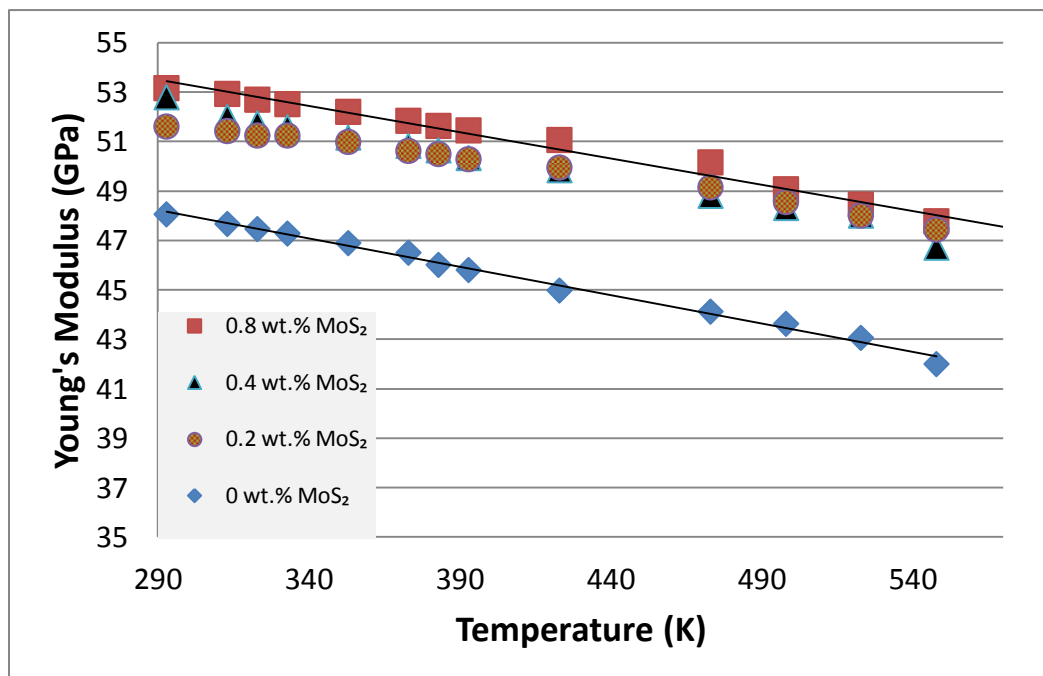


Figure 5.2: Young's modulus measured by mechanical spectroscopy as a function of temperature and MoS₂ content.

5.4.2 XRD analysis

The mixture powders and bulk extruded samples of both the nanocomposites as well as the conventional single phase alloy were characterized by x-ray diffraction to analyze their phase composition. The results indicate that the phase of $(\text{Bi}_{0.2}\text{Sb}_{0.8})_2\text{Te}_3$ is present in all specimens. There is no sign of peaks shifting in the nanocomposite samples compared to the conventional alloy, thus confirming that no chemical reaction takes place between $(\text{Bi}_{0.2}\text{Sb}_{0.8})_2\text{Te}_3$ and MoS₂ during mixing and/or hot extrusion processes (Figure 5.3a). We could not identify any peak representing the MoS₂ phase probably given the very small quantities of MoS₂ nanoparticles in the samples. XRD analysis show significantly larger peaks' broadening in the extruded nanocomposites compared to the conventional single-phase material (Figure 5.3b), which is a consequence of smaller crystallite sizes in nanocomposites. The peak broadenings have been used to calculate crystallite sizes using Scherrer's formula.

Figure 5.4 shows the crystallite size of both powders and hot extruded bulk nanocomposites compared to $(\text{Bi}_{0.2}\text{Sb}_{0.8})_2\text{Te}_3$. Clearly, except for conventional $(\text{Bi}_{0.2}\text{Sb}_{0.8})_2\text{Te}_3$, no significant growth of crystallites is observed during hot extrusion.

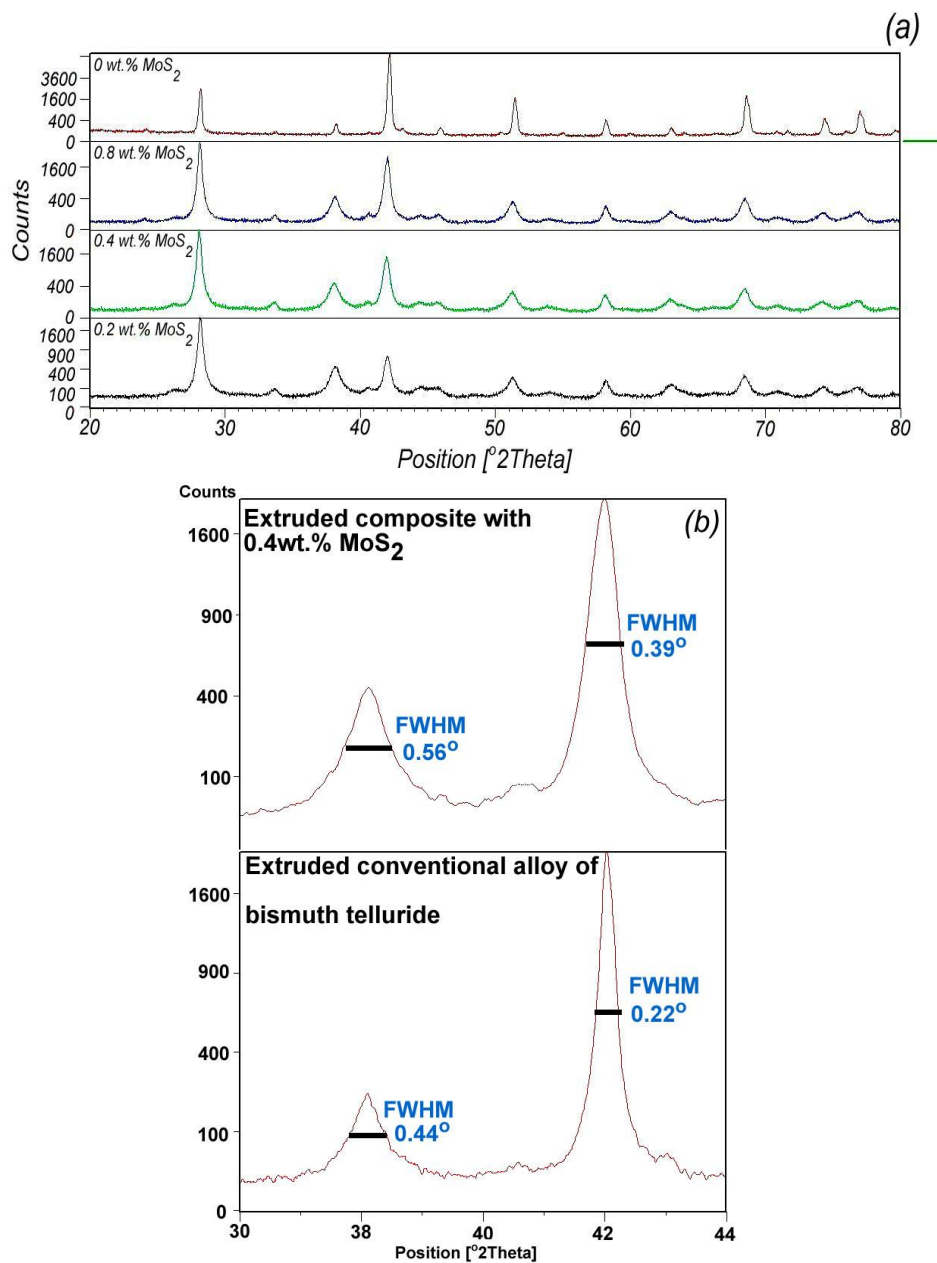


Figure 5.3: (a) X-ray diffraction patterns of extruded samples with different amount of MoS₂ nanoparticles, (b) Peaks' broadening in nanocomposites compared to the alloy without MoS₂.

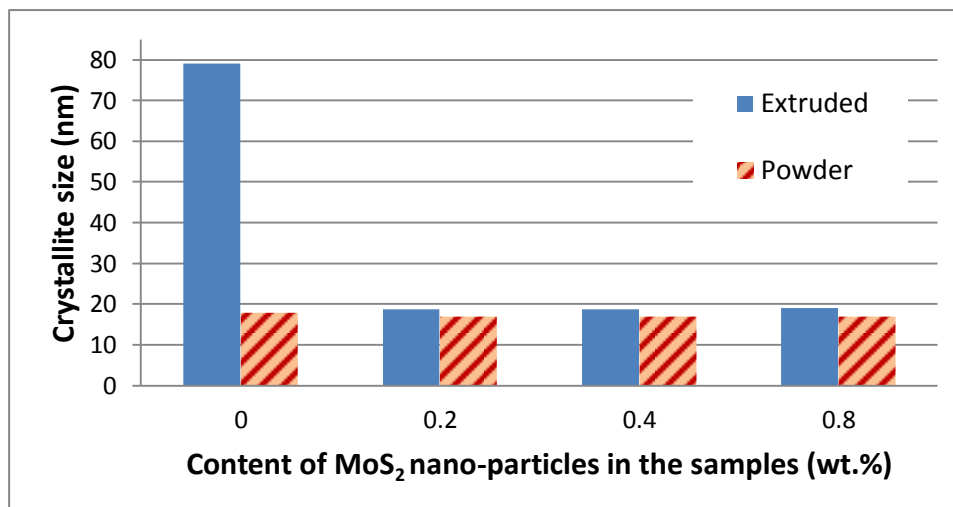


Figure 5.4: Crystallite sizes of the powders and extruded samples of conventional alloy and nanocomposites calculated from XRD peak broadening using Scherrer's formula.

5.4.3 TEM observations

Figure 5.5a and b are high resolution TEM images of the extruded nanocomposite with 0.4 wt.% MoS₂. In Figure 5.5a, the dispersion of decorated grains of (Bi_{0.2}Sb_{0.8})₂Te₃ with a few layers of MoS₂ in the form of nano-flakes is illustrated. We observe MoS₂ nano-flakes, a few atomic layers thick, covering particles of (Bi_{0.2}Sb_{0.8})₂Te₃ in the powder samples and later those few layers are present in the extruded samples. Thus, the TEM images confirm that MoS₂ particles after mixing and during hot extrusion break down into nano-flakes containing a few atomic layers. The observed distances between the dark layers in the HRTEM images is roughly 0.63 nm, which compares well with the reported inter-planar Mo distance in MoS₂ of 0.62 nm. To identify MoS₂ nano-flakes we selected three distinctive areas on the image (Figure 5.5b) and analyzed them with EDX spectroscopy. Figure 5.5c illustrates EDX spectra of these three positions, which confirm presence of pure MoS₂ nano-flakes in the extruded sample. In position 2, there are two grains with two different compositions and its spectrum shows elements of both phases. EDX spectrum of position 3 indicates a MoS₂ free zone. These fragments of MoS₂ are dispersed in the material separated by distances in the order of few tens of nanometers.

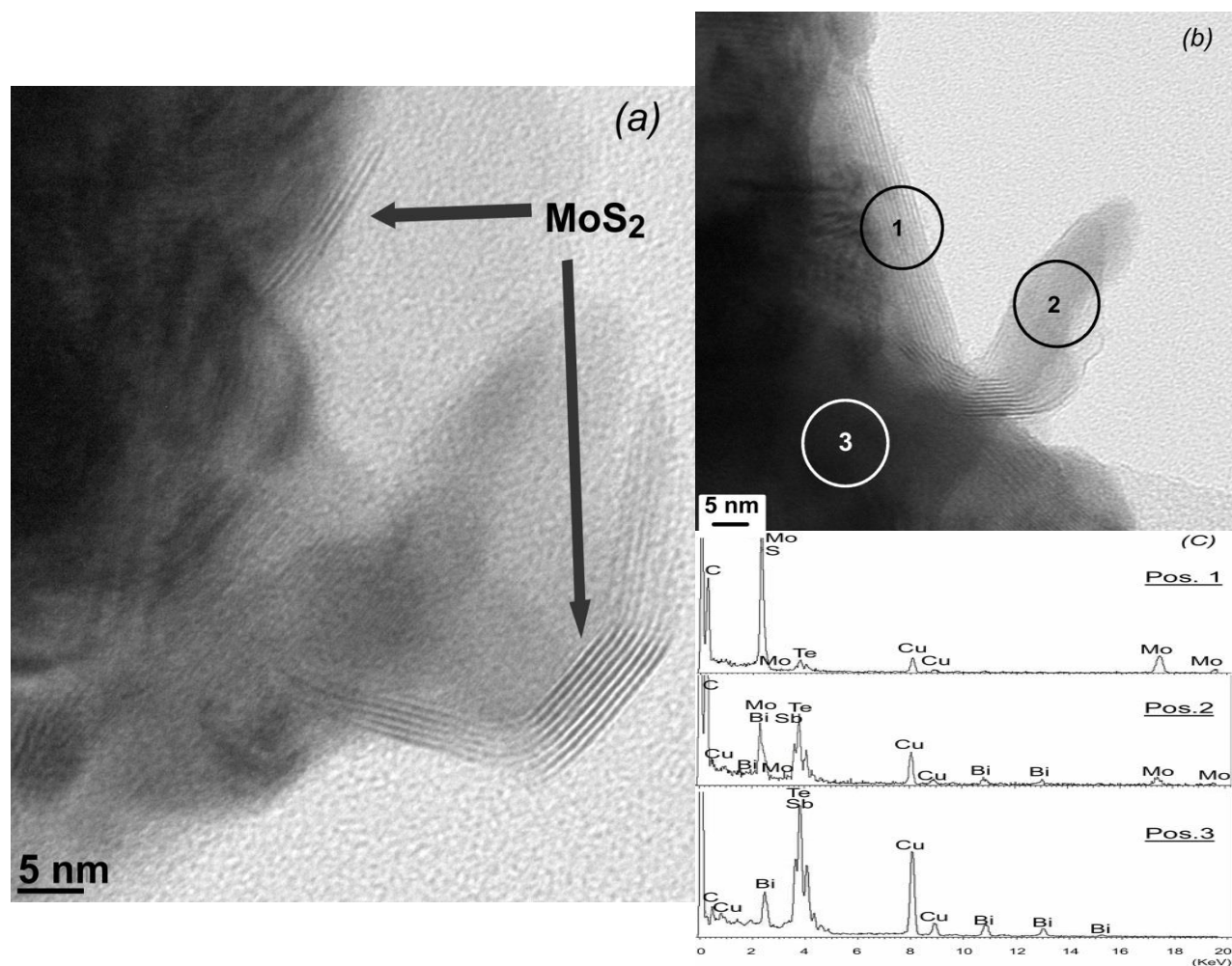


Figure 5.5: TEM images of (a) dispersed nano-flakes which decorate the matrix grains in extruded nanocomposite with 0.4 wt.% of MoS₂, (b) extruded nanocomposite with 0.4 wt.% MoS₂ and (c) EDX spectra of positions labeled 1-3 in panel (b).

5.4.4 Thermoelectric properties

Since MoS₂ flakes are found at close distances in thermoelectric alloys and their size is in the nanometer range, it is natural to expect their influence on the electrical and heat transport properties. The TE properties of the alloy with 0.4 wt.% of MoS₂ are presented in Figures 5.6 and 5.7 as functions of absolute temperature, and compared to the conventional (Bi_{0.2}Sb_{0.8})₂Te₃ compound. Samples with this specific MoS₂ concentration have been chosen for analysis because

more data is available from several extrusions with different processing parameters, as indicated in each figure legend.

Figure 5.6(a) shows a factor of about two decrease of the electrical conductivity for 0.4 wt.% MoS₂ sample with nominal (0.09 wt.% addition of Sb) *p*-type doping (compare solid circles with solid rhomboids). Increasing the dopant level to 0.18 wt.% (Figure 5.6(a), solid squares) restores the electrical conductivity to the conventional alloy level. We also observed that the electrical conductivity is further increased (see solid triangles guided with a solid line) when powders with MoS₂ additives were milled for 4 hours.

Figure 5.6(b) shows a decrease of the thermal conductivity for alloys containing MoS₂ regardless of their doping level and processing parameters. A larger decrease is observed as the temperature increases. It is important to notice that the thermal conductivity near room temperature, in a range where there are no bipolar phenomena, is lower for the composite materials even when their measured electrical conductivities are equal or higher to that of the conventional single-phase alloy.

Despite the decrease in the thermal conductivity, the dimensionless figure of merit *ZT*-curves in Figure.5.7(a) show a decrease in room temperature performance of nanocomposites compared to the conventional alloy. However, at temperatures above 350 K, *ZT* values of samples with MoS₂ additives become higher than those of the conventional alloy. Seebeck coefficient (α) measurements show (see Figure 5.7(b)) room temperature values comparable to the conventional alloy only for the nanocomposite sample with the same nominal doping level. The Seebeck coefficient is lower for the composites with higher *p*-type doping yet revealing a tendency to outperform the conventional alloy at elevated temperatures (outside the measured range).

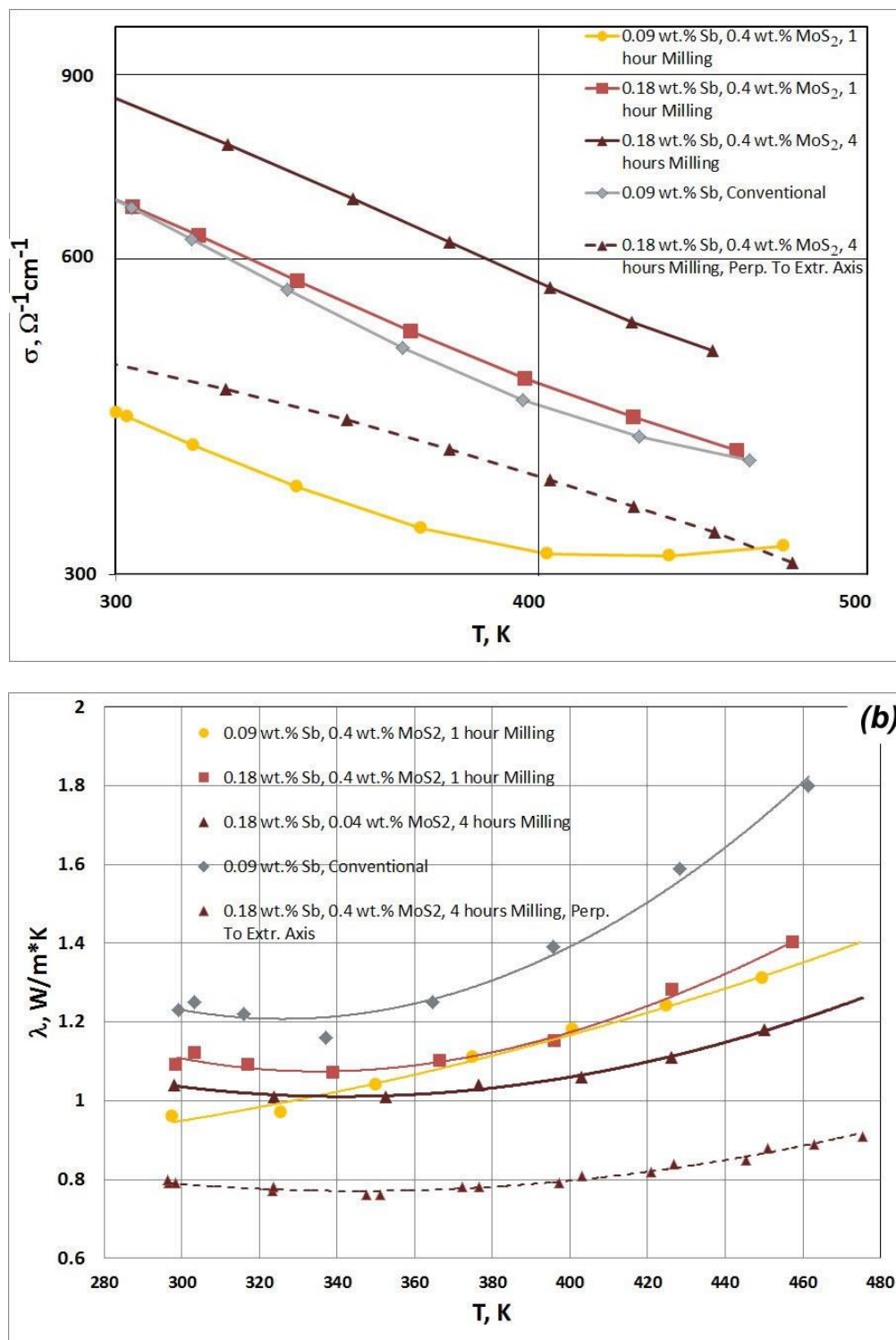


Figure 5.6: (a) Electrical conductivity (log-log scale) and (b) thermal conductivity of *p*-doped samples as a function of temperature. Both conductivities are measured on a plane containing the extrusion axes (except for the case of one sample, measured perpendicular to the extrusion axis, represented by solid triangles guided by a dashed line).

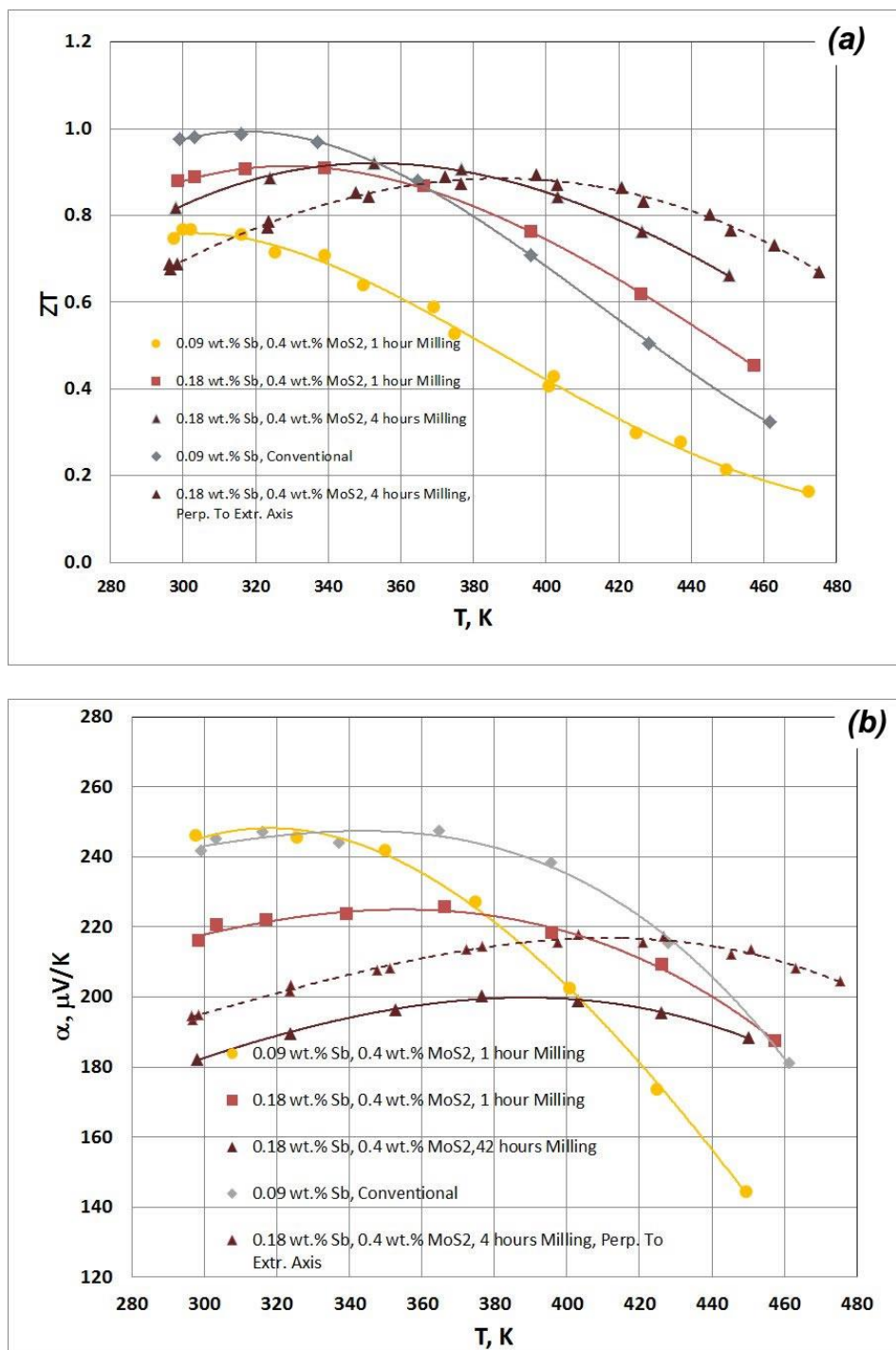


Figure 5.7: (a) Comparison of ZT values as a function of temperature of the conventional $(\text{Bi}_{0.2}\text{Sb}_{0.8})_2\text{Te}_3$ compound with samples containing 0.4 wt.% MoS_2 obtained with different processing parameters, (b) comparison of the Seebeck coefficient of samples in panel (a). As in the previous figure, one of the samples is measured in a direction along the extrusion axis (solid triangles guided by a dashed line).

Nanocomposite samples also show interesting TE properties in the direction perpendicular to the extrusion axis. Dashed curves in Figures 5.6 and 5.7 present such results measured on a 0.18 wt% Sb doped sample milled for 4 hours with 0.4 wt% of MoS₂. A significant reduction of electrical and thermal conductivities is observed in the direction orthogonal to the extrusion axis. This anisotropy is expected for bismuth telluride based alloys. However, the Seebeck coefficient measured in the direction orthogonal to the extrusion axis is higher than along the extrusion axis in the whole temperature range leading to the best ZT performance values above 370 K, as depicted in Figure 5.7(a). The increase of the Seebeck coefficient in the direction orthogonal to the extrusion axis signal changes of the scattering mechanisms for holes. The reduction in slope of the $\sigma(T)$ curve shown in Figure 5.6(a) may be an indication of an enhanced hole scattering cross section by the ionized impurities, which merits further research.

5.5 Discussion

The observed reduction of the grain size in nanocomposites is probably due to two factors. The first one consists in facilitating the extrusion process by the addition of MoS₂ nanoparticles, essentially as a lubricant [136]. At the same time, because of the weakness of the MoS₂ bonds, inclusions break down into nano-flakes only a few atomic layers thick during alloy synthesis in the attritor and under more severe plastic deformation during the hot extrusion. In our experiments, the extrusion rate in the samples containing MoS₂ nanoparticles was higher than in the conventional single phase alloy when all the other extrusion parameters were kept the same. Consequently, materials in the extrusion cylinder were exposed less time at high temperatures and grains had less time for recrystallization or growth.

The second reason for grain growth suppression is related to the observed MoS₂ nano-flakes on the outer surface of crystallites. The TEM observations confirm the presence of MoS₂ nano-flakes partially covering the matrix grains. The grain boundary motion (i.e. grain growth) is in general determined by the atoms diffusivity at grain boundary junctions. The presence of few layers of MoS₂ at the grain boundary alters the energy required for diffusion and grain boundary mobility and leads to a grain growth retarding action.

The reduction of the grain size in nanocomposites also leads to less porosity, which is indirectly confirmed by an important increase of Young's modulus with the minimum amount of MoS₂ particles.

XRD and EDX analyses show no sign of chemical reaction between MoS₂ and (Bi_{0.2}Sb_{0.8})₂Te₃ during mixing and hot extrusion. Crystallite sizes as calculated from XRD patterns are also much smaller than in the conventional alloy subjected to similar processing, implying a delay of the recrystallization in nanocomposites.

As it is expected, smaller grains and crystallites in nanocomposites affect the TE properties. In particular the decrease in the thermal conductivity of nanocomposites can be explained by the increase in phonon scattering due to the smaller crystallite sizes in nanocomposites as well as scattering at MoS₂ nano-inclusions.

5.6 Conclusion

Novel (Bi_{0.2}Sb_{0.8})₂Te₃ /MoS₂ nanocomposite TE alloys were synthesized and investigated, showing a tendency to increase TE performance at the higher end temperature range of bismuth telluride based alloys. MoS₂ nano-particles led to grain growth suppression and significantly smaller grain sizes were obtained compared to the conventional (Bi_{0.2}Sb_{0.8})₂Te₃ material subjected to similar MA and hot extrusion processes. MoS₂ nano-particles were observed dispersed in the material at distances of a few tens of nanometers and in the form of nano-flakes usually less than 10 atomic layers thick. The thermal conductivity of these nanocomposites is reduced due to smaller crystallites resulting in additional scattering of phonons. It is noteworthy to highlight that grain size reduction was observed in both *p*-type and *n*-type materials. Thus, nanocomposites with MoS₂ nano-inclusions provide a novel alternative to increase the mechanical and TE performance of bismuth telluride based alloys.

5.7 Characterization of *n*-type nanocomposite

One nanocomposite of *n*-type $(\text{Bi}_{0.95}\text{Sb}_{0.05})_2(\text{Te}_{0.95}\text{Se}_{0.05})_3$ alloy containing 0.3 wt.% MoS_2 nanoparticles was produced with a similar material processing procedure as the *p*-type nanocomposites. In this section more detailed results of characterization of this nanocomposite are presented.

5.7.1 Microstructure

Figure 5.8 illustrates fracture surfaces of *n*-type conventional single phase alloy and nanocomposite samples. They clearly show that adding MoS_2 nano-particles leads to grain size reduction in the nanocomposite. This result confirms the introduction of MoS_2 nano-particles produces a similar effect of on inhibition of matrix grain growth for *n*-type nanocomposite as for *p*-type ones.

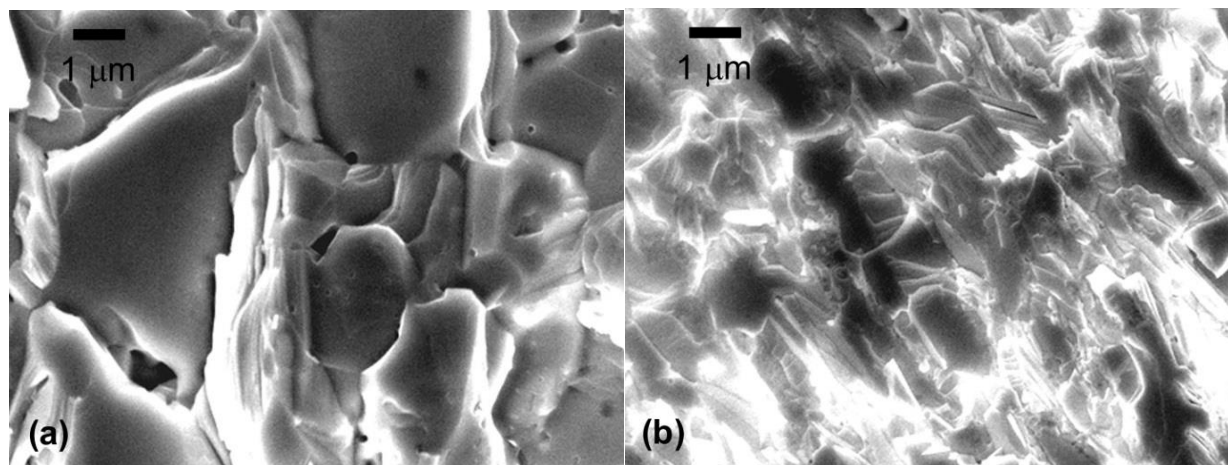


Figure 5.8: SEM images of the fracture surfaces perpendicular to the extrusion axis of a) *n*-type $(\text{Bi}_{0.95}\text{Sb}_{0.05})_2(\text{Te}_{0.95}\text{Se}_{0.05})_3$ alloy (0 wt.% MoS_2), and (b) *n*-type nanocomposite with 0.3 wt.% MoS_2 .

5.7.2 Thermoelectric properties

TE properties of *p*-type nanocomposites with several MoS_2 nano-inclusion concentrations were presented in section 5.4.4. We also expect to see an impact of MoS_2 nano-inclusion addition on TE properties of *n*-type nanocomposite. In this section, we present the TE properties of non-

optimized *n*-type nanocomposite of $(\text{Bi}_{0.95}\text{Sb}_{0.05})_2(\text{Te}_{0.95}\text{Se}_{0.05})_3$ with 0.3 wt.% MoS_2 nanoparticles.

Samples of the nanocomposite containing MoS_2 nano-inclusions showed lower electrical conductivity comparing to the conventional *n*-type alloy (see Figure 5.9). The observed anisotropy in the electrical conductivity is as expected for bismuth telluride based materials, and due to the texture imposed by extrusion process. Similar behavior was observed in the *p*-type nanocomposites with the same doping level as conventional alloy. However, in the *p*-type samples, we could compensate the electrical conductivity reduction due to nano-inclusion addition, by increasing the doping level.

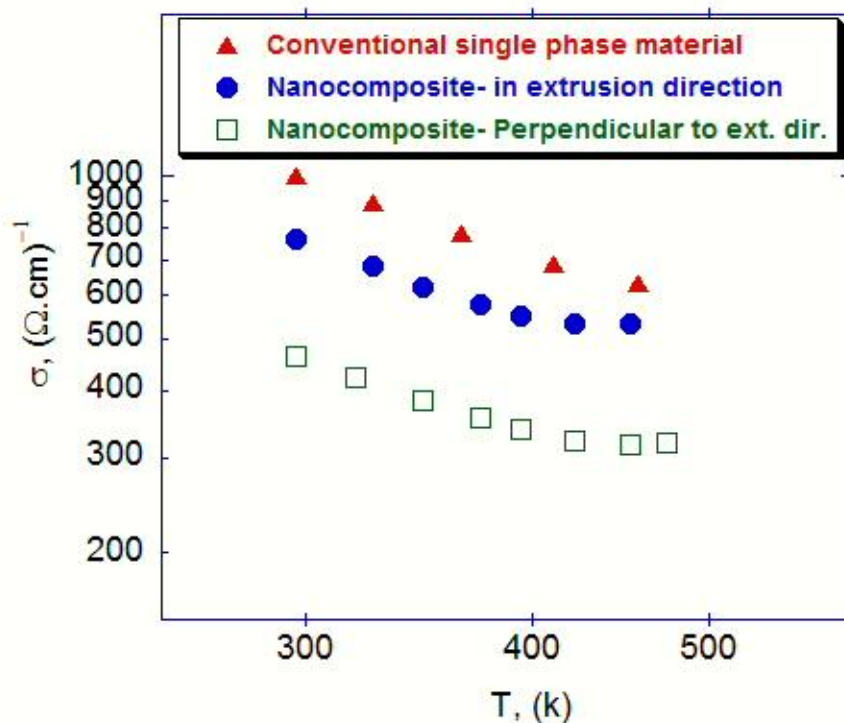


Figure 5.9: Electrical conductivity of *n*-type conventional and nanocomposite materials with 0.3 wt.% of MoS_2 as function of absolute temperature (log-log scale). The measured values in the direction parallel to the extrusion direction are presented for both conventional (red triangles) and nanocomposite (blue circles), as well as values measured on a plane perpendicular to the extrusion axis for the nanocomposite sample (blank squares).

Figure 5.10 shows the thermal conductivity of *n*-type conventional and nanocomposite samples. Although the microstructural analysis of the *n*-type nanocomposite indicated smaller grain size compared to the conventional alloy samples, there is no sign of thermal conductivity reduction in the nanocomposite specimens, contrary to expectation. However, due to the limited number of samples and insufficient comparable data, any further interpretation of this behavior seems inappropriate at this stage.

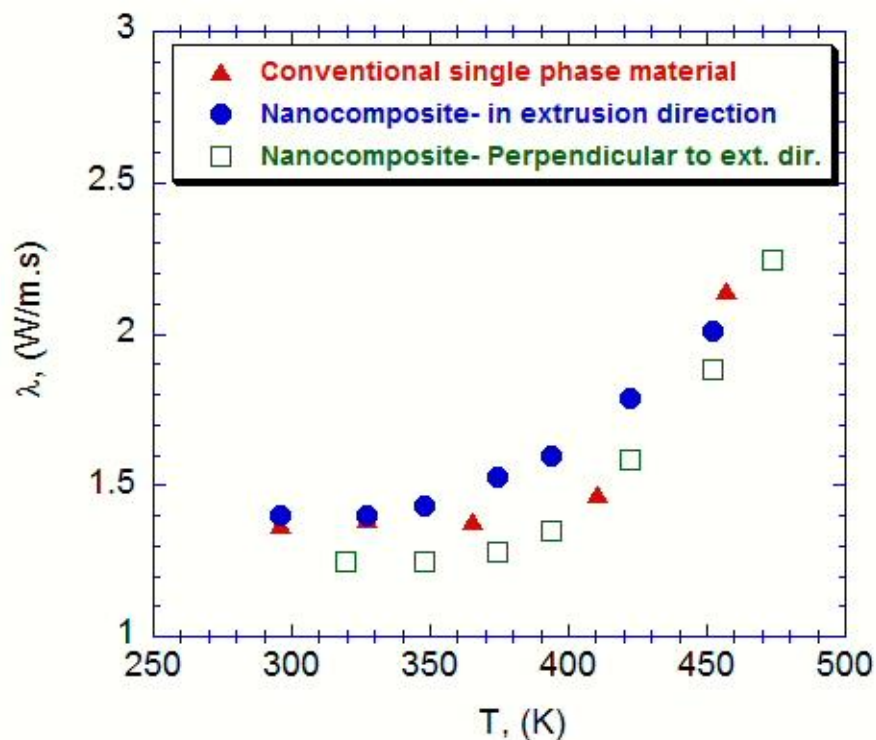


Figure 5.10: Thermal conductivity of *n*-type conventional and nanocomposite samples (with 0.3 wt.% MoS₂). The blank squares show the measured value for the nanocomposite sample along a direction perpendicular to the extrusion axis.

Despite a considerable decrease in the electrical conductivity, and no significant changes in thermal conductivity of *n*-type nanocomposite material comparing with conventional alloy, the dimensionless figure of merit *ZT*-curves in Figure 5.11 do not show a drastic reduction in *ZT* values of the nanocomposite. This can be explained by the increase observed in the Seebeck coefficient of the nanocomposite samples (see Figure 5.12). Seebeck coefficient of *n*-type nanocomposite samples in both directions; along and perpendicular to the extrusion axis has higher values in the whole measurement temperature range compared to the conventional *n*-type

alloy. A systematic study of *n*-type bismuth telluride based nanocomposite was not in the scope of our research work, however, we have tried it to test synthesis feasibility for both *p*-type and *n*-type materials. Hence, the doping level and conduction mode of matrix and nano-particles were not optimized. The added MoS₂ nano-inclusions are intrinsically *p*-type semiconductors, while the matrix is *n*-type. Therefore, charge carrier concentration of the nanocomposite decreased and led to lower electrical conductivity in nanocomposite samples. On the other hand, a lower carrier concentration leads to higher Seebeck coefficient.

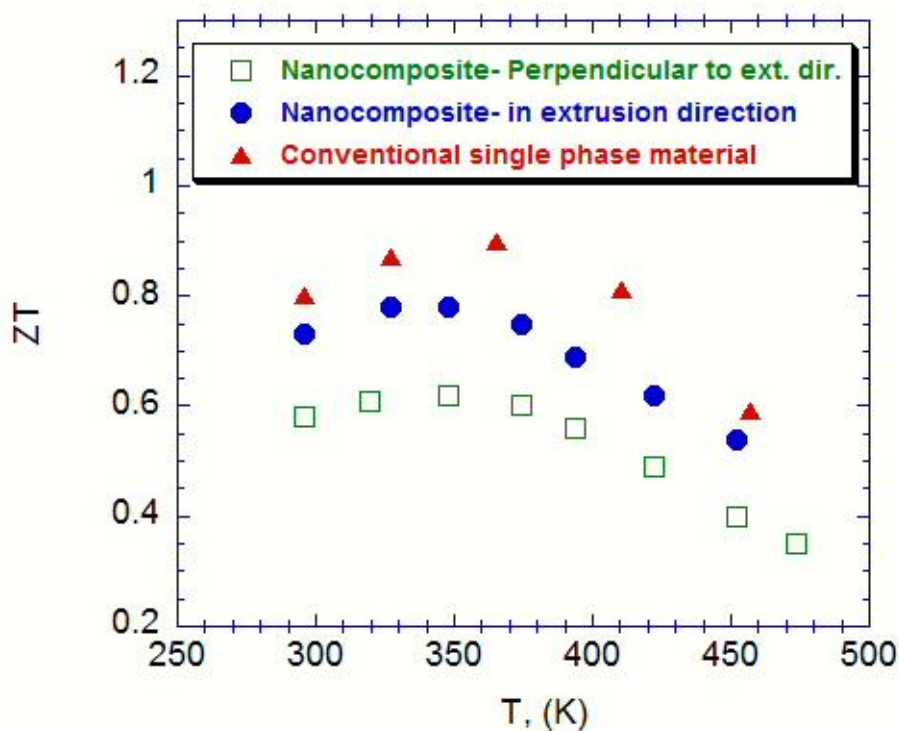


Figure 5.11: ZT values of *n*-type conventional and nanocomposite samples as a function of temperature. As in the previous figure, one of the samples is measured in a direction perpendicular to the extrusion axis.

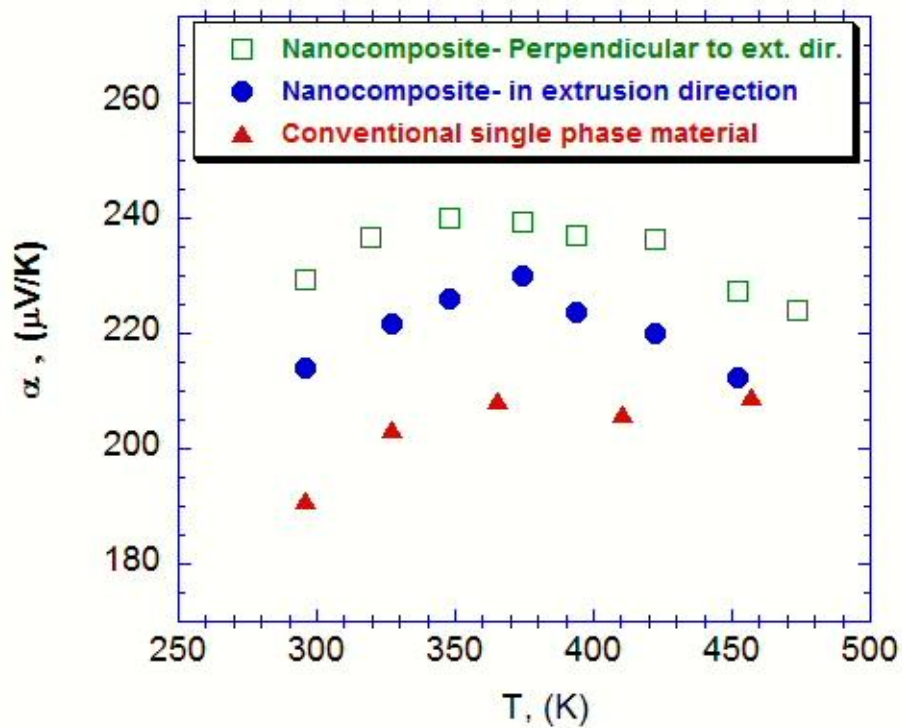


Figure 5.12: Seebeck coefficients of *n*-type conventional and nanocomposite (0.3 wt% MoS₂) samples as a function of temperature. Values of nanocomposite sample shown by blank squares were measured in the direction perpendicular to the extrusion axis.

Chapter 6 **SUMMARY AND GENERAL DISCUSSION**

Generally, the main idea of developing TE composites is to introduce more interfaces in the material in order to reduce the thermal conductivity by adding more phonon scattering mechanisms.

We expected that the numerous nanoscopic interfaces introduced in composites and nanocomposites could lead to a reduction of the lattice thermal conductivity, and accordingly to an improvement of the thermoelectric performance. We have also investigated the relation between structure and thermoelectric properties of produced materials.

In this Ph.D. work, two different types of bismuth telluride based composite TE materials were synthesized and investigated. The first type consists of coherent interfaces between phases in the composite, and the second type contains incoherent interfaces of nano-inclusions and matrix phase.

The first type of composites involves six different mixtures of compositions of *p*-type materials containing bismuth-antimony-telluride based alloys. Each component of the composites was obtained in powder form by mechanical alloying. The powders with two different compositions were mixed then consolidated by hot extrusion to obtain each bulk composite.

The second type of produced composites consists of *p*-type bismuth telluride based nanocomposites with three different concentrations of MoS₂ nano-inclusions. The matrix phase was synthesized by mechanical alloying, then the nano-particles of MoS₂ were mixed to the matrix in different concentrations, and finally each mixture was consolidated by hot extrusion to obtain the nanocomposites.

Microstructural analysis of all composites of first type indicates about 50% reduction in grain size compared to the conventional single phase alloy. This shows grain growth inhibition due to the presence of dissimilar phases in the material. On the other hand, microstructural and nanostructural analyses of nanocomposites of the second type show that nano-inclusions decorated the grain boundaries of the matrix. The flake-shaped nano-particles of MoS₂ with few atomic layers thickness limited the grain growth leading to a significant decrease in average grain and crystallite size of the nanocomposites compared to those of the conventional single phase

alloy. The nano-inclusions are dispersed throughout the matrix by distances in the order of few tens of nanometers. This homogeneous dispersion of nano-inclusions resulted in an average grain size reduction by a factor of around four in nanocomposites. In another words, the average grain size of the nanocomposites containing MoS_2 is almost half that of the composites of first type.

Since grain growth in the processing of nanostructured bismuth telluride based TE materials during hot extrusion or hot pressing the powders is one of the major issues, grain growth suppression in these materials is a significant achievement we could obtain in both approaches.

The compositions of the phases in all composites of first type are so close, thus diffraction of X-rays from planes of different phases in each composite leads to peak broadening instead of two separate peaks for each diffracting plane. Observed peak broadening in the composites materials lead to a reduction in calculated average crystallite size of the composites (Figure 3.3).

The XRD analyses of nanocomposites containing MoS_2 indicate that no chemical reaction takes place between $(\text{Bi}_{0.2}\text{Sb}_{0.8})_2\text{Te}_3$ and MoS_2 during the mixing and/or hot extrusion processes. However, peak broadening is also observed in all the nanocomposite samples compared to the conventional alloy. Comparing the crystallite size of the two powders and hot extruded bulk nanocomposites and single phase alloy of $(\text{Bi}_{0.2}\text{Sb}_{0.8})_2\text{Te}_3$ one can conclude that after the hot extrusion process the average crystallite size in nanocomposites increased by only 10% when it shows nearly 400% growth in the single phase bismuth telluride based alloy (Figure 5.4). In other words, adding MoS_2 nano-particles assists in keeping the nanostructure produced during the powder processing; this results in bulk nanocomposites with a nanostructure comparable to that of powders.

The two mechanisms of grain growth suppression in these novel TE nanocomposites that have been proposed are; 1) the grain growth inhibition mechanism due to the second phase particles, which is often called the Zener pinning or drag.; 2) the addition of MoS_2 nano-particles, which is a well-known solid state lubricant facilitates the extrusion process and consequently, materials containing MoS_2 nano-particles in the extrusion die are exposed to lower effective temperatures. Therefore, matrix grains recrystallization and growth is strongly inhibited compared to the conventional alloy.

According to the first mechanism, the migration of a grain boundary can be retarded by a dispersion of particles in the matrix. This process is called Zener drag (pinning). In fact, the point

in which grain growth will stop is where the driving force for grain growth and the drag force become equal. Therefore, for the boundary to move off the particle, an additional force has to be applied. This force is related to the size of particle and the energy of the boundary [201].

Therefore, both grain size and crystallite size of nanocomposites are smaller than conventional single phase alloy. Although the grain growth and recrystallization inhibition observed in both types of produced composites, however, they show more prominence in the nanocomposites containing MoS₂ nano-particles, which lead to higher density of scattering centers compared to that in the first type composites, yet more scattering centers are introduced in both composite types in comparison with conventional alloy, hence we expected both approaches to result in lower lattice thermal conductivity.

Few reports have been published concerning grain growth suppression and recrystallization reduction of bismuth telluride based TE materials during hot pressing. However, the mechanisms of grain growth hindering in the literature are almost the same as the proposed mechanisms for the materials in the presented work. For instant, Zhang et al. [202] used an organic agent (oleic acid) as additive during the ball milling process, to preserve the nanostructure obtained in the powders. They showed that higher concentrations of oleic acid led to smaller final grain size in the bulk samples. Kulbachinskii et al. [180] synthesized bismuth telluride based composites containing C₆₀ fullerene molecules. They showed that matrix grains were covered by C₆₀ molecules. Consequently, crystallite sizes of composites did not significantly increase during sintering (see Figure 6.1 and compare it to Figure 5.4).

We pursued investigation of structural changes in our nanocomposites. The structural changes of nanocomposites (second type) were studied by means of mechanical spectroscopy (MS) technique. Analysis of MS results show increase of IF_{bg} by the addition of MoS₂ nano-particles in the nanocomposites, which is consistent with the observed reduction of crystallite size by XRD. In addition, calculated activation energies of the internal frictions in the nanocomposites show systematic decrease by increasing the MoS₂ concentration in the materials.

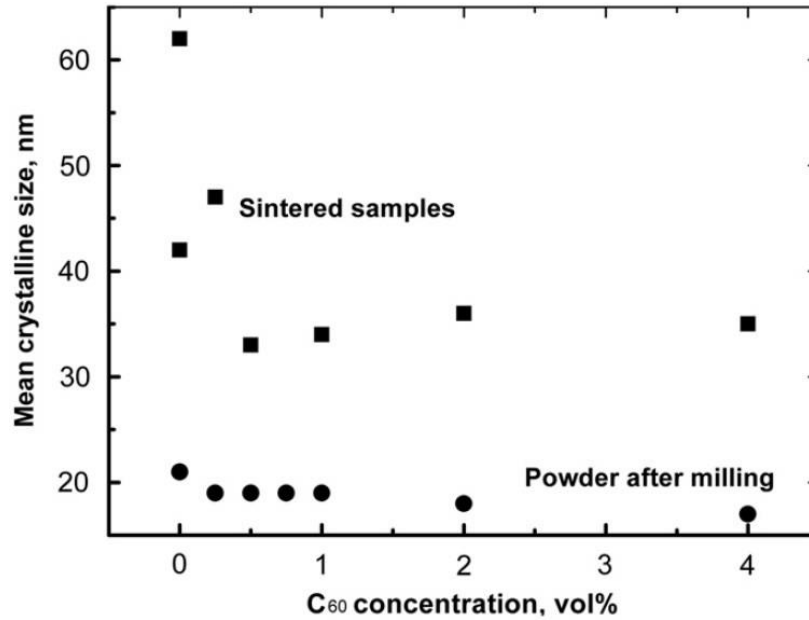


Figure 6.1: Mean crystallite size of powders after milling (circles) and sintered samples (squares) of bismuth telluride based nanocomposites as a function of fullerene concentration [180].

The measured increase in IF_{bg} and the trend observed in the reduction of the activation energy is an indication of higher density of crystal defects in the nanocomposites that largely contribute to the IF_{bg} . As we have shown earlier, adding nano-inclusions led to grain size reduction or, equivalently, a higher density of grain boundaries in the nanocomposites in contrast to the conventional alloys. Additionally, by adding more MoS₂ nano-particles the total area of interfaces between nano-inclusions and the matrix increases, which is another sources of crystal defects in the material. Moreover, the incoherent interfaces between the two phases, giving rise to localized strain at these interfaces. These localized strains affect the IF_{bg} as well.

Also, using the MS results could lead to the evaluation of Young's modulus of nanocomposites. Young's modulus shows a gradual increase in its value by growing the MoS₂ content in the nanocomposite. Consequently, the maximum increase of E (12%) at room temperature is observed in the alloy with 0.8 wt.% of MoS₂ nano-inclusions compared to the conventional alloy. The reduction of the grain size in nanocomposites also leads to less porosity, which is indirectly confirmed by an important increase of Young's modulus with the minimum amount of MoS₂ particles. The increase in Young's modulus can be also attributed to the higher Young's modulus of MoS₂ (240 GPa in bulk [203], 330-400 GPa in nano-flakes [204]), which leads to higher Young's modulus of composites according to the rule of mixture that is [205];

$$E_C = E_m V_m + E_{np} V_{np} \quad (6.1)$$

where E_C is the Young's modulus of composite, E_m stands for Young's modulus of matrix phase (that is around 48 GPa), E_{np} represents Young's modulus of nano-particles, V_m and V_{np} are volume fractions of matrix and nano-particles in the composite, respectively. Equation (6.1) is the general form of rule of mixture which is often modified due to the shape, type and orientation of the secondary phase. However, using this general form, one can obtain a rough estimation of the Young's modulus of our produced nanocomposites.

Although many TE materials are brittle and need improvement in their mechanical strength, the mechanical properties and elastic properties of TE materials have been less studied in comparison with TE properties, especially in case of composite TE materials. One study on mechanical and elastic properties of bismuth telluride based composites is reported by Ren and coworkers [206] where they synthesized bismuth antimony telluride containing 0.5 and 1 wt.% carbon nanotubes (CNTs). In contrast to our results for nanocomposites containing MoS₂ nano-particles, they reported reduced Young's modulus for samples with CNTs. They tried to explain this behavior by providing two arguments; the observation of aggregated CNTs in the grain boundary regions that can be considered as a defect phase, or elastic mismatch between CNTs and the matrix, which lead to lower Young's modulus. However, they stated that this behavior is not fully understood by the authors. Zhao et al. [108] investigated the Young's modulus of binary Bi₂Te₃ alloys containing SiC nano-particles. They showed that by adding 0.2, 0.5, and 1 vol.% SiC nano-particles the Young's modulus of composites increased compared to the single phase alloy of Bi₂Te₃ where they observed the maximum increase of E (around 30%) in samples with 0.5 vol.% of SiC . However, samples containing 1 vol.% SiC has lower Young's modulus in comparison with samples having 0.5 vol.%. They attributed this behavior to lower density (i. e. more porosity) of samples including 1 vol.% of SiC nano-particles.

In the composites of our first type, the charge carrier transport analyses demonstrate that at high temperatures hole transport is controlled by acoustic phonons while at low temperatures holes are predominantly scattered by ionized impurities. However, the charge carrier scattering due to alloying is expected to be negligible because of small difference in electronegativity between Bi and Sb. These analyses confirm that there is no evidence of carriers scattering mechanism linked to the composite nature in the produced composites. This behavior was predictable because of

similar lattice parameters of present phases in these composites leading to the coherent interfaces in the composites. Hence, the coherent interfaces between two different phases in each composite do not significantly affect carrier transport in the bulk TE materials.

On the contrary, adding MoS₂ nano-inclusions in the *p*-type materials led to electrical conductivity reduction in all nanocomposites of this type while we tried to keep the doping level of matrix the same as conventional alloy. The interfaces between nano-inclusions and matrix in this series of nanocomposites are incoherent due to the rather large differences in the lattice parameters of the two phases. This type of interface scatters not only the phonons but also the charge carriers, resulting in lower electrical conductivity. To restore the electrical conductivity to the conventional single phase alloy level, we increased the doping level in the nanocomposites containing 0.4 wt.% MoS₂.

Similar behavior is reported in the bismuth telluride based composites containing SiC and PbTe nano-inclusions [108, 207, 208]. Zhao et al. reported that by increasing the SiC nano-particle content from 0 to 1 vol.% in the bismuth telluride composites the electrical conductivity decreased by 28% at room temperature. Another report on bismuth antimony telluride based nanocomposites with PbTe nano-particles addition, shows significant decrease in the electrical transport properties, which was attributed to unfavorable doping effect [209]. These results also indicate the importance of type of nano-particles that can be used as nano-inclusions in TE nanocomposites.

Although in our study the main objective of making composites with coherent interfaces between constitutive phases was to improve the TE performance of the material, the peak *ZT* values in these composite series decreased continuously when changing from conventional alloy to composites made by binary phases due to slight increase of thermal conductivity in composites. The total thermal conductivity did not decrease when grain size and crystallite size were reduced in these composites since the constitutive phases of composites show higher lattice thermal conductivity compared to that of the single phase alloy. Furthermore, even though the grain size of the composites is reduced compared to that of the single-phase alloy, yet it is not small enough to scatter a large portion of phonons.

But, as it was expected, the nanocomposites with MoS₂ nano-particles showed a decrease of the thermal conductivity regardless of their doping level and processing parameters. Remarkably,

more pronounced reduction of thermal conductivity was observed as the temperature increases, meaning that phonons and charge carriers are more scattered at elevated temperatures in nanocomposites compared to the behavior observed in conventional single phase alloy. At temperatures above 450 K, a 20% thermal conductivity reduction is observed in a sample with 0.4 wt.% of MoS₂ nano-inclusions. In addition, near room temperature, in a range where there are no bipolar phenomena, the thermal conductivity of nanocomposites is lower even when their measured electrical conductivities are equal or higher to that of the conventional single-phase alloy.

Comparing the thermal conductivity of our nanocomposites with other bismuth telluride based TE composites with embedded nano-particles in the literature; we can conclude that an important achievement is made in this aspect of our study. For example, Ganguly et al. [207] used 0.1, 0.5, and 1 wt.% PbTe nano-particles in bismuth telluride based matrix and they observed systematic increase of total thermal conductivity by increasing the PbTe nano-particle content in the nanocomposites compared to the thermal conductivity of matrix. Zhao et al. [108] reported 20% reduction of thermal conductivity at room temperature in samples containing 1 vol.% SiC in Bi₂Te₃ matrix but thermal conductivity of composites surpasses that of the single phase alloy one at elevated temperatures (above 450 K). Zhang et al. [210] could not decrease the total thermal conductivity of bismuth antimony telluride based alloys by adding ZnAlO nano-inclusions, although they claimed they successfully could decrease the lattice thermal conductivity, while the total thermal conductivity increased due to higher electrical conductivity resulted by the introduction of these nano-particles. Although, in general, the reported studies present encouraging effect of adding nano-inclusions on phonon scattering, yet, there is a small number of papers on bismuth telluride based nanocomposites showing drastic decrease of total thermal conductivity by adding nano-particles. One such example, is reported by Sun et al. [211] where they showed by adding 15 vol.% of Zn₄Sb₃ nano-particles to Bi_{0.5}Sb_{1.5}Te₃ the total thermal conductivity of composites was reduced by around 25% at room temperature in comparison to that of the single phase of matrix.

Despite the decrease in the thermal conductivity of nanocomposites containing MoS₂ nano-particles, as we mentioned earlier, we have observed a higher electrical resistivity in composite samples resulting in an approximately 10% decrease in ZT at room temperature compared to that of the conventional (Bi_{0.2}Sb_{0.8})₂Te₃ alloy. However, at temperatures above 350 K, ZT values of

samples with MoS₂ additives become higher than those of the conventional alloy. In a sample with 0.4 wt% MoS₂, at a temperature of 370 K, the ZT value reaches 0.93, an increase of 8% with respect to that of the conventional alloy. The relatively small shifts in the optimum temperature range (i. e. temperature range with maximum ZT) are sometimes reported for TE composites with embedded nano-particles. Nevertheless, a shift that leads to move a TE material from one optimum temperature range category to another has not been reported [209].

Although the ZT in the composites of our first type did not improve due to their increased thermal conductivity, making composites of different bismuth telluride based phases did not significantly influence transport properties leading to no degradation of power factor. This result keeps the promise for this type of composites to enhance the TE performance if the thermal conductivity can be optimized.

In addition to the above discussion on nanocomposites with embedded MoS₂ nano-particles, we investigated the feasibility of this work on n -type bismuth telluride based alloy, and the grain size reduction was observed similarly in both p -type and n -type materials. These results spurred the promises not only on novel alternative TE materials to increase the TE performance, but also to enhance the mechanical properties of bismuth telluride based alloys.

As a recapitulation, we present in Table 6.1 a summary of comparisons between results in the literature and our study on bismuth telluride based nanocomposites with embedded nano-particles at 370 K. This temperature was chosen since the best ZT values of these examples are close or at this temperature, besides, this temperature highlights possible applications of these materials as generators close to room temperature.

Table 6.1 : Comparison between literature and our work on bismuth telluride based nanocomposites with embedded nano-particles.
The values are adopted from measurements at 370 K.

<i>Ref.</i>	<i>Matrix Composition</i>	<i>Nano-inclusion</i>	<i>Electrical resistivity (m Ωcm)</i>	<i>Seebeck coefficient (μV/K)</i>	<i>PF (μW/cmK²)</i>	<i>ZT</i>	<i>Lattice thermal conductivity reduction</i>	<i>Total thermal conductivity reduction</i>	<i>Grain size reduction</i>	<i>Crystallite size</i>
<i>Sun et al.[211]</i>	$Bi_{0.5}Sb_{1.5}Te_3$	Zn_4Sb_3 15 vol.%	1.7	200	23	0.6	~48%	~25%	N/A	~25nm
<i>Zhang et al.[210]</i>	$BiSbTe$	$ZnAlO$ 0.75 wt.%	0.41	165	66	1.3	~50%	~ -13%	N/A	N/A
<i>Zhao et al.[212]</i>	Bi_2Te_3	SiC 1 vol.%	1.05	-127	15	0.72	N/A	~ -3.5%	~50%	N/A
<i>Ganguly et al. [207]</i>	$Bi_{2-x}Sb_xTe_3$	$PbTe$ 1 wt.%	0.5	84	15.3	0.3	~50%	~ -22%	N/A	N/A
<i>Present work</i> <i>Keshavarz et al.</i>	$(Bi_{0.2}Sb_{0.8})_2Te_3$	MoS_2 0.4 wt. %	1.4	208.05	30.7	0.93	N/A	~20%	~75%	~20nm

CONCLUSIONS AND FUTURE DIRECTIONS

The work described in this dissertation is focused on the bismuth telluride based system for the fabrication of nanostructured composites and nanocomposites by means of mechanical alloying and hot extrusion. We have successfully employed this approach to synthesize bulk composite materials for thermoelectric applications. While many strides have been made to maximize the figure of merit of thermoelectric materials by making composite materials, typical production methods are mostly expensive, and not adaptable to large scale production for commercialization. The motivation for the research work described in this dissertation has been to synthesize and evaluate composite thermoelectric materials by simple process and fabrication techniques, which are suitable for mass production and comparatively inexpensive. In addition, bismuth telluride based alloys have marked anisotropic properties, and as a result it is necessary to texture the material to obtain better performance in a particular orientation. Accordingly, utilizing the hot extrusion technique is significantly beneficial to obtain such texture.

It is expected that this less complicated approach will contribute to develop many novel composite thermoelectric materials where texture is challenging.

Two different series of bismuth telluride based composites were synthesized and investigated. This study provides one of the first investigations of thermoelectric composites made of different phases of bismuth telluride alloys (Chapter 3), and bismuth telluride based nanocomposites when MoS₂ nano-inclusions are embedded (Chapter 4 and Chapter 5).

The composites made of bismuth antimony telluride based phases showed promising results in transport properties and power factor. As we expected, according to the theoretical predictions, the coherent interfaces in these series of composites can conserve the transport properties, yet the total performance of these composites did not enhance, hence, further studies on phase selection and their doping levels still need to be done.

On the other hand, although nanocomposites containing MoS₂ nano-particles demonstrated effective thermal conductivity reduction leading to improved figure of merit, depending on theoretical predictions and the expertise gained, yet the work on the nanocomposite TE materials containing nano-inclusions can be further extended by optimization of doping levels and a study

of the electronic and thermal properties of secondary phases (nano-inclusions) along with their effect on the structural changes of final products, which were determined in this work.

Both approaches of making bulk composites of bismuth telluride based alloys demonstrated promising results in significantly crystallite and grain sizes reduction which is an important achievement of this research work. However, addition of MoS₂ nano-particles can be designated as the superior approach to limit the grain and crystallite growth and obtain nanostructured bulk TE materials. In addition, evaluation of the elastic properties, which play a key role in performance of TE modules when they are under thermo-mechanical stresses, showed that not only thermal and electronic properties of TE materials can be engineered by making them composites but also the mechanical properties of these materials can be enhanced by this approach.

The simultaneous optimization of all three interrelated TE properties (thermal conductivity, Seebeck coefficient, and electrical conductivity) in nanocomposites containing nano-inclusions has not yet been reported. Hence, the most challenging part of the job, which is proper doping studies and employing the appropriate type of nano-particles to obtain optimized properties, remain to be completed. Beyond the experimental works introduced in this dissertation, thermal conductivity modeling of composites consisting phases of bismuth telluride based alloys, and bismuth telluride based nanocomposites containing nano-inclusions will be very worthy of finding the composition and volume percentage of each phase to predict composites with minimum thermal conductivity.

This research work mainly concentrated on *p*-type materials; still the feasibility of synthesizing *n*-type nanocomposites containing MoS₂ nano-inclusions has been shown. However, more investigations need to be done to synthesize *n*-type composites of both types with optimized TE properties by the approach introduced in this work.

Since adding MoS₂ nano-particles showed major effect on grain and crystallite size reduction in bismuth telluride based nanocomposites, to optimize TE properties of such nanocomposites, nano-particles of semiconductor compounds with similar crystal structures as MoS₂ but different electronic properties, such as WS₂, MoSe₂, and WTe₂ need to be studied as alternatives.

BIBLIOGRAPHY

- [1] H. J. Goldsmid, *Introduction to thermoelectricity*. Heidelberg ; New York: Springer, 2010.
- [2] J. Jiang, T. Zhang, Q. S. Zhang, Z. Xiong, J. M. Chen, Y. L. Zhang, W. Li, and G. J. Xu, "Enhanced thermoelectric performance in p-type BiSbTe bulk alloy with nano-inclusion of ZnAlO," *Applied Physics Letters*, vol. 98, Jan 10 2011.
- [3] L. D. Chen, Z. Xiong, X. H. Chen, X. Y. Zhao, S. Q. Bai, and X. Y. Huang, "Effects of nano-TiO₂ dispersion on the thermoelectric properties of filled-skutterudite Ba_{0.22}Co₄Sb₁₂," *Solid State Sciences*, vol. 11, pp. 1612-1616, Sep 2009.
- [4] J. Martin, L. Wang, L. Chen, and G. S. Nolas, "Enhanced Seebeck coefficient through energy-barrier scattering in PbTe nanocomposites," *Physical Review B*, vol. 79, Mar 2009.
- [5] T. M. Tritt, N. Gothard, X. Ji, and J. He, "Thermoelectric and transport properties of n-type Bi₂Te₃ nanocomposites," *Journal of Applied Physics*, vol. 103, Mar 1 2008.
- [6] Z. H. Zheng, P. Fan, J. T. Luo, G. X. Liang, and D. P. Zhang, "Enhanced Thermoelectric Properties of Antimony Telluride Thin Films with Preferred Orientation Prepared by Sputtering a Fan-Shaped Binary Composite Target," *Journal of Electronic Materials*, vol. 42, pp. 3421-3425, Dec 2013.
- [7] G. J. Tan, Y. Zheng, and X. F. Tang, "High thermoelectric performance of nonequilibrium synthesized CeFe₄Sb₁₂ composite with multi-scaled nanostructures," *Applied Physics Letters*, vol. 103, Oct 28 2013.
- [8] J. Liu, X. G. Wang, and L. M. Peng, "Effect of annealing on thermoelectric properties of eutectic PbTe-Sb₂Te₃ composite with self-assembled lamellar structure," *Intermetallics*, vol. 41, pp. 63-69, Oct 2013.
- [9] H. Xu and W. Wang, "Electrodeposition of MWNT/Bi₂Te₃ Composite Thermoelectric Films," *Journal of Electronic Materials*, vol. 42, pp. 1936-1945, Jul 2013.

- [10] Y. Du, K. F. F. Cai, S. Z. Shen, B. J. An, Z. Qin, and P. S. Casey, "Influence of sintering temperature on thermoelectric properties of Bi₂Te₃/Polythiophene composite materials," *Journal of Materials Science-Materials in Electronics*, vol. 23, pp. 870-876, Apr 2012.
- [11] K. C. Kim, W. C. Choi, H. J. Kim, H. K. Lyeo, J. S. Kim, and C. Park, "Thermoelectric Properties of Bi₂Te₃-In₂Se₃ Composite Thin Films Prepared by Co-Sputtering," *Journal of Nanoscience and Nanotechnology*, vol. 12, pp. 3633-3636, Apr 2012.
- [12] Y. Y. Wang, K. F. Cai, J. L. Yin, B. J. An, Y. Du, and X. Yao, "In situ fabrication and thermoelectric properties of PbTe-polyaniline composite nanostructures," *Journal of Nanoparticle Research*, vol. 13, pp. 533-539, Feb 2011.
- [13] H. J. Goldsmid, *Applications of thermoelectricity*. London, New York, : Methuen; Wiley, 1960.
- [14] E. Velme, "Thomas Johan Seebeck (1770-1831)," *Proc. Estonian Acad. Sci. Eng.*, vol. 13, pp. 276-282, 2007.
- [15] J. Snyder. (Accessed: 2011, 8 April). *Brief History of Thermoelectrics*. Available: <http://www.thermoelectrics.caltech.edu/thermoelectrics/history.html>
- [16] D. K. C. MacDonald, *Thermoelectricity: an introduction to the principles*. New York, : Wiley, 1962.
- [17] M. V. Vedernikov and E. K. Iordanishvili, "A.F. Ioffe and origin of modern semiconductor thermoelectric energy conversion," *Xvii International Conference on Thermoelectrics, Proceedings Ict 98*, pp. 37-42, 1998.
- [18] A. F. Ioffe, *Semiconductor thermoelements, and Thermoelectric cooling*, Rev. and supplemented for the English ed. London, : Infosearch, 1957.
- [19] M. S. Dresselhaus, G. Chen, M. Y. Tang, R. G. Yang, H. Lee, D. Z. Wang, Z. F. Ren, J. P. Fleurial, and P. Gogna, "New directions for low-dimensional thermoelectric materials," *Advanced Materials*, vol. 19, pp. 1043-1053, Apr 20 2007.
- [20] M. G. Kanatzidis, "Nanostructured Thermoelectrics: The New Paradigm?," *Chemistry of Materials*, vol. 22, pp. 648-659, Feb 9 2010.

- [21] G. J. Snyder and E. S. Toberer, "Complex thermoelectric materials," *Nature Materials*, vol. 7, pp. 105-114, Feb 2008.
- [22] D. M. Rowe and C. M. Bhandari, *Modern Thermoelectrics*: Reston Publishing Company, 1983.
- [23] N. W. Ashcroft and N. D. Mermin, *Solid state physics*: Holt, Rinehart and Winston; Saunders, 1976.
- [24] T. M. Tritt, *Thermal conductivity : theory, properties, and applications*. New York: Kluwer Academic/Plenum Publishers, 2004.
- [25] A. G. Guy, *Introduction to materials science*: McGraw-Hill, 1972.
- [26] A. Rockett, *The materials science of semiconductors*. New York: Springer, 2007.
- [27] C. Kittel, *Introduction to solid state physics*, 8th ed. Hoboken, NJ: Wiley, 2005.
- [28] M. Grundmann, *The physics of semiconductors : an introduction including nanophysics and applications*, 2nd ed. Berlin ; New York: Springer-Verlag, 2010.
- [29] W. S. Liu, X. Yan, G. Chen, and Z. F. Ren, "Recent advances in thermoelectric nanocomposites," *Nano Energy*, vol. 1, pp. 42-56, Jan 2012.
- [30] N. F. Mott, "Electrons in disordered structures," *Advances in Physics*, vol. 50, pp. 865-945, Nov 2001.
- [31] C. Y. Hou, K. Shtengel, and G. Refael, "Thermopower and Mott formula for a Majorana edge state," *Physical Review B*, vol. 88, Aug 7 2013.
- [32] S. R. Brown, S. M. Kauzlarich, F. Gascoin, and G. J. Snyder, "Yb₁₄MnSb₁₁: New high efficiency thermoelectric material for power generation," *Chemistry of Materials*, vol. 18, pp. 1873-1877, Apr 4 2006.
- [33] X. Shi, J. Yang, J. R. Salvador, M. F. Chi, J. Y. Cho, H. Wang, S. Q. Bai, J. H. Yang, W. Q. Zhang, and L. D. Chen, "Multiple-Filled Skutterudites: High Thermoelectric Figure of Merit through Separately Optimizing Electrical and Thermal Transports," *Journal of the American Chemical Society*, vol. 133, pp. 7837-7846, May 25 2011.

- [34] L. D. Hicks, T. C. Harman, and M. S. Dresselhaus, "Use of Quantum-Well Superlattices to Obtain a High Figure of Merit from Nonconventional Thermoelectric-Materials," *Applied Physics Letters*, vol. 63, pp. 3230-3232, Dec 6 1993.
- [35] L. D. Hicks and M. S. Dresselhaus, "Effect of Quantum-Well Structures on the Thermoelectric Figure of Merit," *Physical Review B*, vol. 47, pp. 12727-12731, May 15 1993.
- [36] L. D. Hicks, T. C. Harman, X. Sun, and M. S. Dresselhaus, "Experimental study of the effect of quantum-well structures on the thermoelectric figure of merit," *Physical Review B*, vol. 53, pp. 10493-10496, Apr 15 1996.
- [37] H. Beyer, J. Nurnus, H. Bottner, A. Lambrecht, T. Roch, and G. Bauer, "PbTe based superlattice structures with high thermoelectric efficiency," *Applied Physics Letters*, vol. 80, pp. 1216-1218, Feb 18 2002.
- [38] R. Venkatasubramanian, E. Siivola, T. Colpitts, and B. O'Quinn, "Thin-film thermoelectric devices with high room-temperature figures of merit," *Nature*, vol. 413, pp. 597-602, Oct 11 2001.
- [39] J. P. Heremans, C. M. Thrush, D. T. Morelli, and M. C. Wu, "Thermoelectric power of bismuth nanocomposites," *Physical Review Letters*, vol. 88, May 27 2002.
- [40] E. Alleno, L. Chen, C. Chubilleau, B. Lenoir, O. Rouleau, M. F. Trichet, and B. Villeroy, "Thermal Conductivity Reduction in CoSb(3)-CeO(2) Nanocomposites," *Journal of Electronic Materials*, vol. 39, pp. 1966-1970, Sep 2010.
- [41] S. F. Fan, J. N. Zhao, Q. Y. Yan, J. Ma, and H. H. Hng, "Influence of Nano-inclusions on Thermoelectric Properties of n-Type Bi(2)Te(3) Nanocomposites," *Journal of Electronic Materials*, vol. 40, pp. 1018-1023, May 2011.
- [42] J. L. Mi, X. B. Zhao, T. J. Zhu, and J. P. Tu, "Improved thermoelectric figure of merit in n-type CoSb₃ based nanocomposites," *Applied Physics Letters*, vol. 91, Oct 22 2007.
- [43] M. K. Keshavarz, D. Vasilevskiy, R. A. Masut, and S. Turenne, "p-Type Bismuth Telluride-Based Composite Thermoelectric Materials Produced by Mechanical Alloying and Hot Extrusion," *Journal of Electronic Materials*, vol. 42, pp. 1429-1435, Jul 2013.

- [44] K. F. Hsu, S. Loo, F. Guo, W. Chen, J. S. Dyck, C. Uher, T. Hogan, E. K. Polychroniadis, and M. G. Kanatzidis, "Cubic AgPbmSbTe_{2+m}: Bulk thermoelectric materials with high figure of merit," *Science*, vol. 303, pp. 818-821, Feb 6 2004.
- [45] J. Androulakis, K. F. Hsu, R. Pcionek, H. Kong, C. Uher, J. J. D'Angelo, A. Downey, T. Hogan, and M. G. Kanatzidis, "Nanostructuring and high thermoelectric efficiency in p-type Ag(Pb_{1-y}Sn_y)_mSbTe_{2+m}," *Advanced Materials*, vol. 18, pp. 1170-+, May 2 2006.
- [46] H. Lu, P. G. Burke, A. C. Gossard, G. Zeng, A. T. Ramu, J. H. Bahk, and J. E. Bowers, "Semimetal/Semiconductor Nanocomposites for Thermoelectrics," *Advanced Materials*, vol. 23, pp. 2377-2383, May 24 2011.
- [47] D.-H. Park, M.-Y. Kim, and T.-S. Oh, "Thermoelectric energy-conversion characteristics of n-type Bi₂(Te,Se)₃ nanocomposites processed with carbon nanotube dispersion," *Current Applied Physics*.
- [48] A. M. Strydom, "Thermal and transport properties of the cubic semimetal Y₃Ir₄Ge₁₃: on the metallic border of thermoelectric merit," *Journal of Physics-Condensed Matter*, vol. 19, Sep 26 2007.
- [49] J. M. O. Zide, J. H. Bahk, R. Singh, M. Zebarjadi, G. Zeng, H. Lu, J. P. Feser, D. Xu, S. L. Singer, Z. X. Bian, A. Majumdar, J. E. Bowers, A. Shakouri, and A. C. Gossard, "High efficiency semimetal/semiconductor nanocomposite thermoelectric materials (vol 108, 123702, 2010)," *Journal of Applied Physics*, vol. 110, Sep 1 2011.
- [50] V. Luhn, I. Zharskij, P. Zhukovski, and J. Partyka, "Application of thermoelectric effect in thin film semiconductor metal oxide to manufacture of gas sensors," *Przegląd Elektrotechniczny*, vol. 84, pp. 174-177, 2008.
- [51] V. F. Kraidenov, E. S. Itskevich, and M. N. Kotov, "Thermoelectric-Power of Ceramic Y-Ba-Cu-O with Different Content of Oxygen under Hydrostatic-Pressure up to 12 Kbar," *Fizika Nizkikh Temperatur*, vol. 16, pp. 1016-1020, Aug 1990.
- [52] G. Constantinescu, J. C. Diez, S. Rasekh, M. A. Madre, M. A. Torres, and A. Sotelo, "New promising Co-free thermoelectric ceramic based on Ba-Fe-oxide," *Journal of Materials Science-Materials in Electronics*, vol. 24, pp. 1832-1836, Jun 2013.

- [53] S. B. Cronin, Y. M. Lin, M. R. Black, O. Rabin, and M. S. Dresselhaus, "Thermoelectric transport properties of single bismuth nanowires," *Xxi International Conference on Thermoelectrics, Proceedings Ict '02*, pp. 243-248, 2002.
- [54] D. Nakamura, M. Murata, Y. Hasegawa, T. Komine, D. Uematsu, S. Nakamura, and T. Taguchi, "Thermoelectric Properties of a 593-nm Individual Bismuth Nanowire Prepared Using a Quartz Template," *Journal of Electronic Materials*, vol. 39, pp. 1960-1965, Sep 2010.
- [55] B. Abad, I. Alda, P. Diaz-Chao, H. Kawakami, A. Almarza, D. Amantia, D. Gutierrez, L. Aubouy, and M. Martin-Gonzalez, "Improved power factor of polyaniline nanocomposites with exfoliated graphene nanoplatelets (GNPs)," *Journal of Materials Chemistry A*, vol. 1, pp. 10450-10457, 2013.
- [56] O. Bubnova, Z. U. Khan, A. Malti, S. Braun, M. Fahlman, M. Berggren, and X. Crispin, "Optimization of the thermoelectric figure of merit in the conducting polymer poly(3,4-ethylenedioxythiophene)," *Nature Materials*, vol. 10, pp. 429-433, Jun 2011.
- [57] F. Yakuphanoglu, H. T. Liu, and J. K. Xu, "Electrical, optical, thermoelectric power, and dielectrical properties of organic semiconductor poly(1,12-bis(carbazolyl) dodecane) film," *Journal of Physical Chemistry B*, vol. 111, pp. 7535-7540, Jul 5 2007.
- [58] U. Ctirad, "Skutterudite-Based Thermoelectrics," in *Thermoelectrics Handbook*, ed: CRC Press, 2005, pp. 34-1-34-17.
- [59] X. Shi, L. D. Chen, S. Q. Bai, X. Y. Huang, X. Y. Zhao, Q. Yao, and C. Uher, "Influence of fullerene dispersion on high temperature thermoelectric properties of Ba(y)Co(4)Sb(12)-based composites," *Journal of Applied Physics*, vol. 102, Nov 15 2007.
- [60] Z. M. He, C. Stiewe, D. Platzek, G. Karpinski, E. Muller, S. H. Li, M. Toprak, and M. Muhammed, "Effect of ceramic dispersion on thermoelectric properties of nano-ZrO₂/CoSb₃ composites," *Journal of Applied Physics*, vol. 101, Feb 15 2007.
- [61] X. Y. Zhou, G. Y. Wang, L. Zhang, H. Chi, X. L. Su, J. Sakamoto, and C. Uher, "Enhanced thermoelectric properties of Ba-filled skutterudites by grain size reduction and Ag nanoparticle inclusion," *Journal of Materials Chemistry*, vol. 22, pp. 2958-2964, 2012.

- [62] C. Chubilleau, B. Lenoir, A. Dauscher, and C. Godart, "Low temperature thermoelectric properties of PbTe-CoSb₃ composites," *Intermetallics*, vol. 22, pp. 47-54, Mar 2012.
- [63] C. Chubilleau, B. Lenoir, P. Masschelein, A. Dauscher, C. Candolfi, E. Guilmeau, and C. Godart, "High temperature thermoelectric properties of CoSb₃ skutterudites with PbTe inclusions," *Journal of Materials Science*, vol. 48, pp. 2761-2766, Apr 2013.
- [64] C. Chubilleau, B. Lenoir, P. Masschelein, A. Dauscher, C. Candolfi, E. Guilmeau, and C. Godart, "Influence of ZnO nano-inclusions on the transport properties of the CoSb₃ skutterudite," *Journal of Alloys and Compounds*, vol. 554, pp. 340-347, Mar 25 2013.
- [65] D. T. Morelli and G. P. Meisner, "Low-Temperature Properties of the Filled Skutterudite CeFe₄Sb₁₂," *Journal of Applied Physics*, vol. 77, pp. 3777-3781, Apr 15 1995.
- [66] L. Fu, J. Yang, Y. Xiao, J. Peng, M. Liu, Y. Luo, and G. Li, "AgSbTe₂ nanoinclusion in Yb_{0.2}Co₄Sb₁₂ for high performance thermoelectrics," *Intermetallics*, vol. 43, pp. 79-84, 2013.
- [67] J. Y. Peng, X. Y. Liu, L. W. Fu, W. Xu, Q. Z. Liu, and J. Y. Yang, "Synthesis and thermoelectric properties of In_{0.2+x}Co₄Sb_{12+x} composite," *Journal of Alloys and Compounds*, vol. 521, pp. 141-145, Apr 25 2012.
- [68] X. Y. Zhao, X. Shi, L. D. Chen, W. Q. Zhang, S. Q. Bai, Y. Z. Pei, X. Y. Li, and T. Goto, "Synthesis of YbyCo₄Sb₁₂/Yb₂O₃ composites and their thermoelectric properties," *Applied Physics Letters*, vol. 89, Aug 28 2006.
- [69] J. L. Mi, X. B. Zhao, T. J. Zhu, and J. P. Tu, "Thermoelectric properties of Yb(0.15)Co(4)Sb(12) based nanocomposites with CoSb(3) nano-inclusion," *Journal of Physics D-Applied Physics*, vol. 41, Oct 21 2008.
- [70] X. Shi, J. Yang, J. R. Salvador, M. F. Chi, J. Y. Cho, H. Wang, S. Q. Bai, J. H. Yang, W. Q. Zhang, and L. D. Chen, "Multiple-Filled Skutterudites: High Thermoelectric Figure of Merit through Separately Optimizing Electrical and Thermal Transports (vol 133, pg 7837, 2011)," *Journal of the American Chemical Society*, vol. 134, pp. 2842-2842, Feb 8 2012.

- [71] G. Rogl, A. Grytsiv, P. Rogl, E. Bauer, M. B. Kerber, M. Zehetbauer, and S. Puchegger, "Multifilled nanocrystalline p-type didymium - Skutterudites with $ZT > 1.2$," *Intermetallics*, vol. 18, pp. 2435-2444, Dec 2010.
- [72] W. Xie, A. Weidenkaff, X. Tang, Q. Zhang, J. Poon, and T. Tritt, "Recent Advances in Nanostructured Thermoelectric Half-Heusler Compounds," *Nanomaterials*, vol. 2, pp. 379-412, 2012.
- [73] S. J. Poon, "Electronic and Thermoelectric Properties of Half-Heusler Alloys," in *Recent trends in thermoelectric materials research II*, T. M. Tritt, Ed., ed San Diego, Calif. ; London: Academic, 2001, pp. xvi, 299 p.
- [74] W. J. Xie, X. F. Tang, and Q. J. Zhang, "Fast preparation and thermal transport property of TiCoSb-based half-Heusler compounds," *Chinese Physics*, vol. 16, pp. 3549-3552, Nov 2007.
- [75] G. S. Nolas, D. C. Johnson, Mandrus David G., and Materials Research Society. Meeting, *Thermoelectric materials 2001--research and applications : symposium held November 26-29, 2001, Boston, Massachusetts, U.S.A.* Warrendale, Pennsylvania: Materials Research Society, 2002.
- [76] R. Yaqub, P. Sahoo, J. P. A. Makongo, N. Takas, P. F. P. Poudeu, and K. L. Stokes, "Investigation of the Effect of NiO Nanoparticles on the Transport Properties of $Zr_{0.5}Hf_{0.5}Ni_{1-x}PdxSn_{0.99}Sb_{0.01}$ ($x=0$ and 0.2)," *Science of Advanced Materials*, vol. 3, pp. 633-638, Aug 2011.
- [77] G. Joshi, X. Yan, H. Z. Wang, W. S. Liu, G. Chen, and Z. F. Ren, "Enhancement in Thermoelectric Figure-Of-Merit of an N-Type Half-Heusler Compound by the Nanocomposite Approach," *Advanced Energy Materials*, vol. 1, pp. 643-647, Jul 2011.
- [78] X. A. Yan, G. Joshi, W. S. Liu, Y. C. Lan, H. Wang, S. Lee, J. W. Simonson, S. J. Poon, T. M. Tritt, G. Chen, and Z. F. Ren, "Enhanced Thermoelectric Figure of Merit of p-Type Half-Heuslers," *Nano Letters*, vol. 11, pp. 556-560, Feb 2011.
- [79] C. Yu, T. J. Zhu, K. Xiao, J. J. Shen, S. H. Yang, and X. B. Zhao, "Reduced Grain Size and Improved Thermoelectric Properties of Melt Spun (Hf,Zr)NiSn Half-Heusler Alloys," *Journal of Electronic Materials*, vol. 39, pp. 2008-2012, Sep 2010.

- [80] X. Y. Huang, Z. Xu, and L. D. Chen, "The thermoelectric performance of ZrNiSiVZrO₂ composites," *Solid State Communications*, vol. 130, pp. 181-185, 2004.
- [81] X. Y. Huang, Z. Xu, L. D. Chen, and X. F. Tang, "Effect of gamma-Al₂O₃ content on the thermoelectric performance of ZrNiSn/gamma-Al₂O₃ composites," *Composite Materials Iii*, vol. 249, pp. 79-82, 2003.
- [82] W. J. Xie, J. He, S. Zhu, X. L. Su, S. Y. Wang, T. Holgate, J. W. Graff, V. Ponnambalam, S. J. Poon, X. F. Tang, Q. J. Zhang, and T. M. Tritt, "Simultaneously optimizing the independent thermoelectric properties in (Ti,Zr,Hf)(Co,Ni)Sb alloy by in situ forming InSb nano-inclusions," *Acta Materialia*, vol. 58, pp. 4705-4713, Aug 2010.
- [83] J. P. A. Makongo, D. K. Misra, X. Y. Zhou, A. Pant, M. R. Shabetai, X. L. Su, C. Uher, K. L. Stokes, and P. F. P. Poudeu, "Simultaneous Large Enhancements in Thermopower and Electrical Conductivity of Bulk Nanostructured Half-Heusler Alloys," *Journal of the American Chemical Society*, vol. 133, pp. 18843-18852, Nov 23 2011.
- [84] J. P. A. Makongo, D. K. Misra, J. R. Salvador, N. J. Takas, G. Y. Wang, M. R. Shabetai, A. Pant, P. Paudel, C. Uher, K. L. Stokes, and P. F. P. Poudeu, "Thermal and electronic charge transport in bulk nanostructured Zr_{0.25}Hf_{0.75}NiSn composites with full-Heusler inclusions," *Journal of Solid State Chemistry*, vol. 184, pp. 2948-2960, Nov 2011.
- [85] L. D. Chen, X. Y. Huang, M. Zhou, X. Shi, and W. B. Zhang, "The high temperature thermoelectric performances of Zr_{0.5}Hf_{0.5}Ni_{0.8}Pd_{0.2}Sn_{0.99}Sb_{0.01} alloy with nanophase inclusions," *Journal of Applied Physics*, vol. 99, Mar 15 2006.
- [86] S. J. Poon, D. Wu, S. Zhu, W. J. Xie, T. M. Tritt, P. Thomas, and R. Venkatasubramanian, "Half-Heusler phases and nanocomposites as emerging high-ZT thermoelectric materials," *Journal of Materials Research*, vol. 26, pp. 2795-2802, Nov 2011.
- [87] N. N. Greenwood and A. Earnshaw, *Chemistry of the elements*, 2nd ed. Oxford ; Boston: Butterworth-Heinemann, 1997.
- [88] O. Madelung, U. Rössler, and M. Schulz, "Lead telluride (PbTe) crystal structure, lattice parameters, thermal expansion," in *Non-Tetrahedrally Bonded Elements and Binary*

- Compounds I*. vol. 41C, O. Madelung, U. Rössler, and M. Schulz, Eds., ed: Springer Berlin Heidelberg, 1998, pp. 1-3.
- [89] C. A. a. e. o. t. v. III/17E-17F-41C, "Lead selenide (PbSe) crystal structure, lattice parameters, thermal expansion," in *Non-Tetrahedrally Bonded Elements and Binary Compounds I*. vol. 41C, O. Madelung, U. Rössler, and M. Schulz, Eds., ed: Springer Berlin Heidelberg, 1998, pp. 1-4.
- [90] C. A. a. e. o. t. v. III/17E-17F-41C, "Lead sulfide (PbS) crystal structure, lattice parameters, thermal expansion," in *Non-Tetrahedrally Bonded Elements and Binary Compounds I*. vol. 41C, O. Madelung, U. Rössler, and M. Schulz, Eds., ed: Springer Berlin Heidelberg, 1998, pp. 1-4.
- [91] M. H. Francombe, "Structure-cell data and expansion coefficients of bismuth telluride," *British Journal of Applied Physics*, vol. 9, pp. 415-417, 1958.
- [92] W. Huang, H. X. Da, and G. C. Liang, "Thermoelectric performance of MX₂ (M5M(o),W; X = S, Se) monolayers," *Journal of Applied Physics*, vol. 113, Mar 14 2013.
- [93] K. Biswas, J. Q. He, Q. C. Zhang, G. Y. Wang, C. Uher, V. P. Dravid, and M. G. Kanatzidis, "Strained endotaxial nanostructures with high thermoelectric figure of merit," *Nature Chemistry*, vol. 3, pp. 160-166, Feb 2011.
- [94] J. R. Sootsman, H. Kong, C. Uher, J. J. D'Angelo, C. I. Wu, T. P. Hogan, T. Caillat, and M. G. Kanatzidis, "Large Enhancements in the Thermoelectric Power Factor of Bulk PbTe at High Temperature by Synergistic Nanostructuring," *Angewandte Chemie-International Edition*, vol. 47, pp. 8618-8622, 2008.
- [95] P. F. R. Poudeu, J. D'Angelo, A. D. Downey, J. L. Short, T. P. Hogan, and M. G. Kanatzidis, "High thermoelectric figure of merit and nanostructuring in bulk p-type Na_{1-x}PbmSbyTe_{m+2}," *Angewandte Chemie-International Edition*, vol. 45, pp. 3835-3839, 2006.
- [96] Y. Z. Pei, J. Lensch-Falk, E. S. Toberer, D. L. Medlin, and G. J. Snyder, "High Thermoelectric Performance in PbTe Due to Large Nanoscale Ag-2 Te Precipitates and La Doping," *Advanced Functional Materials*, vol. 21, pp. 241-249, Jan 21 2011.

- [97] S. Johnsen, J. Q. He, J. Androulakis, V. P. Dravid, I. Todorov, D. Y. Chung, and M. G. Kanatzidis, "Nanostructures Boost the Thermoelectric Performance of PbS," *Journal of the American Chemical Society*, vol. 133, pp. 3460-3470, Mar 16 2011.
- [98] T. Ikeda, L. A. Collins, V. A. Ravi, F. S. Gascoin, S. M. Haile, and G. J. Snyder, "Self-assembled nanometer lamellae of thermoelectric PbTe and Sb₂Te₃ with epitaxy-like interfaces," *Chemistry of Materials*, vol. 19, pp. 763-767, Feb 20 2007.
- [99] T. Ikeda, V. A. Ravi, and G. J. Snyder, "Formation of Sb₂Te₃ Widmanstätten precipitates in thermoelectric PbTe," *Acta Materialia*, vol. 57, pp. 666-672, Feb 2009.
- [100] T. Ikeda, S. M. Haile, V. A. Ravi, H. Azizgolshani, F. Gascoin, and G. J. Snyder, "Solidification processing of alloys in the pseudo-binary PbTe-Sb₂Te₃ system," *Acta Materialia*, vol. 55, pp. 1227-1239, Feb 2007.
- [101] Y. Z. Pei, N. A. Heinz, A. LaLonde, and G. J. Snyder, "Combination of large nanostructures and complex band structure for high performance thermoelectric lead telluride," *Energy & Environmental Science*, vol. 4, pp. 3640-3645, Sep 2011.
- [102] S. Il Kim, K. Ahn, D. H. Yeon, S. Hwang, H. S. Kim, S. M. Lee, and K. H. Lee, "Enhancement of Seebeck Coefficient in Bi_{0.5}Sb_{1.5}Te₃ with High-Density Tellurium Nano-inclusions," *Applied Physics Express*, vol. 4, Sep 2011.
- [103] T. S. Basu, R. G. Yang, S. J. Thiagarajan, S. Ghosh, S. Gierlotka, and M. Ray, "Remarkable thermal conductivity reduction in metal-semiconductor nanocomposites," *Applied Physics Letters*, vol. 103, Aug 19 2013.
- [104] W. J. Xie, J. He, H. J. Kang, X. F. Tang, S. Zhu, M. Laver, S. Y. Wang, J. R. D. Copley, C. M. Brown, Q. J. Zhang, and T. M. Tritt, "Identifying the Specific Nanostructures Responsible for the High Thermoelectric Performance of (Bi,Sb)₂Te-₃ Nanocomposites," *Nano Letters*, vol. 10, pp. 3283-3289, Sep 2010.
- [105] B. Poudel, Q. Hao, Y. Ma, Y. C. Lan, A. Minnich, B. Yu, X. A. Yan, D. Z. Wang, A. Muto, D. Vashaee, X. Y. Chen, J. M. Liu, M. S. Dresselhaus, G. Chen, and Z. F. Ren, "High-thermoelectric performance of nanostructured bismuth antimony telluride bulk alloys," *Science*, vol. 320, pp. 634-638, May 2 2008.

- [106] D. K. Ko, Y. J. Kang, and C. B. Murray, "Enhanced Thermopower via Carrier Energy Filtering in Solution-Processable Pt-Sb₂Te₃ Nanocomposites," *Nano Letters*, vol. 11, pp. 2841-2844, Jul 2011.
- [107] D. W. Liu, J. F. Li, C. Chen, and B. P. Zhang, "Effects of SiC Nanodispersion on the Thermoelectric Properties of p-Type and n-Type Bi₂Te₃-Based Alloys," *Journal of Electronic Materials*, vol. 40, pp. 992-998, May 2011.
- [108] L. D. Zhao, B. P. Zhang, J. F. Li, H. L. Zhang, and W. S. Liu, "Enhanced thermoelectric and mechanical properties in textured n-type Bi₂Te₃ prepared by spark plasma sintering," *Solid State Sciences*, vol. 10, pp. 651-658, May 2008.
- [109] X. A. Yan, B. Poudel, Y. Ma, W. S. Liu, G. Joshi, H. Wang, Y. C. Lan, D. Z. Wang, G. Chen, and Z. F. Ren, "Experimental Studies on Anisotropic Thermoelectric Properties and Structures of n-Type Bi₂Te_{2.7}Se_{0.3}," *Nano Letters*, vol. 10, pp. 3373-3378, Sep 2010.
- [110] D. Vasilevskiy, J. M. Simard, F. Belanger, F. Bernier, S. Turenne, and J. L'Ecuyer, "Texture formation in extruded rods of (Bi,Sb)₂(Te,Se)₃ thermoelectric alloys.," *Xxi International Conference on Thermoelectrics, Proceedings Ict '02*, pp. 24-27, 2002.
- [111] J. Li, Q. Tan, J.-F. Li, D.-W. Liu, F. Li, Z.-Y. Li, M. Zou, and K. Wang, "BiSbTe-Based Nanocomposites with High ZT: The Effect of SiC Nanodispersion on Thermoelectric Properties," *Advanced Functional Materials*, vol. 23, pp. 4317-4323, 2013.
- [112] J. H. Yim, K. Jung, H. J. Kim, H. H. Park, C. Park, and J. S. Kim, "Effect of Composition on Thermoelectric Properties in PbTe-Bi₂Te₃ Composites," *Journal of Electronic Materials*, vol. 40, pp. 1010-1014, May 2011.
- [113] L. D. Hicks and M. S. Dresselhaus, "Thermoelectric Figure of Merit of a One-Dimensional Conductor," *Physical Review B*, vol. 47, pp. 16631-16634, Jun 15 1993.
- [114] J. Y. Tang, H. T. Wang, D. H. Lee, M. Fardy, Z. Y. Huo, T. P. Russell, and P. D. Yang, "Holey Silicon as an Efficient Thermoelectric Material," *Nano Letters*, vol. 10, pp. 4279-4283, Oct 2010.
- [115] Y. P. He, D. Donadio, J. H. Lee, J. C. Grossman, and G. Galli, "Thermal Transport in Nanoporous Silicon: Interplay between Disorder at Mesoscopic and Atomic Scales," *Acs Nano*, vol. 5, pp. 1839-1844, Mar 2011.

- [116] H. J. Goldsmid and R. W. Douglas, "Use of semiconductors in thermoelectric refrigeration," *British Journal of Applied Physics*, vol. 5, pp. 386-390, 1954.
- [117] J. R. Drabble and C. H. L. Goodman, "Chemical bonding in bismuth telluride," *Journal of the Physics and Chemistry of Solids*, vol. 5, pp. 142-144, 1958.
- [118] T. M. Tritt and M. A. Subramanian, "Thermoelectric materials, phenomena, and applications: A bird's eye view," *Mrs Bulletin*, vol. 31, pp. 188-194, Mar 2006.
- [119] H. J. Goldsmid, "Heat conduction in Bismuth telluride," *Proceedings of the Physical Society*, vol. 72, pp. 17-26, 1958.
- [120] H. J. Goldsmid, "The thermal conductivity of bismuth telluride," *Proceedings of the Physical Society. Section B*, vol. 69, pp. 203-209, 1956.
- [121] D. L. Greenaway and G. Harbeke, "Band structure of bismuth telluride, bismuth selenide and their respective alloys," *Journal of the Physics and Chemistry of Solids*, vol. 26, pp. 1585-1604, 1965.
- [122] H. J. Goldsmid, "Recent studies of bismuth telluride and its alloys," in *Conference on Semiconducting Compounds, 14 June 1961*, 1961, pp. 2198-2202.
- [123] H. Scherrer and S. Scherrer, "Bismuth Telluride, Antimony Telluride, and their Solid Solutions," in *CRC handbook of thermoelectrics*, D. M. Rowe, Ed., ed Boca Raton, FL: CRC Press, 1995, p. pp. 211
- [124] H. J. Goldsmid, "The electrical conductivity and thermo-electric power of bismuth telluride," *Proceedings of the Physical Society*, vol. 71, pp. 633-646, 1958.
- [125] J. P. Fleurial, L. Gailliard, and R. Triboulet, "Thermal properties of high quality single crystals of bismuth telluride. I. Experimental characterization," *Journal of the Physics and Chemistry of Solids*, vol. 49, pp. 1237-47, 1988.
- [126] C. B. Satterthwaite and R. W. Ure, Jr., "Electrical and thermal properties of Bi₂Te₃," *Physical Review*, vol. 108, pp. 1164-1170, 1957.
- [127] A. F. Ioffe, S. V. Airapetyants, A. V. Ioffe, N. V. Kolomoets, and L. S. Stil'bans, "On increasing the efficiency of semi-conducting thermocouples," *Doklady Akademii Nauk SSSR*, vol. 106, p. 981, 1956.

- [128] F. D. Rosi, B. Abeles, and R. V. Jensen, "Materials for thermoelectric refrigeration," *Physics and Chemistry of Solids*, vol. 10, pp. 191-200, 1959.
- [129] H. J. Goldsmid and R. T. Delves, "Materials for thermoelectric refrigeration," *GEC Journal*, vol. 28, pp. 102-105, 1961.
- [130] S. S. Kim, T. Aizawa, and S. Yamamoto, "Fabrication of anisotropically structured p-type and n-type Bi-Te thermoelectric materials via new P/M route," in *Powder Metallurgy World Congress & Exhibition (PM2004), 17-21 Oct. 2004*, Shrewsbury, UK, 2004, p. 6 pp.
- [131] C. C. Koch, *Nanostructured materials : processing, properties, and potential applications*. Norwich, N.Y.: Noyes Publications/William Andrew Pub., 2002.
- [132] P. A. Lee, *Optical and electrical properties*. Dordrecht ; Boston: D. Reidel Pub. Co., 1976.
- [133] T. Boker, R. Severin, A. Muller, C. Janowitz, R. Manzke, D. Voss, P. Kruger, A. Mazur, and J. Pollmann, "Band structure of MoS₂, MoSe₂, and alpha-MoTe₂: Angle-resolved photoelectron spectroscopy and ab initio calculations," *Physical Review B*, vol. 64, Dec 15 2001.
- [134] R. Coehoorn, C. Haas, J. Dijkstra, C. J. Flipse, R. A. de Groot, and A. Wold, "Electronic structure of MoSe₂, MoS₂, and WSe₂. I. Band-structure calculations and photoelectron spectroscopy," *Phys Rev B Condens Matter*, vol. 35, pp. 6195-6202, Apr 15 1987.
- [135] J. N. Coleman, M. Lotya, A. O'Neill, S. D. Bergin, P. J. King, U. Khan, K. Young, A. Gaucher, S. De, R. J. Smith, I. V. Shvets, S. K. Arora, G. Stanton, H. Y. Kim, K. Lee, G. T. Kim, G. S. Duesberg, T. Hallam, J. J. Boland, J. J. Wang, J. F. Donegan, J. C. Grunlan, G. Moriarty, A. Shmeliov, R. J. Nicholls, J. M. Perkins, E. M. Grieverson, K. Theuwissen, D. W. McComb, P. D. Nellist, and V. Nicolosi, "Two-Dimensional Nanosheets Produced by Liquid Exfoliation of Layered Materials," *Science*, vol. 331, pp. 568-571, Feb 4 2011.
- [136] T. S. Li and G. L. Galli, "Electronic properties of MoS₂ nanoparticles," *Journal of Physical Chemistry C*, vol. 111, pp. 16192-16196, Nov 8 2007.
- [137] S. Lebegue and O. Eriksson, "Electronic structure of two-dimensional crystals from ab initio theory," *Physical Review B*, vol. 79, Mar 2009.

- [138] X. Zong, H. Yan, G. Wu, G. Ma, F. Wen, L. Wang, and C. Li, "Enhancement of photocatalytic H₂ evolution on CdS by loading MoS₂ as Cocatalyst under visible light irradiation," *Journal of the American Chemical Society*, vol. 130, pp. 7176-7, Jun 11 2008.
- [139] J. L. Verble and T. J. Wieting, "LATTICE MODE DEGENERACY IN MOS₂ AND OTHER LAYER COMPOUNDS," *Physical Review Letters*, vol. 25, pp. 362-365, 1970.
- [140] Webpage. (Accessed on 30 Oct. 2013). *DRILUBE products containing molybdenum disulfide*. Available: <http://www.drilube.co.jp/english/product/molybdenum.html>
- [141] J. M. Martin, C. Donnet, T. Lemogne, and T. Epicier, "Superlubricity of Molybdenum-Disulfide," *Physical Review B*, vol. 48, pp. 10583-10586, Oct 1 1993.
- [142] M. V. Bollinger, K. W. Jacobsen, and J. K. Norskov, "Atomic and electronic structure of MoS₂ nanoparticles," *Physical Review B*, vol. 67, Feb 15 2003.
- [143] J. P. Wilcoxon, P. P. Newcomer, and G. A. Samara, "Synthesis and optical properties of MoS₂ and isomorphous nanoclusters in the quantum confinement regime," *Journal of Applied Physics*, vol. 81, pp. 7934-7944, Jun 15 1997.
- [144] J. P. Wilcoxon and G. A. Samara, "Strong Quantum-Size Effects in a Layered Semiconductor - Mos₂ Nanoclusters," *Physical Review B*, vol. 51, pp. 7299-7302, Mar 15 1995.
- [145] A. Kumar and P. K. Ahluwalia, "A first principle Comparative study of electronic and optical properties of 1H - MoS₂ and 2H - MoS₂," *Materials Chemistry and Physics*, vol. 135, pp. 755-761, Aug 15 2012.
- [146] A. Kumar and P. K. Ahluwalia, "Electronic structure of transition metal dichalcogenides monolayers 1H-MX₂ (M = Mo, W; X = S, Se, Te) from ab-initio theory: new direct band gap semiconductors," *European Physical Journal B*, vol. 85, Jun 2012.
- [147] K. F. Mak, C. Lee, J. Hone, J. Shan, and T. F. Heinz, "Atomically Thin MoS₂: A New Direct-Gap Semiconductor," *Physical Review Letters*, vol. 105, Sep 24 2010.
- [148] X. J. Liu, G. Zhang, Q. X. Pei, and Y. W. Zhang, "Phonon thermal conductivity of monolayer MoS₂ sheet and nanoribbons," *Applied Physics Letters*, vol. 103, Sep 23 2013.

- [149] M. Buscema, M. Barkelid, V. Zwiller, H. S. J. van der Zant, G. A. Steele, and A. Castellanos-Gomez, "Large and Tunable Photothermoelectric Effect in Single-Layer MoS₂," *Nano Letters*, vol. 13, pp. 358-363, Feb 2013.
- [150] V. Varshney, S. S. Patnaik, C. Muratore, A. K. Roy, A. A. Voevodin, and B. L. Farmer, "MD simulations of molybdenum disulphide (MoS₂): Force-field parameterization and thermal transport behavior," *Computational Materials Science*, vol. 48, pp. 101-108, Mar 2010.
- [151] F. Belanger, "Etude d'alliages thermoelectriques bismuth-tellure-selenium elaborés par metallurgie des poudres," MQ71228 M.Sc.A., Ecole Polytechnique, Montreal (Canada), Ann Arbor, 2001.
- [152] F. Bernier, "Caracterisation des alliages thermoelectriques et simulation numerique de l'extrusion a chaud," MQ89180 M.Sc.A., Ecole Polytechnique, Montreal (Canada), Ann Arbor, 2003.
- [153] B. D. Cullity, "Elements of x-ray diffraction," in *Addison-Wesley series in metallurgy and materials*, 2d ed Reading, Mass.: Addison-Wesley Pub. Co., 1978, p. 102.
- [154] F. H. Chung and D. K. Smith, *Industrial applications of X-ray diffraction*. New York: Marcel Dekker, 2000.
- [155] T. C. Harman, "Special Techniques for Measurement of Thermoelectric Properties," *Journal of Applied Physics*, vol. 29, pp. 1373-1374, 1958.
- [156] M. Razeghi, "Non-equilibrium electrical properties of semiconductors," in *Fundamentals of solid state engineering*, 3rd ed New York: Springer, 2009, pp. 316-318.
- [157] L. J. Van der Pauw, "A Method of Measuring The Resistivity and Hall coefficient on Lamellae of Arbitrary Shape," *Philips Technical Review*, vol. 20, pp. 220-224, 1958.
- [158] G. Roebben, B. Basu, J. Vleugels, J. Van Humbeeck, and O. Van der Biest, "The innovative impulse excitation technique for high-temperature mechanical spectroscopy," *Journal of Alloys and Compounds*, vol. 310, pp. 284-287, Sep 28 2000.
- [159] G. Roebben, B. Bollen, A. Brebels, J. Van Humbeeck, and O. Van der Biest, "Impulse excitation apparatus to measure resonant frequencies, elastic moduli, and internal friction

- at room and high temperature," *Review of Scientific Instruments*, vol. 68, pp. 4511-4515, Dec 1997.
- [160] A. S. Nowick and B. S. Berry, "Anelastic relaxation in crystalline solids," in *Materials science series v 1*, ed New York,: Academic Press, 1972, pp. 156-463.
- [161] R. G. Duan, G. Roebben, O. Van Biest, K. M. Liang, and S. R. Gu, "Microstructure research of glasses by impulse excitation technique (IET)," *Journal of Non-Crystalline Solids*, vol. 281, pp. 213-220, Mar 2001.
- [162] O. Bourbia, "Etude des frottements internes dans le tellurure de bismuth prepare par extrusion," MR82571 M.Sc.A., Ecole Polytechnique, Montreal (Canada), Ann Arbor, 2011.
- [163] J. Snyder. (2010). *Thermoelectric Nanomaterials*. Available: <http://thermoelectrics.caltech.edu/thermoelectrics/nanomaterials.html>
- [164] W. Liu, X. Yan, G. Chen, and Z. Ren, "Recent advances in thermoelectric nanocomposites," *Nano Energy*, vol. 1, pp. 42-56, 2012.
- [165] M. G. Kanatzidis, P. F. P. Poudeu, J. D'Angelo, H. J. Kong, A. Downey, J. L. Short, R. Pcionek, T. P. Hogan, and C. Uher, "Nanostructures versus solid solutions: Low lattice thermal conductivity and enhanced thermoelectric figure of merit in $Pb_{9.6}Sb_{0.2}Te_{10-x}Se_x$ bulk materials," *Journal of the American Chemical Society*, vol. 128, pp. 14347-14355, Nov 8 2006.
- [166] M. G. Kanatzidis, P. F. P. Poudeu, A. Gueguen, C. I. Wu, and T. Hogan, "High Figure of Merit in Nanostructured n-Type $KPb(m)SbTe(m+2)$ Thermoelectric Materials," *Chemistry of Materials*, vol. 22, pp. 1046-1053, Feb 9 2010.
- [167] Z. He, C. Stiewe, S. Li, D. Platzek, G. Karpinski, E. Muller, M. Toprak, and M. Muhammed, "Processing and characterization of nano-structured $ZrO_2/CoSb_3$ thermoelectric composites," *ICT'06: XXV International Conference on Thermoelectrics, Proceedings*, pp. 701-705, 2006.
- [168] M. G. Kanatzidis, J. Androulakis, K. F. Hsu, R. Pcionek, H. Kong, C. Uher, J. J. D'Angelo, A. Downey, and T. Hogan, "Nanostructuring and high thermoelectric efficiency

- in p-type $\text{Ag}(\text{Pb}_{1-y}\text{Sn}_y)_m\text{SbTe}_{2+m}$," *Advanced Materials*, vol. 18, pp. 1170+, May 2 2006.
- [169] X. H. Ji, J. He, Z. Su, N. Gothard, and T. M. Tritt, "Improved thermoelectric performance in polycrystalline p-type Bi_2Te_3 via an alkali metal salt hydrothermal nanocoating treatment approach," *Journal of Applied Physics*, vol. 104, Aug 1 2008.
- [170] A. Popescu and L. M. Woods, "Enhanced thermoelectricity in composites by electronic structure modifications and nanostructuring," *Applied Physics Letters*, vol. 97, pp. 052102-3, 2010.
- [171] Y. Zhang, X. Z. Ke, C. F. Chen, J. H. Yang, and P. R. C. Kent, "Nanodopant-Induced Band Modulation in AgPbmSbTe_{2+m} -Type Thermoelectrics," *Physical Review Letters*, vol. 106, May 20 2011.
- [172] J. M. Simard, D. Vasilevskiy, F. Belanger, J. L'Ecuyer, and S. Turenne, "Production of thermoelectric materials by mechanical alloying - Extrusion process," *Twentieth International Conference on Thermoelectrics, Proceedings*, pp. 132-135, 2001.
- [173] C. Andre, D. Vasilevskiy, S. Turenne, and R. A. Masut, "Increase in the density of states in n-type extruded $(\text{Bi}_{1-x}\text{Sb}_x)_2(\text{Te}_{1-y}\text{Se}_y)_3$ thermoelectric alloys," *Journal of Physics D-Applied Physics*, vol. 44, Jun 15 2011.
- [174] G. A. Slack, ",," in *CRC handbook of thermoelectrics*, D. M. Rowe, Ed., ed Boca Raton, FL: CRC Press, 1995, pp. 407-440.
- [175] K. Seeger, "Semiconductor physics : an introduction," in *Springer series in solid-state sciences*, 4th ed Berlin ; New York: Springer-Verlag, 1989, pp. 160-165.
- [176] G. Chen, M. S. Dresselhaus, G. Dresselhaus, J. P. Fleurial, and T. Caillat, "Recent developments in thermoelectric materials," *International Materials Reviews*, vol. 48, pp. 45-66, Feb 2003.
- [177] M.-S. Jeng, D. Song, G. Chen, and R. Yang, "Modeling the Thermal Conductivity and Phonon Transport in Nanoparticle Composites Using Monte Carlo Simulation," *Journal of Heat Transfer*, vol. 130, pp. 042410-042410, 2008.

- [178] A. J. Minnich, M. S. Dresselhaus, Z. F. Ren, and G. Chen, "Bulk nanostructured thermoelectric materials: current research and future prospects," *Energy & Environmental Science*, vol. 2, pp. 466-479, 2009.
- [179] D. H. Park, M. Y. Kim, and T. S. Oh, "Thermoelectric energy-conversion characteristics of n-type Bi₂(Te,Se)₃ nanocomposites processed with carbon nanotube dispersion," *Current Applied Physics*, vol. 11, pp. S41-S45, Jul 2011.
- [180] V. A. Kulbachinskii, V. G. Kytin, M. Y. Popov, S. G. Buga, P. B. Stepanov, and V. D. Blank, "Composites of Bi_{2-x}Sb_xTe₃ nanocrystals and fullerene molecules for thermoelectricity," *Journal of Solid State Chemistry*, vol. 193, pp. 64-70, Sep 2012.
- [181] D. Vasilevskiy, S. Turenne, and R. A. Masut, "Application of mechanical spectroscopy to the study of high performance (Bi_{1-x}Sb_x)₂(Te_{1-y}Se_y)₃ extruded thermoelectric alloys," presented at the ICT 2007. 26th International Conference on Thermoelectrics, 2007.
- [182] T. C. Harman, J. H. Cahn, and M. J. Logan, "Measurement of thermal conductivity by utilization of Peltier effect," *Journal of Applied Physics*, vol. 30, pp. 1351-1359, 1959.
- [183] M. S. Blanter, "Internal friction in metallic materials a handbook," in *Internal friction in metallic materials a handbook*, ed. Berlin ; New York: Springer, 2007, pp. 11-121.
- [184] K. K. Chawla, "Crystallographic Nature of Interface," in *Composite materials : science and engineering*, 2nd ed New York: Springer, 1998, pp. 110-111.
- [185] R. Mitra and Y. R. Mahajan, "Interfaces in Discontinuously Reinforced Metal-Matrix Composites - an Overview," *Bulletin of Materials Science*, vol. 18, pp. 405-434, Aug 1995.
- [186] A. G. Metcalfe, *Interfaces in metal matrix composites*. New York,: Academic Press, 1974.
- [187] W. Kim, J. Zide, A. Gossard, D. Klenov, S. Stemmer, A. Shakouri, and A. Majumdar, "Thermal conductivity reduction and thermoelectric figure of merit increase by embedding nanoparticles in crystalline semiconductors," *Physical Review Letters*, vol. 96, Feb 3 2006.

- [188] X. Y. Qin and X. H. Yang, "Giant scattering parameter and enhanced thermoelectric properties originating from synergetic scattering of electrons in semiconductors with metal nanoinclusions," *Applied Physics Letters*, vol. 97, Nov 8 2010.
- [189] L. H. Liang, Y. G. Wei, and B. Li, "Thermal conductivity of composites with nanoscale inclusions and size-dependent percolation," *Journal of Physics-Condensed Matter*, vol. 20, Sep 10 2008.
- [190] P. A. Sharma, J. D. Sugar, and D. L. Medlin, "Influence of nanostructuring and heterogeneous nucleation on the thermoelectric figure of merit in AgSbTe(2)," *Journal of Applied Physics*, vol. 107, Jun 1 2010.
- [191] L. E. Cassels, T. E. Buehl, P. G. Burke, C. J. Palmstrom, A. C. Gossard, G. Pernot, A. Shakouri, C. R. Haughn, M. F. Doty, and J. M. O. Zide, "Growth and characterization of TbAs:GaAs nanocomposites," *Journal of Vacuum Science & Technology B*, vol. 29, May 2011.
- [192] K. T. Delaney, N. A. Spaldin, and C. G. Van de Walle, "Theoretical study of the structural and electronic properties of strained ErAs," *Physical Review B*, vol. 77, Jun 2008.
- [193] B. C. Sales, "Thermoelectric materials - Smaller is cooler," *Science*, vol. 295, pp. 1248-1249, Feb 15 2002.
- [194] L. E. Bell, "Cooling, heating, generating power, and recovering waste heat with thermoelectric systems," *Science*, vol. 321, pp. 1457-1461, Sep 12 2008.
- [195] M. Saleemi, M. S. Toprak, S. H. Li, M. Johnsson, and M. Muhammed, "Synthesis, processing, and thermoelectric properties of bulk nanostructured bismuth telluride (Bi₂Te₃)," *Journal of Materials Chemistry*, vol. 22, pp. 725-730, Jan 14 2012.
- [196] Y. C. Lan, B. Poudel, Y. Ma, D. Z. Wang, M. S. Dresselhaus, G. Chen, and Z. F. Ren, "Structure Study of Bulk Nanograined Thermoelectric Bismuth Antimony Telluride," *Nano Letters*, vol. 9, pp. 1419-1422, Apr 2009.
- [197] W. Huang, H. Da, and G. Liang, "Thermoelectric performance of MX₂ (M = Mo, W; X = S, Se) monolayers," *Journal of Applied Physics*, vol. 113, p. 104304, Mar 14 2013.

- [198] H. H. Guo, T. Yang, P. Tao, Y. Wang, and Z. D. Zhang, "High pressure effect on structure, electronic structure, and thermoelectric properties of MoS₂," *Journal of Applied Physics*, vol. 113, Jan 7 2013.
- [199] S. Turenne, T. Clin, D. Vasilevskiy, and R. A. Masut, "Finite Element Thermomechanical Modeling of Large Area Thermoelectric Generators based on Bismuth Telluride Alloys," *Journal of Electronic Materials*, vol. 39, pp. 1926-1933, Sep 2010.
- [200] D. Vasilevskiy, S. Turenne, and R. A. Masut, "Application of mechanical spectroscopy to the study of high performance (Bi_{1-x}Sb_x)₂(Te_{1-y}Se_y)₃ extruded thermoelectric alloys," in *Thermoelectrics, 2007. ICT 2007. 26th International Conference on*, 2007, pp. 45-48.
- [201] E. Nes, N. Ryum, and O. Hunderi, "On the Zener drag," *Acta Metallurgica*, vol. 33, pp. 11-22, 1985.
- [202] Q. Zhang, Q. Y. Zhang, S. Chen, W. S. Liu, K. Lukas, X. Yan, H. Z. Wang, D. Z. Wang, C. Opeil, G. Chen, and Z. F. Ren, "Suppression of grain growth by additive in nanostructured p-type bismuth antimony tellurides," *Nano Energy*, vol. 1, pp. 183-189, Jan 2012.
- [203] J. L. Feldman, "Elastic constants of 2H-MoS₂ and 2H-NbSe₂ extracted from measured dispersion curves and linear compressibilities," *Journal of Physics and Chemistry of Solids*, vol. 37, pp. 1141-1144, 1976.
- [204] A. Castellanos-Gomez, M. Poot, G. A. Steele, H. S. J. van der Zant, N. Agrait, and G. Rubio-Bollinger, "Elastic Properties of Freely Suspended MoS₂ Nanosheets," *Advanced Materials*, vol. 24, pp. 772-+, Feb 7 2012.
- [205] M. Balasubramaniam, "Introduction to Composites," in *Composite Materials and Processing*, ed: CRC Press, 2013, pp. 1-30.
- [206] F. Ren, H. Wang, P. A. Menchhofer, and J. O. Kiggans, "Thermoelectric and mechanical properties of multi-walled carbon nanotube doped Bi_{0.4}Sb_{1.6}Te₃ thermoelectric material," *Applied Physics Letters*, vol. 103, Nov 25 2013.
- [207] S. Ganguly, C. Zhou, D. Morelli, J. Sakamoto, C. Uher, and S. L. Brock, "Synthesis and evaluation of lead telluride/bismuth antimony telluride nanocomposites for thermoelectric applications," *Journal of Solid State Chemistry*, vol. 184, pp. 3195-3201, Dec 2011.

- [208] C. Chen, D. W. Liu, B. P. Zhang, and J. F. Li, "Enhanced Thermoelectric Properties Obtained by Compositional Optimization in p-Type $\text{Bi}_x\text{Sb}_{2-x}\text{Te}_3$ Fabricated by Mechanical Alloying and Spark Plasma Sintering," *Journal of Electronic Materials*, vol. 40, pp. 942-947, May 2011.
- [209] Y. Ma, R. Heijl, and A. E. C. Palmqvist, "Composite thermoelectric materials with embedded nanoparticles," *Journal of Materials Science*, vol. 48, pp. 2767-2778, Apr 2013.
- [210] T. Zhang, Q. S. Zhang, J. Jiang, Z. Xiong, J. M. Chen, Y. L. Zhang, W. Li, and G. J. Xu, "Enhanced thermoelectric performance in p-type BiSbTe bulk alloy with nano-inclusion of ZnAlO ," *Applied Physics Letters*, vol. 98, Jan 10 2011.
- [211] J. H. Sun, X. Y. Qin, H. X. Xin, D. Li, L. Pan, C. J. Song, J. Zhang, R. R. Sun, Q. Q. Wang, and Y. F. Liu, "Synthesis and thermoelectric properties of $\text{Zn}_4\text{Sb}_3/\text{Bi}_{0.5}\text{Sb}_{1.5}\text{Te}_3$ bulk nanocomposites," *Journal of Alloys and Compounds*, vol. 500, pp. 215-219, Jun 25 2010.
- [212] L. D. Zhao, B. P. Zhang, J. F. Li, M. Zhou, W. S. Liu, and J. Liu, "Thermoelectric and mechanical properties of nano-SiC-dispersed Bi_2Te_3 fabricated by mechanical alloying and spark plasma sintering," *Journal of Alloys and Compounds*, vol. 455, pp. 259-264, May 8 2008.

APPENDIX – LIST OF AUTHOR’S CONTRIBUTIONS DURING THIS PROJECT

1. Journal papers:

- Mohsen K. Keshavarz, Dimitri Vasilevskiy, Remo A. Masut, Sylvain Turenne, “Effect of grain growth suppression by MoS₂ nanoparticles in hot extruded (Bi_{0.2}Sb_{0.8})₂Te₃ thermoelectric alloys”, *Journal of Electronic Materials*, accepted in January 2014.
- Mohsen K. Keshavarz, Dimitri Vasilevskiy, Remo A. Masut, Sylvain Turenne, “Synthesis of bismuth telluride-based thermoelectric nanocomposites containing MoS₂ nano-inclusions”, *Journal of Materials Characterization*, Submitted in March 2014.
- Mohsen K. Keshavarz, Dimitri Vasilevskiy, Remo A. Masut, Sylvain Turenne, “*p*-type bismuth telluride based composite thermoelectric materials produced by mechanical alloying and hot extrusion”, *Journal of Electronic Materials*, Volume 42, Issue 7, pp 1429-1435, 2013.
- S. Kashi, M. K. Keshavarz, D. Vasilevskiy, R. A. Masut, S. Turenne, “Effect of Surface Preparation on Mechanical Properties of Ni Contacts on Polycrystalline (Bi_{1-x}Sb_x)₂(Te_{1-y}Se_y)₃ Alloys”, *Journal of Electronic Materials*, Volume 41, Issue 6, pp 1227-1231, 2012.
- Mohsen K. Keshavarz, Dimitri Vasilevskiy, Remo A. Masut, Sylvain Turenne, “Mechanical properties of bismuth telluride based nanocomposites with embedded MoS₂ nano-particles”, (in preparation).

2. Contributions in international conferences:

- The 30th International Conference on Thermoelectrics (ICT 2011), July 17-21, 2011, Traverse City, Michigan, USA. Presented work: “Effect of Surface Preparation on Mechanical Properties of Ni Contacts on Polycrystalline

(Bi_{1-x}Sb_x)₂(Te_{1-y}Se_y)₃ Alloys”, S. Kashi, M. K. Keshavarz, D. Vasilevskiy, R. A. Masut, S. Turenne.

- ICT/ECT Joint Conference 2012, July 9-12, 2012, Aalborg, Denmark. Presented work: “*p*-type bismuth telluride based composite thermoelectric materials produced by mechanical alloying and hot extrusion”, Mohsen K. Keshavarz, Dimitri Vasilevskiy, Remo A. Masut, Sylvain Turenne.
- Trends in Nano Technology (TNT2012), September 10-14, 2012, Madrid, Spain. Presented work: “Nanostructured thermoelectric alloys obtained by mechanical alloying followed by hot extrusion or by microwave sintering”, M.K. Keshavarz, J. Arreguin-Zavala, D. Vasilevskiy, S. Turenne and R.A. Masut.
- The 32nd International Conference on Thermoelectrics (ICT2013), June 30- July 4, 2013, Kobe, Japan. Presented work: “Effect of grain growth suppression by MoS₂ nanoparticles in hot extruded (Bi_{0.2}Sb_{0.8})₂Te₃ thermoelectric alloys”, Mohsen K. Keshavarz, Dimitri Vasilevskiy, Remo A. Masut, Sylvain Turenne.
- Materials Science and Technology conference & exhibition (MS&T13), October 27-31, 2013, Montreal, Canada. Presented work: “Enhanced Mechanical Properties of Nanostructured (Bi_{0.2}Sb_{0.8})₂Te₃/MoS₂ Composite Thermoelectric Materials”, Mohsen K. Keshavarz, Melik Bouhadra, Dimitri Vasilevskiy, Remo A. Masut, Sylvain Turenne.